



저작자표시-비영리-변경금지 2.0 대한민국

이용자는 아래의 조건을 따르는 경우에 한하여 자유롭게

- 이 저작물을 복제, 배포, 전송, 전시, 공연 및 방송할 수 있습니다.

다음과 같은 조건을 따라야 합니다:



저작자표시. 귀하는 원저작자를 표시하여야 합니다.



비영리. 귀하는 이 저작물을 영리 목적으로 이용할 수 없습니다.



변경금지. 귀하는 이 저작물을 개작, 변형 또는 가공할 수 없습니다.

- 귀하는, 이 저작물의 재이용이나 배포의 경우, 이 저작물에 적용된 이용허락조건을 명확하게 나타내어야 합니다.
- 저작권자로부터 별도의 허가를 받으면 이러한 조건들은 적용되지 않습니다.

저작권법에 따른 이용자의 권리는 위의 내용에 의하여 영향을 받지 않습니다.

이것은 [이용허락규약\(Legal Code\)](#)을 이해하기 쉽게 요약한 것입니다.

[Disclaimer](#)

Doctoral Thesis

Multi-Color Iron MR Imaging: New development and clinical application

Hansol Lee

Department of Biomedical Engineering

Ulsan National Institute of Science and Technology

2021

Multi-Color Iron MR Imaging: New development and clinical application

Hansol Lee

Department of Biomedical Engineering

Ulsan National Institute of Science and Technology

Multi-Color Iron MR Imaging: New development and clinical application

A thesis submitted to
Ulsan National Institute of Science and Technology
in partial fulfillment of the
requirements for the degree of
Doctor of Philosophy

Hansol Lee

06.08.2021 of submission

Approved by



Advisor

HyungJoon Cho

Multi-Color Iron MR Imaging: New development and clinical application

Hansol Lee

This certifies that the thesis of Hansol Lee is approved.

06.08.2021 of submission

Signature



Advisor: HyungJoon Cho

Signature



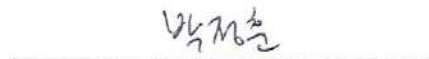
Joon-Mo Yang

Signature



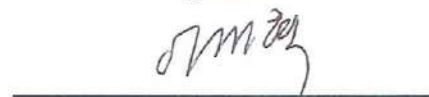
Woonggyu Jung

Signature



Jung-Hoon Park

Signature



Jae-Hyeok Lee

Abstract

In the brain, iron is an essential element in oxygen supply through blood vessels, energy metabolism, myelin formation, and neurotransmitter synthesis for brain development with maintaining homeostasis. However, even in healthy people, as they grow older, iron levels increase steadily in some regions of the brain. Among the inevitable iron deposits with aging, the unbound labile iron generates reactive oxygen and free radicals, which produce stress on the brain tissue and necrosis of cells, which are closely associated with neurodegenerative diseases. These finally promote neurodegenerative diseases, including Parkinson's disease and Alzheimer's disease, which accompany the damage in behavior and cognitive function. Therefore, developing magnetic resonance imaging-based biomarkers to detect various iron clusters deposited in the brain is crucial work for diagnosing and monitoring related diseases. However, it's still impossible to classify the states of iron and separate the various forms of iron deposited in the brain.

The aim of this study was to develop multi-color iron magnetic resonance imaging and the investigation of its *in vivo* feasibility through translation research from the preclinical trials including postmortem magnetic resonance imaging with histopathological validation to clinical application.

In the first section, it was discovered that the neuromelanin pigment within the human substantia nigra is only sensitive to T_2^* than other magnetic resonance contrast due to its paramagnetic property. Subsequently, the technique for specific visualization of neuromelanin-iron clusters in postmortem substantia nigra tissue was developed using combined T_2 and T_2^* (T_2^*/T_2 or T_2^*/T_2^2) with histopathological validation supported by the Monte Carlo simulation. Separate segmentations of the areas of iron detected in the T_2 map and neuromelanin observed in the T_2^*/T_2 map (or T_2^*/T_2^2 map) were available within the substantia nigra. The dorsal linear mismatch of T_2 and T_2^* was consistently detected in the brains of healthy controls. However, it was shortened in the diseased brains. *In vivo* feasibility and implication of developed technique as a clinical biomarker were quantitatively demonstrated in the patients of Parkinson's disease compared to healthy subjects.

In the second section, the iron deposition along the myelinated fiber of white matter was identified in the diseased brains. The iron-rich white matter at the frontal subcortical area contributes to the positive susceptibility in the patients of Adult-onset leukoencephalopathy with axonal spheroids and pigmented glia. Susceptibility-weighted imaging presented the noticeable phase signal showing the tree-like structure in the white matter of the frontal brain, with striking atrophy. This kind of rare tissue contrast in susceptibility-weighted imaging can aid to define Adult-onset leukoencephalopathy with axonal spheroids and pigmented glia. Besides, the deposited iron was verified on the myelinated fibers of the 3rd cranial nerve, which is the oculomotor nerve within the brain of progressive supranuclear palsy. Our

results demonstrated the enhanced magnetic resonance susceptibility value between the area of substantia nigra and red nucleus shown in the brain of progressive supranuclear palsy derives from exaggerated iron concentration on the myelinated fibers of the nerves between two structures.

In conclusion, the developed techniques of multi-color iron magnetic resonance imaging in this thesis can be useful imaging biomarkers to evaluate the progressive change of several iron-related neurodegenerative diseases, such as Perry syndrome, progressive supranuclear palsy, Parkinson's disease, and Adult-onset leukoencephalopathy with axonal spheroids and pigmented glia. The advanced research will be implemented to validate the alteration of magnetic resonance signal with the presence of iron molecules chelated to beta-amyloid or tau with Alzheimer's disease progression.

Contents

Abstract	1
Contents	3
List of figures	5
List of tables	8
Chapter 1. Introduction	
1.1 Motivation	9
1.2 Purpose	10
1.3 Outline	10
1.4 Abbreviations	11
Chapter 2. Background	
2.1 Iron-sensitive MRI technique	13-15
2.1.1 R_2 and R_2^* relaxation	13
2.1.2 Quantitative susceptibility mapping	14
2.2 Neurodegenerative disease	16-18
2.2.1 Parkinson's disease	16
2.2.2 Progressive supranuclear palsy	16
2.2.3 Perry syndrome	17
2.2.3 Adult-onset leukoencephalopathy with axonal spheroids and pigmented glia	17
Chapter 3. Detection of neuromelanin pigments in the substantia nigra	
3.1 Distinct detection of neuromelanin from iron deposition within the substantia nigra of post-mortem human brain using 7T MRI	19-37
3.1.1 Introduction	19
3.1.2 Methods	21
3.1.3 Results	24
3.1.4 Discussions and Conclusions	33
3.2 Determination of neuromelanin distribution in the dorsal area of substantia nigra pars compacta using T_2 and T_2^* mismatch	38-67
3.2.1 Introduction	38
3.2.2 Methods	39

3.2.3 Results	47
3.2.4 Discussions and Conclusions	62

Chapter 4. Iron deposition on the myelinated fibers

4.1 Pathological validation of paramagnetic lesions in the white matter of Adult-onset leukoencephalopathy with axonal spheroids and pigmented glia	68-74
4.1.1 Introduction	68
4.1.2 Methods	69
4.1.3 Results	71
4.1.4 Discussions and Conclusions	73
4.2 Accumulated iron on the myelinated fibers of the oculomotor nerve in the brain of progressive supranuclear palsy	75-87
4.2.1 Introduction	75
4.2.2 Methods	76
4.2.3 Results	80
4.2.4 Discussions and Conclusions	84

Chapter 5. Conclusions

5.1 Summary	88
5.2 Limitations and Future works	88

List of figures

Chapter 2. Background

2.1 Iron-sensitive MRI technique

Figure 2.1.1 The time progression of T_2^* decay and T_2 decay	13
--	----

Chapter 3. Detection of neuromelanin pigments in the substantia nigra

3.1 Distinct detection of neuromelanin from iron deposition within the substantia nigra of post-mortem human brain using 7T MRI

Figure 3.1.1 The MT- T_1 weighted images with co-registered LFB staining and Perls' Prussian blue staining	24
Figure 3.1.2 The influences of effective iron-cluster size on the quantitative T_2 , T_2^* , T_2^*/T_2 , and T_2^*/T_2^2 values derived from MC simulation	25
Figure 3.1.3 The schematic flow chart to segment neuromelanin and tissue iron distributions	26
Figure 3.1.4 The multiparametric MRI and co-registered histology to segment iron and neuromelanin distribution of the sample from the 75F subject	27
Figure 3.1.5 The multiparametric MRI and co-registered histology to segment iron and neuromelanin distribution of the sample from the left SN tissue of 70F subject	28
Figure 3.1.6 The multiparametric MRI and co-registered histology to segment iron and neuromelanin distribution of the sample from the 86F subject	29
Figure 3.1.7 The multiparametric MRI and co-registered histology for iron and neuromelanin distribution of the sample from the 60M subject	30
Figure 3.1.8 The partial correlation coefficients of T_2^* and T_2^*/T_2 (T_2^*/T_2^2) with respect to neuromelanin and iron distribution	33
Figure 3.1.9 The neuromelanin concentrations and iron-chelating ability per unit neuromelanin versus ages	34
Figure 3.1.10 The neuromelanin and myelin distribution from histology	35
3.2 Determination of neuromelanin distribution in the dorsal area of substantia nigra pars compacta using T_2 and T_2^* mismatch	
Figure 3.2.1 Monte Carlo simulation for transverse MR relaxation times based on the size of randomly distributed paramagnetic spherical particles	42
Figure 3.2.2 The manually drawn boundary (red dotted line) around the short T_2^* region with anterior-posterior length of the SN	46

Figure 3.2.3 3D reconstructed midbrain tissue showing deposited ferric iron and neuromelanin pigments48

Figure 3.2.4 Postmortem multimodal MRI of the three subjects49

Figure 3.2.5 Postmortem multimodal MRI with direct histological validation50

Figure 3.2.6 Neuromelanin segmentation by T_2^* and T_2 thresholding from the tissue sample obtained from a 75-year-old normal female51

Figure 3.2.7 Neuromelanin segmentation by T_2^* and T_2 thresholding from the tissue sample obtained from an 86-year-old normal female52

Figure 3.2.8 The overlap of the T_2^* and T_2 mismatch area of MRI and binarized neuromelanin distribution segmented from co-registered cryosectioned block-faces from normal controls53

Figure 3.2.9 Neuromelanin segmentation by T_2^* and T_2 thresholding from the tissue sample obtained from a 51-year-old male patient with SN depigmentation54

Figure 3.2.10 Iron chelation with neuromelanin pigments55

Figure 3.2.11 *In vivo* multimodal MRI for two intermediate levels in normal subjects57

Figure 3.2.12 *In vivo* multimodal MRI for two intermediate levels in Parkinson’s disease patients58

Figure 3.2.13 Schematic flow diagram for postmortem and *in vivo* MRI analysis59

Figure 3.2.14 *In vivo* T_2 and T_2^* ratios for two levels of normal subjects and Parkinson's disease patients60

Figure 3.2.15 *In vivo* MRI of normal controls and Parkinson’s disease patients62

Figure 3.2.16 *In vivo* MRI of three groups categorized from [^{18}F] FP-CIT PET63

Figure 3.2.17 The quantitative measurement of SN size in normal controls and Parkinson’s disease patients64

Chapter 4. Iron deposition on the myelinated fibers

4.1 Pathological validation of paramagnetic lesions in the white matter of Adult-onset leukoencephalopathy with axonal spheroids and pigmented glia

Figure 4.1.1 T_2 -weighted images and Susceptibility-weighted images on ALS cases70

Figure 4.1.2 Schematic flow diagram for postmortem and *in vivo* MRI analysis71

Figure 4.1.3 Postmortem MRI for ALS brain with histological validation72

4.2 Accumulated iron on the myelinated fibers of the oculomotor nerve in the brain of progressive supranuclear palsy

Figure 4.2.1 The delineation of ROI surrounding the region between SN and RN in SWI78

Figure 4.2.2 Histopathology and LA-ICP-MS with multimodal MRI on the postmortem SN of an 86-year-old normal female79

Figure 4.2.3 Histopathology and LA-ICP-MS with multimodal MRI on the postmortem SN of a 67-year-old male with PSP80

Figure 4.2.4 The representative MRI showing the SN and RN82

Figure 4.2.5 The line profile of normalized SWI intensity across the SN and RN83

Figure 4.2.6 The line profiles across SN and RN84

List of tables

Chapter 3. Detection of neuromelanin pigments in the substantia nigra

3.1 Distinct detection of neuromelanin from iron deposition within the substantia nigra of post-mortem human brain using 7T MRI

Table 3.1.1 PCC of multimodal MRI with respect to neuromelanin and iron distributed within SN32

3.2 Determination of neuromelanin distribution in the dorsal area of substantia nigra pars compacta using T_2 and T_2^* mismatch

Table 3.2.1 Quantitative values from T_2 and T_2^* mismatch and neuromelanin-sensitive MRI technique61

Chapter 4. Iron deposition on the myelinated fibers

4.1 Pathological validation of paramagnetic lesions in the white matter of Adult-onset leukoencephalopathy with axonal spheroids and pigmented glia

Table 4.1.1 Clinical and genetic findings of four patients with ALS69

4.2 Accumulated iron on the myelinated fibers of the oculomotor nerve in the brain of progressive supranuclear palsy

Table 4.2.1 Demographic and clinical characteristics of PD, PSP, and healthy control groups77

Table 4.2.2 Comparison of R_2^* and QSM in the region between SN and RN among PD, PSP, and control85

Chapter 1. Introduction

1.1 Motivation

In the brain, iron is an essential element in oxygen supply through the blood vessels, energy metabolism, myelin formation, and neurotransmitter synthesis for brain development with maintaining homeostasis. However, even in healthy people, as they grow older, iron levels increase steadily in some areas of the brain. Among the inevitable iron deposits with aging, the unbound labile iron generates reactive oxygen and free radicals, which produce stress on the brain tissue and the necrosis of cells. Many studies have shown that these finally lead to neurodegenerative diseases, such as Alzheimer's disease and Parkinson's disease, which accompany the damage in cognitive function and behavior. To prevent such neurodegeneration, most iron molecules are stably transported and stored in the brain by binding to proteins such as ferritin, transferrin, and hemosiderin.

Among the various iron distributions in the brain, most iron within the human substantia nigra (SN) located in the midbrain is in the form of a stable structure chelated to neuromelanin, which means sequestered or surrounded by neuromelanin. The degeneration of dopaminergic neurons containing neuromelanin pigments and excessive iron deposition in the SN is highly associated with Parkinson's disease progression. The molecules containing a high level of iron are also stored in the myelinated fiber of white matter and oligodendrocyte because iron is needed for the formation of myelin sheaths or axon maturation. But the problem of the mechanism of iron homeostasis causes abnormal iron deposition on the white matter. The vulnerability of oligodendrocytes and myelinated fibers against oxidative stress of iron can be stimulated by the environment of high iron concentration. The enhanced iron concentration on the white matter fibers causes damage to neurons according to the disease progression. Furthermore, iron molecules are deposited along the blood vessels. Iron in hemoglobin can be deposited along the vessels due to hemorrhage caused by damage to the blood-brain barrier. Perivascular Iron deposition also occurs due to the deposition of beta-amyloid on the vascular wall called cerebral amyloid angiopathy with Alzheimer's disease progression.

According to the situation, two different states of iron including ferric iron and ferrous iron are deposited in the brain. The iron chelated to neuromelanin in the SN is in the state of ferric iron. And the iron attached to the aggregated beta-amyloid is ferrous iron. Ferric iron is not reactive and stable. It can be detected by Perls' Prussian blue staining. Ferrous iron is toxic and causes oxidative stress to brain tissue. It is detected by Turnbull blue staining. Visualizing the progressive changes of iron distribution in the brain tissues is a crucial way for monitoring neurodegenerative diseases. However, it's still impossible to classify the iron states and separate the various iron forms deposited within the brain.

1.2 Purpose

The aim of this study is the development of multi-color iron magnetic resonance (MR) imaging and the investigation of its *in vivo* feasibility and implication. Using a new concept of MR imaging, the states of iron molecules were non-invasively classified and the various forms of iron deposition in the brain were separated. Analyzing the spatial distribution and concentration of iron molecules in the brain is also important. So, this study is called multi-color iron MR imaging.

The objectives in this thesis are:

- 1) the visualization of neuromelanin-iron complex in the SN,
- 2) the identification of iron deposition along myelinated fibers.

1.3 Outline

The followings are the summary of each Chapter.

Chapter 2 provides the background of multi-color iron MR imaging. The basic theory of iron-sensitive MRI techniques and the brief description of neurodegenerative diseases are proposed to explain the importance of the non-invasive classification of the iron states and the separation of the various iron forms.

Chapter 3 shows the specific visualization of neuromelanin-iron clusters in the postmortem SN with the validation by histopathological analysis and Monte-Carlo simulation. *In vivo* feasibility and implication of the developed method was investigated and compared between the patients of Parkinson's disease and healthy controls.

Chapter 4 describes the iron deposition on the myelinated fibers of white matter in the brain suffering from neurodegenerative diseases. The area of white matter within the brains of Adult-onset leukoencephalopathy with axonal spheroids and pigmented glia patients and progressive supranuclear palsy patients were analyzed by iron-sensitive MRI techniques with assessing pathological correlation and compared with the brains of healthy controls.

Chapter 5 contains the summary and conclusion of this thesis. The potential of the developed techniques to visualize iron clusters in the brain tissues as imaging biomarkers in the clinical diagnosis of neurodegenerative diseases is briefly described. The limitations of this study are presented with suggestions for improving the performance of iron imaging techniques for further study.

1.4 Abbreviations

AC-PC	Anterior commissure and posterior commissure
ALSP	Adult-onset leukoencephalopathy with axonal spheroids and pigmented glia
COSMOS	Calculation of susceptibility through multiple orientation sampling
[¹⁸F] FP-CIT	¹⁸ F-N-(3-fluoropropyl)-2β-carbomethoxy-3β-(4-iodophenyl) nortropane
FA	Flip angle
H-Y	Hoehn and Yahr
LA-ICP-MS	Laser ablation inductively coupled plasma mass spectrometry
LBV	Laplacian boundary value
LFB	Luxol fast blue
MC	Monte Carlo
MEDI	Morphology enabled dipole inversion
MGE	Multiple gradient echo
MR	Magnetic resonance
MRI	Magnetic resonance imaging
MS	Multiple sclerosis
MSME	Multi-spin multi-echo
MT	Magnetization transfer
PD	Parkinson's disease
PET	Positron emission tomography
PS	Perry syndrome
PSP	Progressive supranuclear palsy
QSM	Quantitative susceptibility mapping
RARE	Rapid acquisition with relaxation enhancement
RAREVTR	Rapid acquisition with relaxation enhancement with variable repetition time
RN	Red nucleus
ROI	Region of interest
SD	Standard deviation
SN	Substantia nigra
SNc	Substantia nigra pars compacta
SNr	Substantia nigra pars reticulata
SWI	Susceptibility-weighted imaging
TE	Echo time

TR Repetition time

UPDRS III Unified Parkinson's disease rating scale part III

WM White matter

Chapter 2 Background

2.1 Iron-sensitive MRI technique

2.1.1 R_2 and R_2^* relaxation

The simplest magnetic resonance (MR) image is acquired by measuring the global signal in the transverse plane from the sample. After the tipping net longitudinal signal to the transverse plane by application of radiofrequency (rf) pulse, the vector sum of transverse spin components is in the coherence. Several causes bring the loss of transverse coherence. R_2 ($1/T_2$) and R_2^* ($1/T_2^*$) relaxation are the process that the signals in the transverse plane decay or dephase. R_2 is called spin-spin relaxation because one excited spin transfers the energy to other spins. Due to the spin-spin relaxation, the movement of spins from molecular vibrations or rotations induces spin precession. Besides, the proton never experiences a 100% homogeneous magnetic field. As time goes by, the spins encounter the fluctuating local magnetic field and precess on the transverse plane at the Larmor frequency with loss of phase coherence. This precession generates the free induction decay (FID) with the vector sum toward 0.

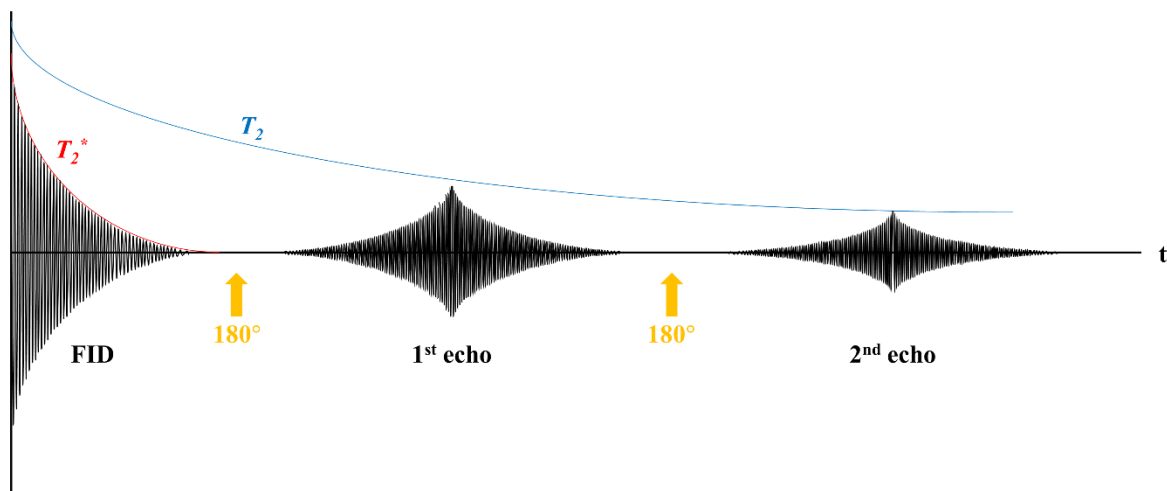


Figure 2.1.1 The time progression of T_2^* decay and T_2 decay.

The relaxation times T_2 and T_2^* are decided by the time demanded for the signal in the transverse plane exponentially decaying or dephasing to 37 % of the initial signal after the rf pulse. The relation between T_2 and T_2^* is

$$\frac{1}{T_2^*} = \frac{1}{T_2} + \frac{1}{T_2 i} \quad (1)$$

, where $T_2 i$ is a major factor in determining T_2^* associated with the main magnetic field inhomogeneity and local magnetic susceptibility difference. $T_2 i$ is usually from the significant iron deposition or calcification in the tissue and the area near the air tissue interface. The Gradient-echo sequence produces the FID signal following 90° rf pulse. The bipolar readout gradient (frequency encoding gradient) generates an echo for the data related to the time constant of T_2^* .

The application of 180° rf pulse in spin-echo sequence causes the reversal of proton dephasing with the same rate of precession prior to the 180° rf pulse. The proton dephasing related to $T_2 i$ is eliminated because all protons encounter the same environment before and after the pulse. The irreversible relaxation caused by the interaction between spins is still left regardless of the application of 180° rf pulse. The reformation of coherence in the spin-echo sequence makes an echo. The resultant signal is associated with T_2 relaxation. Using multiple bipolar readout gradients and 180° rf pulses continuously generate the other signals until the protons are completely dephased by T_2^* and T_2 relaxation.

2.1.2 Quantitative susceptibility mapping

Magnetic susceptibility is a dimensionless and inherent property of the source. The susceptibility of a material can be positive (paramagnetic) or negative (diamagnetic). Iron is the most abundant element with paramagnetic property in the human brain. The myelin sheath of white matter is a diamagnetic source, which is composed of lipids and proteins. Calcification is another diamagnetic source in the diseased brain.

The induced magnetic field is determined by the susceptibility of the material in accordance with the applied magnetic field. The sources with paramagnetic susceptibility induce internal magnetic fields in the same direction as the applied magnetic field. However, the diamagnetic susceptibility sources generate magnetic fields in the opposite direction. The relation between the spatially different susceptibility and the magnetic field is expressed as

$$\Delta B(r) = B_0 \cdot d(r) * \chi(r) \quad (2)$$

, where B_0 is the main magnetic field and $d(r)$ is the unit dipole kernel in the spherical polar coordinates. Therefore, the reconstruction of the susceptibility value from the magnetic field map needs inverse calculation. The convolution in the spatial domain corresponds directly to a multiplication in the frequency domain. The equation is expressed as

$$\mathcal{F}\{\Delta B(k)\} = B_0 \cdot D(k) \cdot \mathcal{F}\{\chi(k)\} \quad (3)$$

, where \mathcal{F} is the Fourier transform operator and $D(k)$ is the unit dipole kernel in the Fourier domain.

Quantitative susceptibility mapping (QSM) is a novel technique solving an inverse calculation to reconstruct the 3D distribution of magnetic susceptibility value of the tissue using an MR phase image obtained from gradient-echo-based sequences. In QSM, the standard scale of the measured value is a voxel. Due to each voxel containing various susceptibility sources according to the environment, the bulk susceptibility in each voxel was estimated by the weighted sum of the magnetic susceptibility of the respective element with its fractional volume as the following equation,

$$\chi_{\text{voxel}} = \sum_k V_k \cdot \chi_k \quad (4)$$

, where V_k is the volume fraction and χ_k is the susceptibility of component k .

QSM can be applied in the investigation of susceptibility differences in human tissues, especially in the case of iron deposition and calcification with aging and the progression of neurodegenerative diseases. Even though T_2^* or R_2^* map is the quantitative analysis using the multiple magnitude images of gradient-echo based sequences, the calcification and iron deposition in the tissue cannot be distinguishable based on the T_2^* or R_2^* values, because both circumstances bring the shortened T_2^* (increased R_2^*) values due to the local magnetic susceptibility difference. On the other hand, QSM can provide the differentiation of such cases as the positive value for iron deposition and the negative value for calcification.

2.2 Neurodegenerative disease

2.2.1 Parkinson's disease

Parkinson's disease (PD) is a common progressive neurodegenerative disorder mainly affecting the motor function of the patient. The clinical motor symptoms of PD include postural disturbance, rigidity, tremor, and bradykinesia. Depression, sleep disorders, constipation, genitourinary dysfunction are the non-clinical symptoms of PD. Loss of dopaminergic neurons within the substantia nigra (SN) of the midbrain is pathological characteristics of PD. The decline of dopamine levels over time induced by the death of dopaminergic neurons causes most abnormal motor dysfunctions in PD. Besides, excessive iron accumulation associated with oxidative stress in the SN is another abnormal characteristic of PD. There is no standard clinical assessment to diagnose PD. The diagnosis of PD is primarily following clinical criteria, based on the patient's symptom and medical history. Currently, medical imaging tools of MRI, positron emission tomography (PET), single-photon emission tomography (SPECT), and ultrasound can be promising diagnostic methods for helping monitor and diagnose PD. They have been used to distinguish PD from other diseases. For MRI, the visualization of progressive changes of neuromelanin pigment located in the SN is believed as a promising method to monitor and diagnose PD patients considering nigral degeneration with disease progression. It is well known that using the magnetization transfer (MT) contrast pulses on T_1 -weighted scans shows a bright area adequately sensitive to the neuromelanin distribution, which is called as neuromelanin-sensitive MRI technique. Furthermore, nigrosomes are clusters of neuromelanin-containing dopaminergic cells within the SN degenerated preferentially with the progression of PD by the increased iron content. The nigrosome-1, which is the largest cluster, is detected in susceptibility-weighted images (SWI) as a dorsolateral high signal intensity with an ovoid appearance in healthy subjects. R_2^* and QSM have been utilized for measuring the iron levels within the SN and have demonstrated an increase of iron deposition in the SN of PD patients.

2.2.2 Progressive supranuclear palsy

Progressive supranuclear palsy (PSP) is one of the degenerative parkinsonism, which is defined by the pathology of hyper-phosphorylated tau protein and the loss of nerve cells in cortical and subcortical regions, including the subthalamic nucleus, globus pallidus, and especially in the SN. Palsy of the gaze in vertical plane has been observed as other principal features of PSP. Atrophy of the midbrain is the common MRI findings in the PSP brain. The hyperintensity in T_2 -weighted image was identified in the

pons, which is the indicator of gliosis. Distinctive pattern of iron deposition in the brain of PSP patients can serve the potential diagnostic marker for *in vivo* MRI studies. The abnormal iron concentration in the specific area of brain would help differentiate the patients of PSP from healthy controls. According to the degeneration of neural cells in the SN, subthalamic nucleus, globus pallidus, and red nucleus (RN), significant increases in iron-related MR signals have been found in the corresponding areas. In postmortem MRI studies using histopathological examinations, the destruction of internal architecture and microstructural surrounding the SN is significantly more than PD. Consequently, the area of hypointense signals around the border of SN that interconnect the area of hypointense signals of RN in the FLASH MRI leads to the difficult demarcation between two structures in the midbrain of PSP patients.

2.2.3 Perry syndrome

Perry syndrome (PS) is a rare progressive brain disease characterized by movement abnormality as Parkinsonism, severe loss of weight, central hypoventilation, and psychiatric changes. The movement abnormality with disease progression accompanies the changes of behavior and personality of the patients. PS is a hereditary disorder with an autosomal dominant manner. The pathological hallmarks of PS are the severe depigmentation and the gliosis in the SN with the mutation on the axon of the Dynactin subunit 1 (*DCTN1*) gene, which provides the instructions for producing dynactin-1 protein involved in transporting materials within the cells. Mutation of the *DCTN1* gene disrupts the transportation of materials within cells causing malfunction in neurons. The neurons related to breathing, emotion, and movement gradually dies and they underlie the pathogenesis of PS. The marked loss of dopamine transporters is shown in the results of [¹⁸F] FP-CIT PET application on PS patients demonstrating the severe degeneration of dopaminergic neurons. Although there are subtle changes in the brain MRI of PS like frontotemporal atrophy, remarkable change was still not detected consistently. It can be also due to the very rare individuals reported worldwide.

2.2.4 Adult-onset leukoencephalopathy with axonal spheroids and pigmented glia

Adult-onset leukoencephalopathy with axonal spheroids and pigmented glia (ALSP) is a progressive neurodegenerative disease described by cognitive disorder, behavior and psychiatric symptoms, Parkinsonism, executive dysfunction, ataxia, and apraxia. ALSP is an autosomal dominant disease with pathologic features of the presence of myelin loss sparing the subcortical U-fibers, pigmented microglia, axonal spheroids, and reactive astrocytosis caused by mutations of the colony-stimulating factor 1

receptor (*CSF1R*) gene and the alanyl-transfer (t)RNA synthetase 2(*AARS2*) gene in the white matter. *CSF1R* gene encodes transmembrane tyrosine kinase receptor in the phagocytic cells, microglia. The mutation in the *CSF1R* gene is known as the causative factor for the pathogenesis in the white matter. *AARS2* gene is expressed for a mitochondrial enzyme. The mutation of the *AARS2* gene induces leukoencephalopathy. MRI has non-invasively demonstrated the marked atrophy of the cerebral cortical area corresponding to the WM lesions as well as enlarged ventricles. Thinning of corpus callosum thickness, white matter lesions with calcification, the abnormal signal in the pyramidal tracts are other MRI findings of the ALSP brain.

Chapter 3. Detection of neuromelanin pigments in the substantia nigra

3.1 Distinct detection of neuromelanin from iron deposition within the substantia nigra of post-mortem human brain using 7T MRI

3.1.1 Introduction

Neuromelanin is mostly found in the SN pars compacta (SN_c) and is known to be a powerful iron chelator [1, 2, 3]. The majority of ferric iron, which can bring oxidative stress to the brain tissue by generating highly reactive free oxygen radicals, can be stored in the ferritin of the human brain [4, 5]. In the SN_c, most of iron molecules are chelated by the neuromelanin in the dopaminergic neurons to form a stable complex; thus, dopaminergic neurons are protected from iron toxicity [6, 7]. There are two different iron chelating sites on Neuromelanin with high and low affinities [1, 8]. The protective ability of neuromelanin against the oxidative stress of iron by chelating iron occurs when the iron is mostly chelated in high affinity site [1]. Parkinson's disease (PD) is a major progressive neurodegenerative disease associated with the loss of neuromelanin -containing dopaminergic neurons of the substantia nigra (SN) [9]. With the progression of PD, it is generally recognized that iron depositions increase at the SN of the PD brain, while the neuromelanin -containing dopaminergic neurons decreases [1]. When the iron chelating site of high affinity are saturated in the pathogenesis of PD, the iron only can be chelated to the site of low affinity and the hydroxyl radicals were formed to generate oxidative stress [10]. Historically, the quantitative measurements of iron and ultrastructural images of neuromelanin granules in dopamine neurons of human SN have been investigated using X-ray diffraction analysis, nuclear magnetic resonance spectroscopy, infrared spectroscopy, Electron paramagnetic resonance spectroscopy, Analytical Electron Microscopy, and Nano-Secondary Ion Mass Spectrometry [11, 12, 13]. It is increasingly important to non-invasively distinguish the spatial distribution of neuromelanin from that of iron in the SN for detecting and monitoring PD pathology. As neuromelanin -iron complex and ferric iron are endogenous paramagnetic sources [2, 3], magnetic resonance imaging (MRI) approaches appear to be a promising modality for the non-invasive delineation of both key components in SN.

The hyperintense neuromelanin -related MRI contrast with magnetization transfer (MT)- T_1 weighted scans were investigated to delineate neuromelanin distribution [14]. The neuromelanin -related MRI contrast is believed to be generated both from the contribution of neuromelanin to paramagnetic T_1

shortening and MT effect [14, 15, 16]. Specifically, the hyperintense region near the SN is observed with MT- T_1 weighted imaging, such as 2D multi slice fast spin echo acquisition. Several studies have also reported the shrinkage of the hyperintense region of MT- T_1 weighted images near the SN with the progression of the PD [14, 17, 18, 19]. However, the association of such MRI hyperintensity in the SN with neuromelanin distribution is confounding. Considering the ambiguity in an overlap between the deposits of paramagnetic neuromelanin-iron complex and ferric iron in normal and PD SN, it is difficult to assign the hyperintense region for the exclusive detection of neuromelanin from only T_1 weighted MR images. Additionally, the interdependence between MT saturation and myelination in SN further complicates the interpretation of the hyperintensity from conventional MT- T_1 weighted images [20].

On the other hand, neuromelanin-iron complex and ferric iron act as significant endogenous paramagnetic perturbs to generate magnetic susceptibility mismatch with respect to underlying tissue in normal and PD SN [2]. Resulting inhomogeneous magnetic field variations affect the associated transverse MR relaxations, such as T_2 and T_2^* . As both T_2 and T_2^* values will change with the varying concentrations of paramagnetic sources, it is still impossible to spatially separate neuromelanin-iron complex and ferric iron. However, the T_2 and T_2^* values of MR voxels do not only depend on the fractional volumes (concentrations) but also on the effective size of paramagnetic perturbers [21]. For example, with increasing fractional volume of a paramagnetic source, both T_2 and T_2^* values will correspondingly shorten. On the other hand, the T_2 and T_2^* values tend to lengthen and saturate, respectively, with the increasing size of the paramagnetic perturbers at a fixed fractional volume [21]. Considering the significantly larger effective size of neuromelanin-iron complex compared to ferric iron, it is worthwhile to take advantage of this diverging T_2 and T_2^* behaviors with the increase in the size of paramagnetic perturbers. It may provide a unique non-invasive opportunity in distinguishing neuromelanin-iron complex from ferric iron in human SN, irrespective of their concentrations.

In this study, we investigated the direct correlations of multiple MR parameters [T_1 , T_2 , T_2^* , T_2^*/T_2 , T_2^*/T_2^2 , susceptibility weighted imaging (SWI), and quantitative susceptibility mapping (QSM)] at 7T with respect to quantified histological components, such as myelin (Luxol Fast Blue (LFB)), ferric iron (Perls' Prussian blue staining), and neuromelanin pigments, from six post-mortem human SN samples from five subjects (age: 40-year-old male (40M), 60-year-old male (60M), right and left SNs from 70-year-old female (70F_L, 70F_R), 75-year-old female (75F), and 86-year-old female (86F)). Numerical T_2 and T_2^* relaxation simulations in the presence of paramagnetic spheres with varying sizes were performed to derive the feasibility of MR relaxometry in distinguishing neuromelanin-iron complex from ferric iron by emphasizing the size differences between them. The efficacy of the suggested MR relaxometry method, merging T_1 , T_2 , and T_2^* contributions, in spatially separating neuromelanin-iron complex from ferric iron was directly verified using the co-registered histological components in SN

for the six post-mortem samples from five subjects.

3.1.2 Methods

Numerical simulations for MR relaxation

To demonstrate the usefulness of T_2 and T_2^* values to separate neuromelanin distribution, Monte Carlo (MC) simulations on spin diffusion were implemented by examining the dependence of the size of paramagnetic perturbers on T_2 and T_2^* values. In the simulation, the variables for setting were suggested from MRI experiments. The perturbers with spherical shape were randomly scattered with the start of each repetition. The matrix size was set as $0.136 \times 0.136 \times 0.136 \text{ mm}^3$. The perturbers have the radii as 3, 5, 7, 9, 11, 13, and 15 μm . Their partial volumes with respect to the whole space was 2%, 4%, and 6%. The perturbers has $1 \times 10^{-7} [\text{cgs}]$ for the magnetic susceptibility value. To calculate T_2 and T_2^* values, echo times were decided as 3, 7, 11, 15, 19, 23, and 27 ms for gradient echo and 8, 16, 24, 32, 40, 48, and 56 ms for spin echo.

Each perturbers causes the variation of local magnetic field on the surrounding area. The convolution between the calculated local magnetic field variation and the distribution of perturbers presents the total change of magnetic field. 60,000 protons moved incoherently in the whole simulation space. Until the echo time, protons diffuse continuously with 0.1 ms time steps. At each echo time, the signal reductions of gradient and spin echo acquisitions in the entire space were obtained from the voxel-wisely accumulated phase. 10 times repetition was performed for averaging the signals. T_2 and T_2^* values were linearly fitted from the signals of respective echo time.

Postmortem brain samples

The six samples of post-mortem midbrains tissue including SN were obtained from five subjects (40-year-old male (40M), 60-year-old male (60M), 70-year-old female left tissue (70F_L), 70-year-old female right tissue (70F_R), 75-year-old female (75F), and 86-year-old female (86F)), which have no history of other kinds of neurological diseases. All included subjects signed the informed consent and they joined the Anatomical Donation Program of Pusan National University. All methods in this study were approved by Institutional Review Board of both Pusan National University Yangsan Hospital (PNUYH) and Ulsan National Institute of Science and Technology (UNIST) according to the Helsinki Declaration guidelines. The previous work reported the association between T_2^* values and the results of Perls' blue staining in two samples of 40M and 70F_R [22]. After the extractions, the post-mortem brains were immediately fixed in the 10% neutral buffered formalin. Subsequently, they were sectioned along the midsagittal plane to generate right and left SN [23]. They were cut into the block with 1.5-cm-thickness

including the whole SN levels parallel to a plane bisecting the superior colliculus and the mammillary body.

Ex vivo MRI experiments

Post-mortem brain tissues underwent the *ex vivo* MRI experiments using 7T preclinical MRI scanner (Bruker, Germany). Samples were positioned delicately in the 50 ml syringe with formalin solution. T_1 weighted MR technique with MT saturation was performed using RARE sequence with multi slice acquisition with and without MT preparation contrast pulses using TR = 800 ms and TE = 8 ms. The MT contrast were two sinc pulses of flip angle = 600° for 10 ms duration with 1 kHz off-resonance [15, 17]. RAREVTR sequence was performed to acquire T_1 map using TR = 107, 200, 300, 500, 700, 1000, 2000, 3000, and 5000 ms, and TE = 7.1 ms. MSME sequence was performed to acquire T_2 map using TR = 5000 ms, and TE = 8, 16, 24, ..., and 120 ms. MGE sequence was performed to acquire T_2^* map using TR = 2000 ms, and TE = 3.3, 7.4, ..., and 40.2 ms. The overall parameters for each scan were isotropic in-plane resolution of $136 \times 136 \mu\text{m}$, matrix size of 256×256 , and 20 slices with slice thickness of 500 μm .

Histological analysis

After MR scan, the midbrain samples were cryoprotected using the sucrose solution with concentration of 10%, 20%, and 30%. Subsequently, the cryoprotected tissues were frozen by liquid nitrogen and isopentane. Comparing with T_1 weighted MR images, 50 μm -thick tissue blocks were obtained using the cryostat by considering the position and angle of each tissue. The thin slides representing each MR image were stained by LFB staining and Perls' blue staining. Myelinated fiber in the white matter was demonstrated using LFB staining. The distribution of ferric iron was stained by Perls' blue staining. However, neuromelanin-chelated ferric iron was not identified in the Perls' blue staining. The stained slides were scanned using Virtual Microscope (Olympus, Japan).

The region of neuromelanin was shown as brown or black color in the Perls' blue staining. The binary image for neuromelanin pigments in each slide was acquired by thresholding the sum of all values of RGB channels. For the binary image of iron, blue dots in the Perls' blue staining were extracted by highlighting blue channel among RGB channels (value of blue channel – value of red channel/2 – value of green channel/2). In the case of the binary image of myelin, the value of blue channel was used in LFB staining. The down-sampled images were generated from the binary image of neuromelanin, iron, and myelin counts using 10×10 pixel block, which suggest the density of each component identified in each staining [22].

Post-processing

Quantitative T_1 , T_2 , and T_2^* values for each voxel were estimated by logarithmic linear regression of the relaxation signal from the respective pulse sequence. SWI was generated from both magnitude and phase images of the same gradient echo sequence [25]. The phase image was acquired after unwrapping and filtering using a low pass filter to remove the noise; then, the phase image was multiplied to the corresponding magnitude image [25]. The bulk magnetic susceptibility images from the QSM algorithms were produced through temporal and spatial phase unwrapping [26], background field removal using Laplacian boundary value method [27], and deconvolution of dipole kernel by morphology enabled dipole inversion (MEDI) technique [28].

Based on the MC simulation results, the quantitative T_2^*/T_2 maps were acquired voxel by voxel to segment the region of neuromelanin-iron complex from that of ferric iron and other diamagnetic tissues components. The diamagnetic tissue region from the same subject was selected as a reference region of interest (ROI), and then mean and standard deviation (STD) for the reference ROI were calculated. The threshold value for segmenting the region of neuromelanin-iron complex was set as $\text{mean}_{\text{REF}} - 5 \times \text{STD}_{\text{REF}}$ of reference ROI. The whole SN mask was selected from the T_1 weighted image. Conclusively, the region of neuromelanin-iron complex was represented by multiplying the thresholded neuromelanin-iron complex region from T_2^*/T_2 map and the whole SN mask from T_1 weighted image. The ferric iron rich region was also selected using the thresholding from the T_2 map.

To match MRI and corresponding histological slides, each MR image was upsampled by a cubic B-spline interpolation. The upsampled T_1 weighted images were co-registered to corresponding LFB staining images to have the same resolution using 2D rigid transformation. Other MR images were co-registered using the same 2D transformation matrix information. Perls' Prussian blue staining images were aligned to right neighboring LFB staining images.

Voxel-by-voxel correlation between various MR images and pigment distributions from Perls' Prussian blue staining was investigated. Corresponding data from five slices for each subject were analyzed. The Pearson partial correlation coefficient was calculated among MR parameter, iron deposits, and neuromelanin pigments while controlling the effect of one other variable. For the multiple linear regression model, the partial regression coefficients, $\beta_{\text{neuromelanin}}$ and β_{iron} , for neuromelanin pigments and iron deposits were determined from the equation $Y = \beta_0 + \beta_{\text{neuromelanin}}x_{\text{neuromelanin}} + \beta_{\text{iron}}x_{\text{iron}}$, where β_0 is the intercept of Y, and $x_{\text{neuromelanin}}$ and x_{iron} are two independent variables (the extracted density of neuromelanin pigments and iron deposits, respectively). $\beta_{\text{neuromelanin}}$ and β_{iron} are slopes for each independent variable, $x_{\text{neuromelanin}}$, and x_{iron} , respectively, to measure how strongly each variable influences Y, the dependent variable (T_2^* for our work). $\beta_{\text{neuromelanin}}$ was suggested as the T_2^* reduction per unit neuromelanin, possibly indicating the amount of iron load on neuromelanin.

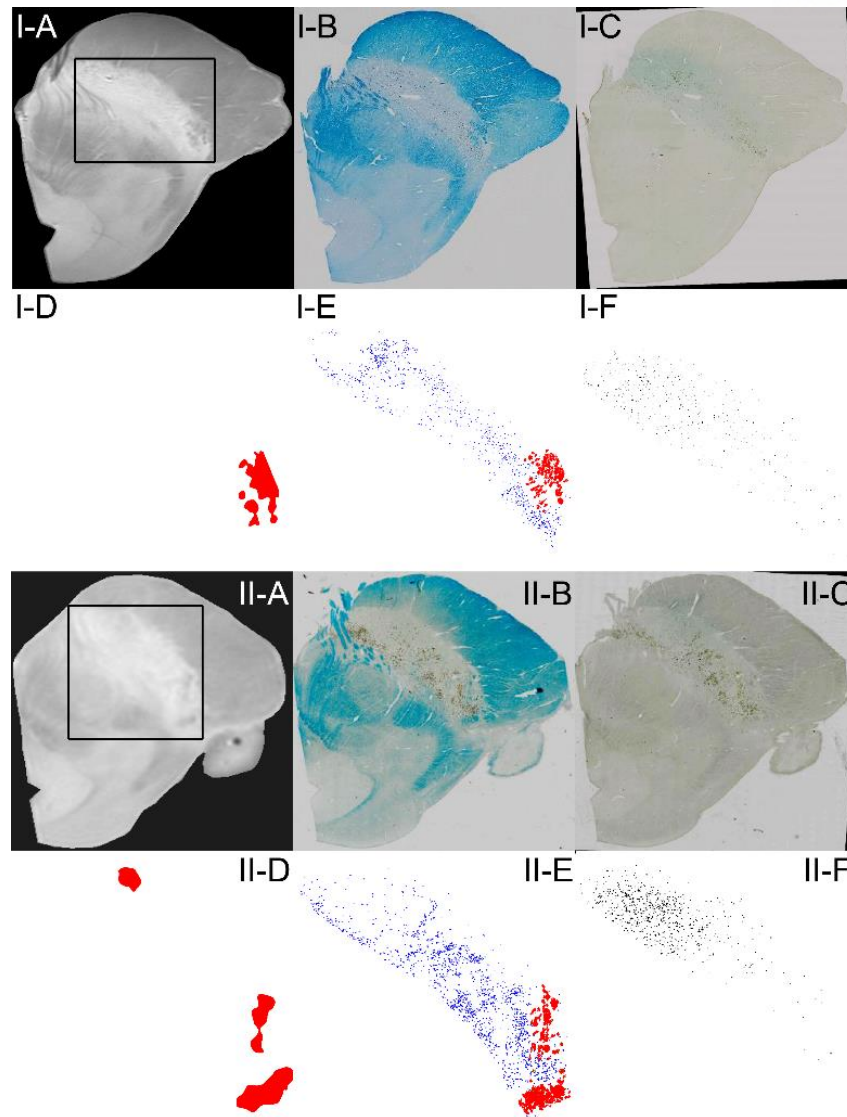


Figure 3.1.1 The $MT-T_1$ weighted images with co-registered LFB staining and Perls' Prussian blue staining. (I: 40M, II: 70FL) (A): $MT-T_1$ weighted image, (B): LFB staining, (C): Perls' Prussian blue staining, (D): magnified hypointense area from $MT-T_1$ weighted image within the SN shown as a red mask, (E): neuromelanin distribution (blue dots) from Perls' Prussian blue staining and myelin distribution (red dots) from LFB staining with same magnification factor used to generate (D), (F): iron deposited distribution (black dots) from Perls' Prussian blue staining with same magnification factor used to generate (D).

3.1.3 Results

T_1 weighted image with MT effects and histological components in SN

The correlation of T_1 weighted images with MT effects to neuromelanin pigments was investigated

with the co-registered LFB staining and Perls' Prussian blue staining as shown in Figure 3.1.1 from two subjects, 40M and 70F. The hypointense areas within the SN were segmented from the T_1 weighted images with MT effects as the red regions, magnified in Figure 3.1.1I-D and Figure 3.1.1II-D. The blue-stained myelin from LFB staining (Figure 3.1.1I-B and Figure 3.1.1II-B) was shown as red dots in Figure 3.1.1I-E and Figure 3.1.1II-E with the same magnification factor as that used in Figure 3.1.1I-D and Figure 3.1.1II-D. The neuromelanin pigments were identified as blue dots in Figure 3.1.1I-E and Figure 3.1.1II-E, which can be both seen from LFB and Perls' Prussian blue staining (Figure 3.1.1I-C and Figure 3.1.1II-C). The iron deposits from the co-registered Perls' Prussian blue staining were identified as black dots as shown in Figure 3.1.1I-F and Figure 3.1.1II-F. When Figure 3.1.1-D and Figure 3.1.1-E with same magnification and co-registration were compared, the red areas were significantly co-localized. In other words, the hypointense areas in the T_1 weighted images with MT effects were related to the myelin distribution in LFB staining.

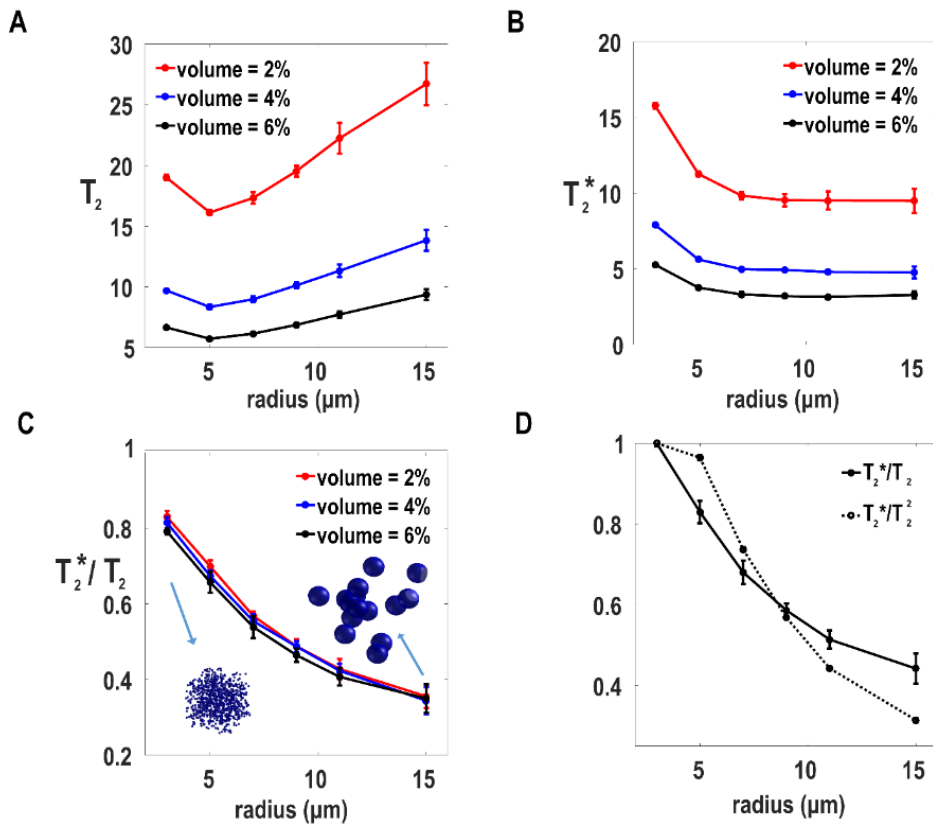


Figure 3.1.2 The influences of effective iron-cluster size on the quantitative T_2 , T_2^* , T_2^*/T_2 , and T_2^*/T_2^2 values derived from MC simulation. (A): T_2 relaxation time for different sizes and partial volumes (B): T_2^* relaxation time for different sizes and partial volumes. (C): T_2^*/T_2 values for different sizes and partial volumes. (D): Comparison between T_2^*/T_2 and T_2^*/T_2^2 for different sizes at a 6% partial volume. The red, blue, and dark lines correspond to partial volumes of 2%, 4%, and 6%, respectively.

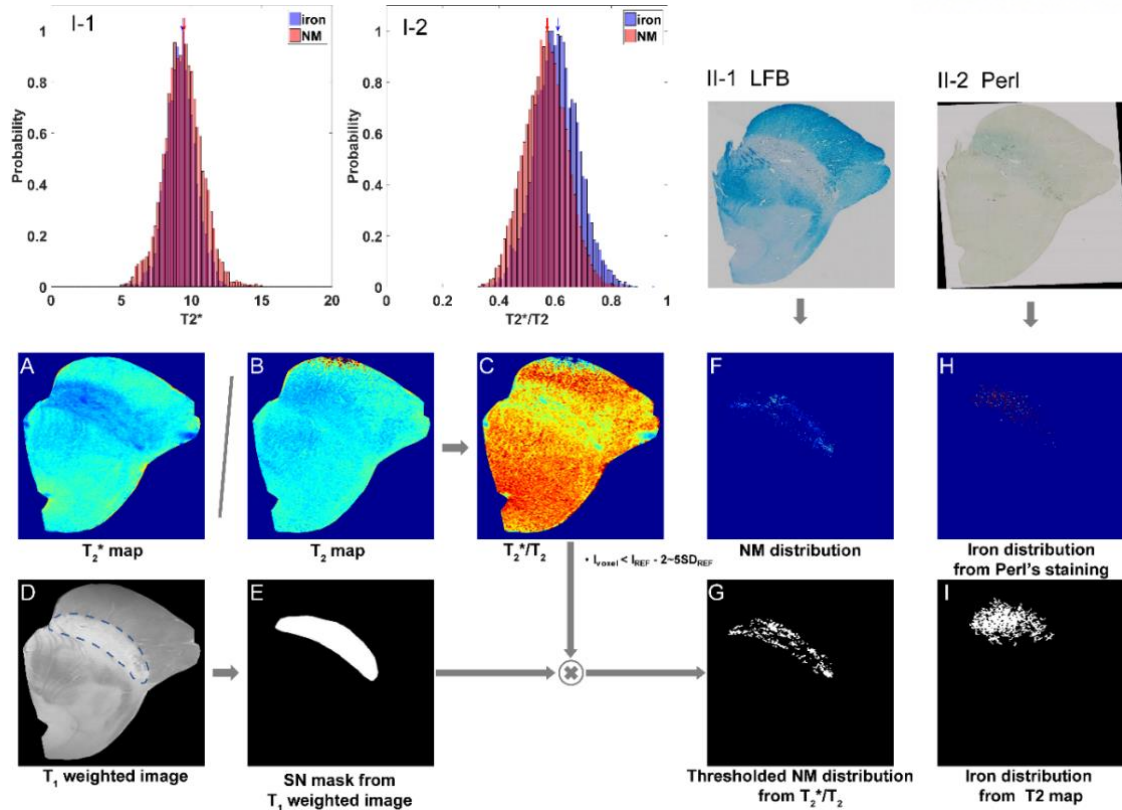


Figure 3.1.3 The schematic flow chart to segment neuromelanin and tissue iron distributions. Histograms for the T_2^* values (I-1) and T_2^*/T_2 values (I-2) for the iron (red) and neuromelanin (blue) distributions detected from Perls' Prussian blue staining for the sample from the 40M subject. The median values were marked with corresponding arrows. The schematic flow chart guided the procedure to segment iron-clustered neuromelanin and tissue iron distributions from MR relaxometries. (A): T_2^* map, (B): T_2 map, (C): T_2^*/T_2 map, (D): T_1 weighted image, (E): SN mask from T_1 weighted image, (F): neuromelanin distribution from Perls' Prussian blue staining, (G): Thresholded neuromelanin distribution from T_2^*/T_2 map, (H): Iron distribution from Perls' Prussian blue staining, (I): Thresholded iron distribution from T_2 map

Transverse MR relaxometries depending on the size of spherical perturbers

The size-dependent T_2 and T_2^* values from MC simulations are shown in Figure 3.1.2A and Figure 3.1.2B at varying fractional volumes of the perturbers of 2%, 4%, and 6%. The T_2 and T_2^* values were shortened with the increasing volume fraction of spherical perturbers shown as different color lines in Figure 3.1.2A and Figure 3.1.2B. When the radius was small, the T_2 and T_2^* values tended to decrease when the sphere size increased. As the sphere size further increased, T_2 values started to rise, while the T_2^* values saturated. Both size and volume fraction of the spherical perturbers influenced T_2 and T_2^* values. However, it was observed that the influence of volume fraction of spherical perturbers was

minimized for T_2^*/T_2 as shown in Figure 3.1.2C. The T_2^*/T_2 values were mainly correlated with the size of spherical perturbers. It was also observed that the T_2^*/T_2^2 values dropped more sharply with the increase in the size of spherical perturbers than the corresponding T_2^*/T_2 values at fixed volume fraction (6%) shown in Figure 3.1.2D.

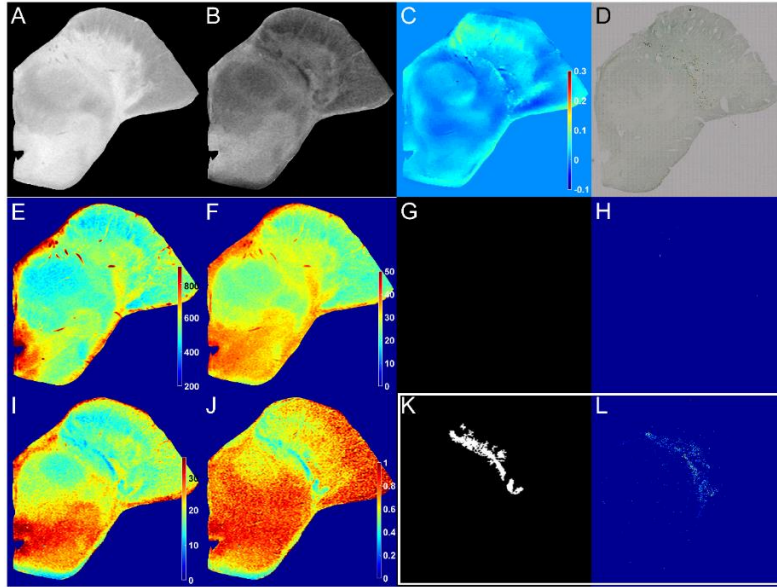


Figure 3.1.4 The multiparametric MRI and co-registered histology to segment iron and neuromelanin distribution of the sample from the 75F subject. (A) : MT T_1 -weighted image, (B) : SWI, (C) : QSM, (D) : Perls' Prussian blue staining, (E) : T_1 map, (F) : T_2 map, (G) : Iron distribution from T_2 map, (H) : Iron distribution from Perls' Prussian blue staining, (I) : T_2^* map, (J) : T_2^*/T_2 map, (K) : neuromelanin distribution from T_2^* map, (L) : neuromelanin distribution from Perls' Prussian blue staining.

The segmentation of neuromelanin-iron complex and ferric iron in the SN

The experimental T_2^* map in Figure 3.1.3A indicated the presence of iron deposits and neuromelanin pigments identified from Perls' Prussian blue staining, along with the corresponding T_2^*/T_2 map in Figure 3.1.3C. The clear relative shift of T_2^*/T_2 distribution of the region of neuromelanin-iron complex with respect to that of the region of ferric iron was observed in Figure 3.1.3I-2. These were compared with the corresponding T_2^* distributions shown in Figure 3.1.3I-1. The red and blue arrows on top of the histograms denote the median values of corresponding distributions. Accordingly, the process of specifically segmenting the region neuromelanin-iron complex in SN was illustrated in Figure 3.1.3A-3I for the 40M. The T_2^* map, which shows spatially overlapping distributions of neuromelanin with iron in SN in Figure 3.1.3A, was divided by the T_2 map in Figure 3.1.3B to obtain the T_2^*/T_2 map shown in Figure 3.1.3C. The whole SN mask in Figure 3.1.3E was obtained from the corresponding T_1 weighted

image as shown in Figure 3.1.3D. Then, the resulting T_2^*/T_2 map was combined with SN mask, and thresholded ($T_2^*/T_2 < \text{mean}_{\text{REF}} - 5 \times \text{STD}_{\text{REF}}$, tissue reference ROI is shown as a black circle in Figure 3.1.3C) to generate the segmented neuromelanin-iron complex in SN as shown in Figure 3.1.3G. The region of ferric iron was also obtained by thresholding the T_2 map, which is shown in Figure 3.1.3I. For the direct comparisons, neuromelanin pigments and ferric iron deposits from histological counts are shown in Figure 3.1.3F and Figure 3.1.3H, respectively, which were obtained from Perls' Prussian blue staining (Figure 3.1.3II-2). Spatial separation of neuromelanin-iron complex and ferric iron in SN was feasible with the combining process using mutually complementary MR relaxometries, T_1 , T_2 , and T_2^* .

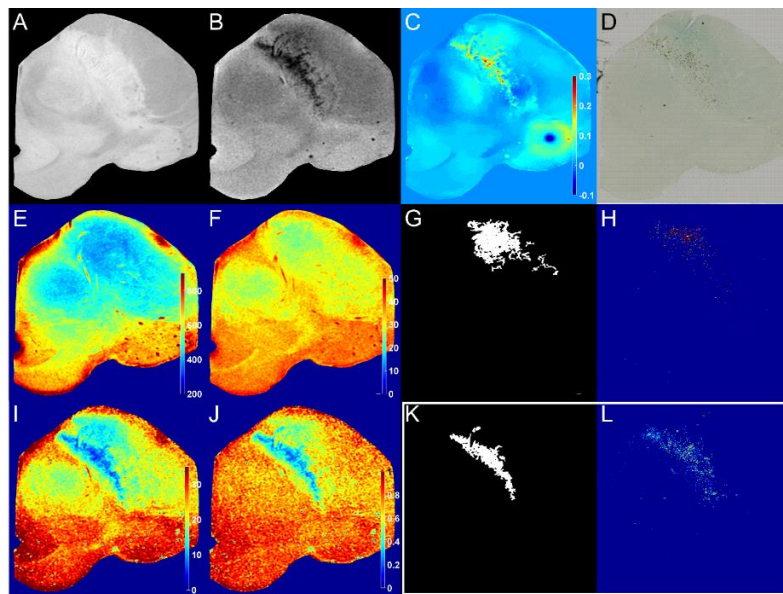


Figure 3.1.5 The multiparametric MRI and co-registered histology to segment iron and neuromelanin distribution of the sample from the left SN tissue of 70F subject. (A) : MT T_1 -weighted image, (B) : SWI, (C) : QSM, (D) : Perls' Prussian blue staining, (E) : T_1 map, (F) : T_2 map, (G) : Iron distribution from T_2 map, (H) : Iron distribution from Perls' Prussian blue staining, (I) : T_2^* map, (J) : T_2^*/T_2 map, (K) : neuromelanin distribution from T_2^* map, (L) : neuromelanin distribution from Perls' Prussian blue staining.

The comparisons between MR parameters and corresponding histological components

The various MRI-derived images and maps are shown in comparison with corresponding neuromelanin pigments and ferric iron deposits extracted from co-registered Perls' Prussian blue staining for the 75F, 70F_L, 86F, and 60M subjects as shown in Figure 3.1.4, Figure 3.1.5, Figure 3.1.6, and Figure 3.1.7, respectively. MRI-derived images included the T_1 weighted images with MT effects (A), SWI (B), QSM (C), T_1 map (E), T_2 map (F), T_2^* map (I), and T_2^*/T_2 map (J). The T_2^*/T_2^2 map (M)

was included in Figure 3.1.6 and Figure 3.1.7, when the T_2^*/T_2 map was apparently insufficient in separating the neuromelanin pigments for the sample with excessively elevated iron concentrations. Iron deposits (H) and neuromelanin pigments (L) were derived from Perls' Prussian blue staining (D). Thresholded regions of neuromelanin-iron complex (K) and ferric iron (G) from respective MRI acquisitions of T_2^*/T_2 map (or T_2^*/T_2^2 map for 60M and 86F) and T_2 map are respectively shown in direct comparison with corresponding histological components.

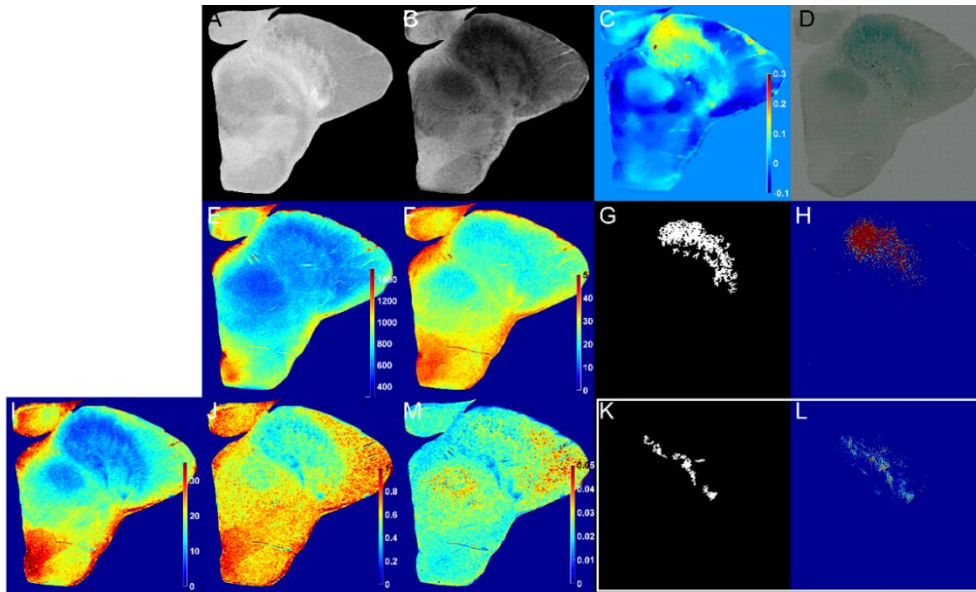


Figure 3.1.6 The multiparametric MRI and co-registered histology to segment iron and neuromelanin distribution of the sample from the 86F subject. (A): MT T_1 -weighted image, (B): SWI, (C): QSM, (D): Perls' Prussian blue staining, (E): T_1 map, (F): T_2 map, (G): Iron distribution from T_2 map, (H): Iron distribution from Perls' Prussian blue staining, (I): T_2^* map, (J): T_2^*/T_2 map, (K): neuromelanin distribution from T_2^* map, (L): neuromelanin distribution from Perls' Prussian blue staining, (M): T_2^*/T_2^2 map.

It was generally observed that both paramagnetic neuromelanin-iron complex and ferric iron contribute to significant T_2^* shortening, which are both seen from SWI (B) and T_2^* (I) maps for all cases. The QSM (C) showed that the white matter containing myelin has negative magnetic susceptibility value with the diamagnetic property. On the other hand, ferric iron rich areas, such as the substantia nigra pars reticulata (SNr) and red nucleus, and neuromelanin-iron complex rich area, such as SNc were manifested as paramagnetic substances with positive magnetic susceptibility value. Positive magnetic susceptibility values from the QSM (C) in the regions with neuromelanin-iron complex and ferric iron support the iron chelation to neuromelanin. The area with ferric iron pigments was generally observed

to have reduced T_2 (F) and T_2^* (I) values, while the region with neuromelanin-iron complex appears to have significantly shorter T_2^* (I) values. T_1 (E) values were not specifically correlated with neuromelanin pigments in this post-mortem study as shown in Table 3.1.1. The hyperintense area in T_1 weighted images with various MT effects appears to overlap only with the non-myelinated SN region instead for all cases.

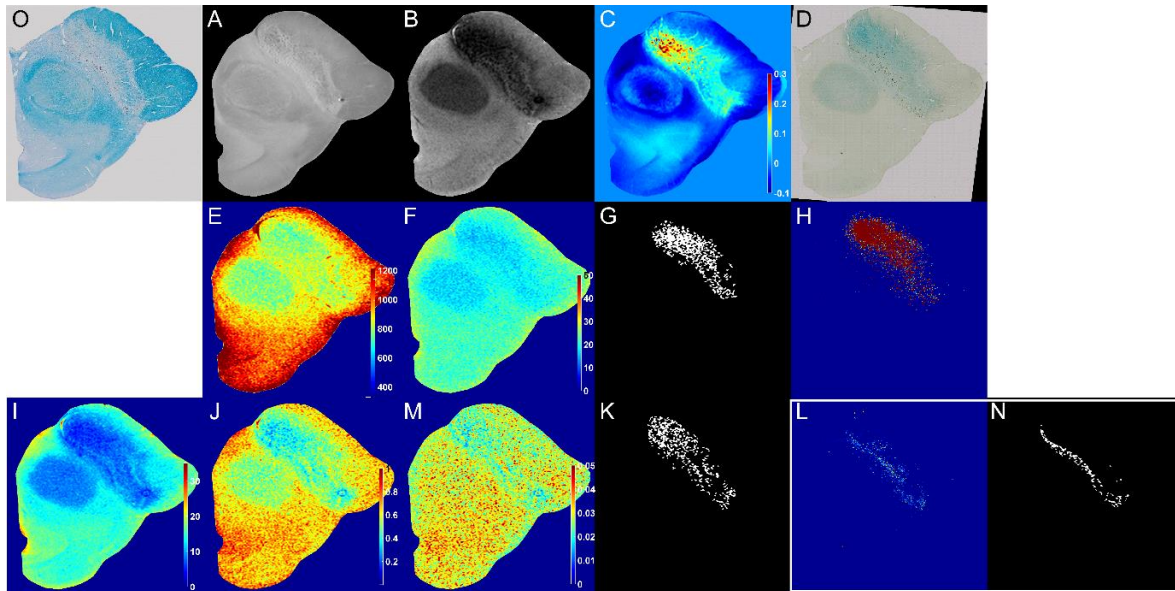


Figure 3.1.7 The multiparametric MRI and co-registered histology to segment iron and neuromelanin distribution of the sample from the 60M subject. (A): MT T_1 -weighted image, (B): SWI, (C): QSM, (D): Perls' Prussian blue staining, (E) : T_1 map, (F) : T_2 map, (G) : Iron distribution from T_2 map, (H) : Iron distribution from Perls' Prussian blue staining, (I) : T_2^* map, (J) : T_2^*/T_2 map, (K) : neuromelanin distribution from T_2^* map, (L) : neuromelanin distribution from Perls' Prussian blue staining, (M) : T_2^*/T_2^2 map, (N) : neuromelanin distribution from excluding iron distribution (G) from thresholded T_2^*/T_2^2 map (K), (O) : LFB staining.

On the contrary, T_2^*/T_2 map (J) and correspondingly thresholded neuromelanin-iron complex mask (K) directly co-localized with histology-referenced region with neuromelanin pigments (L) from Perls' Prussian blue staining (D) as shown in Figure 3.1.4 and Figure 3.1.5. For the 86F SN sample with highly elevated count of iron deposits, the iron contribution appeared to persist in T_2^*/T_2 map as shown in Figure 3.1.6J, but the region of neuromelanin-iron complex was distinguishable from that of ferric iron in the T_2^*/T_2^2 map as shown in Figure 3.1.6M. The correspondingly thresholded neuromelanin-iron complex mask was shown in Figure 3.1.6K and compared with respect to the histology-referenced region of neuromelanin pigments in Figure 3.1.6L. For the sample from the 60M subject, which showed

the highest iron deposits, the region of ferric iron and neuromelanin-iron complex were not separated even in the T_2^*/T_2^2 map as shown in Figure 3.1.7M. However, high ferric iron deposits (H) distinctively showed up on the T_2 map (F), so that excluding the iron rich area with low T_2 values (G) from the T_2^*/T_2^2 -thresholded area (K) generated Figure 3.1.7N, which showed the similar co-localization with respect to the histology-referenced region of neuromelanin pigments in Figure 3.1.7L. A significantly larger portion of myelinated areas was observed within the 60M SN as shown in Figure 3.1.7O, which contributed the shrinkage of the hyperintense area in T_1 weighted image with MT effects (Figure 3.1.7A).

Direct correlations between MR parameters and histological components

The partial correlation coefficients for all subjects (40M, 60M, 70F_L, 70F_R, 75F, and 86F) are summarized in Table 3.1.1. It was generally observed that the neuromelanin pigments are more significantly correlated with T_2^* than T_1 or T_2 . The ferric iron deposits are more sensitive to T_2 and T_2^* than T_1 . Consistently, T_2^*/T_2 (or T_2^*/T_2^2 for the highly iron concentrated case of 60M and 86F) showed the highest partial correlation coefficient with neuromelanin pigments than any other MR-derived parameters. The trends of correlation coefficient change from T_2^* to T_2^*/T_2 (or T_2^*/T_2^2) with respect to neuromelanin pigments and ferric iron deposits for all six samples were plotted in Figure 3.1.8. The partial correlation coefficients from T_2^* to T_2^*/T_2 (or T_2^*/T_2^2) were significantly improved for the neuromelanin pigments but worsened for the ferric iron deposits, verifying the efficacy of combining mutually complementary MR relaxometries in segmenting the region of neuromelanin-iron complex. The p values of paired-sample t -tests for the change of partial correlation coefficients were less than 0.05 for both ferric iron deposits and neuromelanin pigments. At the same time, T_2 values were only significantly correlated with the corresponding ferric iron deposits, but not necessarily with the neuromelanin pigments.

Even with the limited sample sizes of this study, it was observed that the counts of neuromelanin pigments showed an increasing trend with age as plotted in Figure 3.1.9A, which is consistent with previous reports [24, 29]. To evaluate the variation of iron load on individual neuromelanin, the T_2^* reduction per neuromelanin, $\beta_{\text{neuromelanin}}$ values of the multiple linear regression model for each subject, were plotted in Figure 3.1.9B. In contrast to the linear increase of counted neuromelanin pigments in human SN, the $\beta_{\text{neuromelanin}}$ did not show the monotonic trend with normal aging.

Table 3.1.1 PCC of multimodal MRI with respect to neuromelanin and iron distributed within SN.

PCC(40M)	T_1 map	T_2 map	T_2^* map	SWI	QSM	T_2^*/T_2 map	T_2^*/T_2^2 map
NM							
SNc	0.04	0.01	-0.52*	-0.54*	0.32*	-0.70*	
SN	-0.03	0.25*	-0.28*	-0.21*	0.04	-0.63*	
Iron							
SNc	-0.52*	-0.61*	-0.58*	-0.57*	0.54*	-0.23	
SNr	-0.32*	-0.44*	-0.43*	-0.42*	0.42*	-0.22	
SN	-0.37*	-0.46*	-0.47*	-0.45*	0.44*	-0.26*	
PCC(60M)							
NM							
SNc	0.00	-0.09	-0.42*	-0.43*	0.28*	-0.48*	-0.49*
SN	-0.10	-0.18**	-0.39*	-0.37*	0.39*	-0.45*	-0.43*
Iron							
SNc	-0.12	-0.61*	-0.60*	-0.59*	0.25*	-0.53*	-0.26**
SNr	-0.34*	-0.62*	-0.67*	-0.68*	0.35*	-0.67*	-0.41*
SN	-0.32*	-0.61*	-0.65*	-0.65*	0.29*	-0.64*	-0.39*
PCC(70FR)							
NM							
SNc	-0.11	-0.08	-0.68*	-0.68*	0.50*	-0.74*	
SN	-0.12	-0.05	-0.64*	-0.65*	0.55*	-0.73*	
Iron							
SNc	-0.28*	-0.45*	-0.45*	-0.41*	0.41*	-0.30*	
SNr	-0.29*	-0.28*	-0.60*	-0.60*	0.60*	-0.65*	
SN	-0.27*	-0.35*	-0.52*	-0.51*	0.44*	-0.48*	
PCC(70FL)							
NM							
SNc	0.05	0.06	-0.38*	-0.46*	0.40*	-0.43*	
SN	0.05	0.14	-0.45*	-0.47*	0.35*	-0.57*	
Iron							
SNc	-0.03	-0.24*	-0.07	-0.02	0.16	0.06	
SNr	-0.10	-0.34*	-0.47*	-0.44*	0.37*	-0.49*	
SN	-0.13	-0.36*	-0.25*	-0.18**	0.34*	-0.10	
PCC(75F)							
NM							
SNc	0.29*	0.35*	-0.27*	-0.18**	-0.05	-0.46*	
SN	0.45*	0.51*	-0.08	0.23*	-0.14*	-0.50*	
Iron							
SNc	-0.13	-0.17**	-0.22*	-0.17**	0.04	-0.13	
SNr	0.08	0.12	-0.06	0.04	0.09	-0.16**	
SN	0.02	0.04	-0.11*	-0.02	0.07	-0.15*	
PCC(86F)							
NM							
SNc	0.07	0.23*	-0.13	-0.16	-0.13	-0.43*	-0.60*
SN	0.05	0.27*	0.01	0.09	-0.40*	-0.22*	-0.43*
Iron							
SNc	-0.16	-0.49*	-0.59*	-0.60*	0.47*	-0.64*	-0.33*
SNr	-0.10	-0.34*	-0.47*	-0.44*	0.37*	-0.49*	-0.24*
SN	-0.11*	-0.38*	-0.50*	-0.47*	0.32*	-0.53*	-0.26*

*: $p < 0.0001$, **: $p < 0.005$. NM: neuromelanin. PCC: Pearson partial correlation coefficients.

3.1.4 Discussions and Conclusions

The iron load on neuromelanin within the SN is generally known for reducing the iron toxicity, and resulting neuromelanin-iron complex in the SN can act as an endogenous paramagnetic magnetic susceptibility perturber. [2, 6, 7] In this study, the dependence of MR relaxometry on the underlying geometry of paramagnetic perturbers was observed to provide a unique opportunity for specifically detecting neuromelanin-iron complex in the SN. The positive magnetic susceptibility values in the region of neuromelanin pigments from QSM ascertained the iron chelation of neuromelanin in SN which was consistent results with previous studies using Electron paramagnetic resonance (EPR) and Moessbauer spectroscopy [2, 3, 4]. In addition, the diamagnetic myelin region showed negative magnetic susceptibility values, which is consistent with previous findings [30, 31, 32]. The region of reduced T_2 values mostly coincided with high ferric iron deposits, not necessarily with the region of neuromelanin pigments, as T_2 values tend to increase as the size of paramagnetic perturbers increase [21, 33, 34]. On the other hand, the region of low T_2^*/T_2 (T_2^*/T_2^2) values showed improved correlations with respect to neuromelanin pigments compared to corresponding T_2^* values. Consequently, separate segmentations of ferric iron from the T_2 map and neuromelanin-iron complex from the T_2^*/T_2 map (or T_2^*/T_2^2 map) were possible in SN, whose mask was determined from the T_1 weighted MR image.

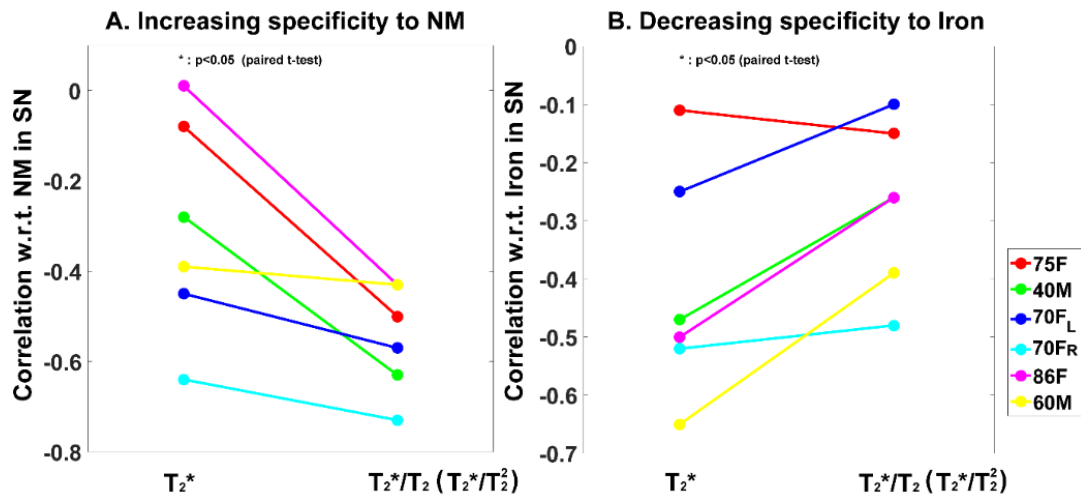


Figure 3.1.8 The partial correlation coefficients of T_2^* and T_2^*/T_2 (T_2^*/T_2^2) with respect to neuromelanin and iron distribution. (A): The partial correlation coefficients of T_2^* and T_2^*/T_2 (T_2^*/T_2^2 for the sample from the 60M and 86F subjects) with respect to histological neuromelanin distribution for six samples. (B): The partial correlation coefficients of T_2^* and T_2^*/T_2 (T_2^*/T_2^2 for 60M and 86F) with respect to histological iron distribution for six samples.

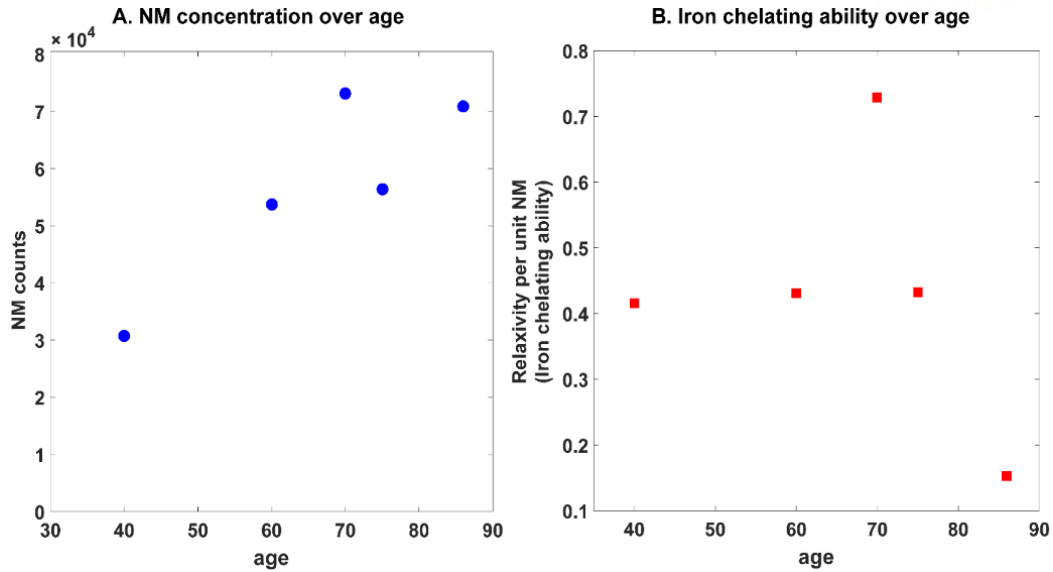


Figure 3.1.9 The neuromelanin concentrations and iron-chelating ability per unit neuromelanin versus ages. (A): The neuromelanin concentrations versus age for six samples. (B): The partial regression coefficient ($\beta_{\text{neuromelanin}}$) (iron chelating ability per unit neuromelanin) versus ages for six samples. neuromelanin and ferric iron concentrations and corresponding T_2^* values from five slices for each sample were merged and analyzed to obtain (A) and (B).

It is worthwhile to elaborate our experimental findings on T_1 weighted images with MT effects and its relevance in delineating neuromelanin distributions in the SN. It was consistently observed with all samples that hypointense areas of T_1 weighted images with MT effects both inside and outside of SN coincided with myelinated tissue regions from corresponding LFB staining as shown in Figure 3.1.10. As the MT effect provides interaction between protons in free and restricted pools to saturate mobile protons, our observation is consistent with the widely applied method to measure myelin content [20]. We also found that the region of myelin and neuromelanin pigments in the SN do not overlap with each other. Hyperintense areas on T_1 weighted images with MT effects may be interpreted as non-myelinated regions, which are likely to coincide with the region of neuromelanin pigments. But they did not directly correlate with the density of neuromelanin pigments. For example, in samples such as the 60M with highest iron deposits from Perls' Prussian blue staining, a significantly larger portion of myelinated areas was observed within the SN, which may be interpreted as a shrinkage of the region of neuromelanin in conventional MT- T_1 based neuromelanin sensitive imaging as shown in Figure 3.1.7A and Figure 3.1.7O. However, the counts of neuromelanin pigments in the 60M SN were not significantly different from the rest of the samples. Considering that the iron deposition and loss of neuromelanin-containing dopaminergic neurons within the SN are pathologically significant in the pathogenesis of PD, it appears to require extra precautions, when interpreting only MT- T_1 based neuromelanin sensitive

imaging as a direct surrogate for the loss of neuromelanin-containing dopaminergic neurons in monitoring PD progression.

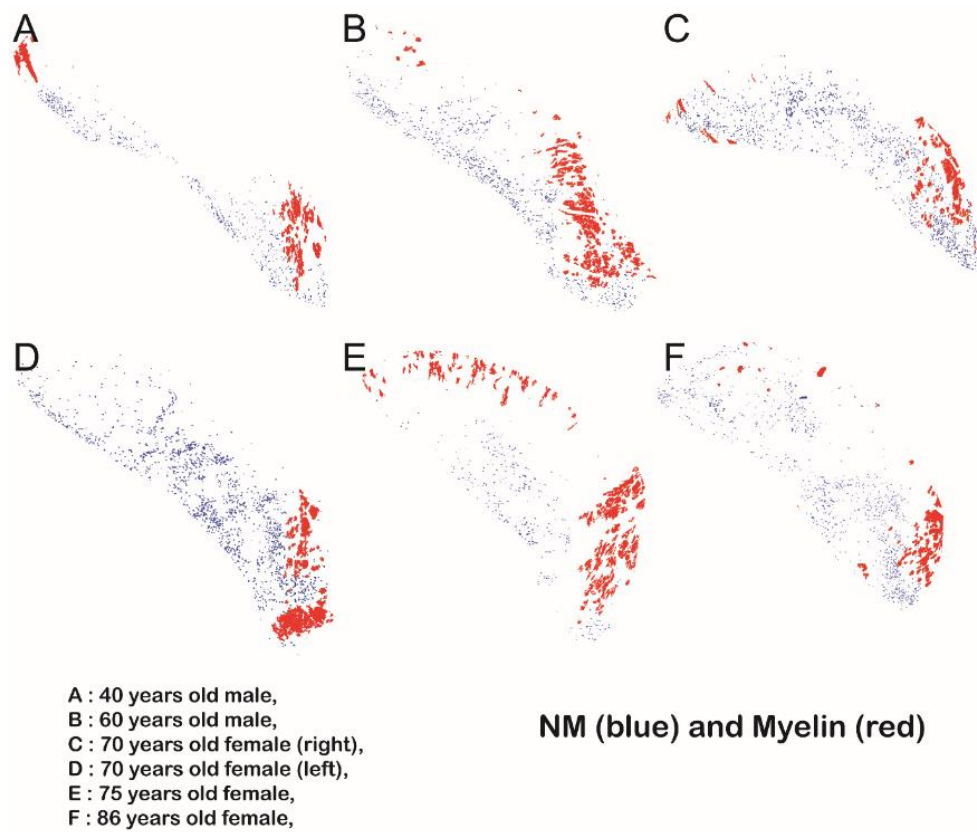


Figure 3.1.10 The neuromelanin and myelin distribution from histology. (A): neuromelanin (blue) and myelin (red) distribution of 40M, (B): neuromelanin (blue) and myelin (red) distribution of 60M, (C): neuromelanin (blue) and myelin (red) distribution of 70F_R, (D): neuromelanin (blue) and myelin (red) distribution of 70F_L, (E): neuromelanin (blue) and myelin (red) distribution of 75F, (F): neuromelanin (blue) and myelin (red) distribution of 86F.

The interpretation of T_2^*/T_2 map in delineating neuromelanin-iron complex at elevated ferric iron contents should be noted because the spatially effective clustering of the ferric iron will be inevitable even without chelation to neuromelanin. For instance, the counts of ferric iron deposits of SN samples from 86F and 60M subjects were significantly larger compared to the other samples. For the sample from the 86F, the T_2^*/T_2^2 mapping was required in differentiating neuromelanin-iron complex from ferric iron. For the sample from the 60M with the highest iron stained deposits, even T_2^*/T_2^2 mapping was insufficient. However, iron deposits distinctively showed up on the T_2 map, so combining the

T_2^*/T_2^2 and T_2 information enabled a specific visualization of neuromelanin-iron complex even at high iron deposits.

The gradual increase of neuromelanin with aging has been reported [24, 29], which is consistent with our findings. However, the reduction of T_2^* values per neuromelanin pigment ($\beta_{\text{neuromelanin}}$), which may reflect the variation of iron load on individual neuromelanin [35], did not necessarily correlate with the counts of neuromelanin pigments or iron deposits in this study. The $\beta_{\text{neuromelanin}}$ values for the samples from the 40M, 60M, and 75F were similar. The $\beta_{\text{neuromelanin}}$ of the samples from the 70F and 86F with the largest neuromelanin counts were significantly larger and smaller than those of the rest, respectively, with the 10-fold increase of ferric iron counts in the 86F compared to the 70F sample, but with similar neuromelanin pigments counts. The change in the amount of iron load on the neuromelanin with aging is a very important but controversial issue. The neurodegeneration with the loss of neuromelanin-containing neurons may be facilitated with iron overload within neuromelanin, but no *in vivo* method exists that can characterize the amount of iron chelation to the individual neuromelanin [36, 37]. With further optimization and more samples including PD SN, this technique may be efficiently used to identify the approximate iron concentration within SN by evaluating the reduction of T_2^* on neuromelanin-iron complex and ferric iron, respectively.

There are several limitations in our study. First, it should be noted that post-mortem MT- T_1 based contrasts with formalin fixation may be different from that of corresponding *in vivo* contrasts [38]. As the formalin fixation changes the chemical environment of tissue and water movement, the effect of formalin fixation has been reported to reduce the MT ratio of the brain tissue [39, 40]. Further study must be pursued in validating post-mortem and *in vivo* MT- T_1 based contrasts with each other. Second, the ability to identify the ratio between reactive ferrous (Fe^{2+}) iron and non-reactive ferric (Fe^{3+}) iron is another important issue. Turnbull's blue staining is needed to observe ferrous (Fe^{2+}) iron and its correlation to MR relaxation parameters should be examined. It has been reported that Fe^{3+} contributes 10 times more to the T_2^* reduction than Fe^{2+} , so it is likely that most of observed T_2^* reduction comes from the Fe^{3+} [41]. However, it is difficult to separate the contribution of Fe^{2+} from that of Fe^{3+} . Third, for the clinical applications, lengthy acquisition time for T_2 and T_2^* mapping may not be ideal, and future studies should be conducted to optimize echo times so that the combination of T_2 and T_2^* weighted images at particular echo times can be used to delineate neuromelanin-iron complex except ferric iron instead of lengthy relaxation mapping procedures.

In conclusion, our findings using combined transverse MR relaxometries suggest that paramagnetic neuromelanin-iron complex can be separated from ferric iron in SN, based on the MC simulation for MR relaxometry alteration due to the effective size differences of paramagnetic perturbers. Because the degeneration of neuromelanin-iron complex and the increase of iron deposition within the SN are the

most important pathological features of PD, this technique may be a useful tool to evaluate the progressive change of neuromelanin and iron distribution with the advance of PD.

The original source of Chapter 3.1 is the article, Lee, H., Baek, S. Y., Chun, S. Y., Lee, J. H., & Cho, H. (2018). Specific visualization of neuromelanin-iron complex and ferric iron in the human post-mortem substantia nigra using MR relaxometry at 7T. *Neuroimage*, 172, 874-885..

3.2 Determination of neuromelanin distribution in the dorsal area of substantia nigra pars compacta using T_2 and T_2^* mismatch

3.2.1 Introduction

Neuromelanin is a dark, pigmented granule expressed within the dopaminergic neurons of the substantia nigra pars compacta (SNc) [1, 3]. Neuromelanin plays a major function in the protection of neurons by storing metals such as iron, copper, and zinc [6, 7]. Parkinsonism is a clinical syndrome characterized by tremor, bradykinesia, and rigidity [42]. Specifically, Parkinson's disease is a typical variety of Parkinsonism involving the loss of pigmented dopaminergic neurons mainly in the substantia nigra (SN) [1, 43]. The ability to visualize the gradual changes in neuromelanin distribution within the SN is a potentially useful metric to monitor nigral degeneration in Parkinson's disease patients.

Neuromelanin binds iron molecules, forming neuromelanin-iron complexes, and is one of the endogenous paramagnetic perturbers in the SN [3, 13, 44]. Thus, magnetic resonance imaging (MRI) could be a useful imaging tool to detect the distribution of these paramagnetic neuromelanin-iron complexes [2, 45]. Recent development of neuromelanin-sensitive MRI using T_1 -weighted scans with additional magnetization transfer (MT) contrast preparation pulses can generate hyperintense signals adequately sensitive to detect neuromelanin localization [17, 46, 47, 48]. Neuromelanin-specific contrast results from both T_1 shortening and MT effects [16]. In addition, nigrosome 1 is considered a cluster of neuromelanin-containing dopaminergic neurons, which are preferentially affected by Parkinson's disease progression [9]; this cluster is characterized by a dorsolateral hyperintense region with a swallow-tail appearance on T_2^* - and susceptibility-weighted images (SWI) from healthy controls [49, 50]. An increase in iron deposition in Parkinson's disease may cause a progressive loss of the tail sign [51]. Transverse MR relaxometry and quantitative susceptibility mapping (QSM) have been employed to characterize iron deposition within the SN to aid diagnosis of Parkinson's disease [46, 52, 53, 54].

The use of MRI, however, as a noninvasive modality to identify and differentiate the spatial distribution of neuromelanin and ferric iron within the SN remains controversial. Due to increased accumulation of total iron content in the SN during aging and Parkinson's disease progression, the spatial distribution of neuromelanin and deposition of ferric iron molecules can overlap within the SN. Both neuromelanin and deposited iron act as iron clusters of different sizes with paramagnetic properties leading to similar MR signal contrast [2, 16, 45]. Additionally, the SN is a relatively small area located in the midbrain, making delineation of the region difficult; for this reason, neuromelanin may be distributed in areas with the size of only a few voxels when visualized by conventional *in vivo* MRI [22,

57]. In Parkinson's disease, dopaminergic neuron loss, an accumulation of iron molecules, and progressive atrophy of cerebral tissue can further confound the interpretation of spatial localization through *in vivo* MRI [56].

More recently, studies assessing postmortem tissue using 7T MRI and co-registered histological analysis have reported that neuromelanin significantly shortens the T_2^* , but not necessarily the T_2 values [22, 57]. Meanwhile, ferric iron deposition has been observed to shorten both transverse relaxation times [57]; this mismatch of T_2 and T_2^* values has previously been utilized to investigate the spatial separation between neuromelanin and ferric iron deposition in postmortem tissue of the SN in normal brains [57].

Building upon these previous observations, we hypothesized that the T_2 and T_2^* mismatch would be a useful indicator to assess dorsal neuromelanin distribution of normal and diseased SN tissue. Both high- and low-resolution MR transverse relaxometries were performed at 7T to investigate the cause of the T_2 and T_2^* mismatch in normal and depigmented postmortem SN tissue. Furthermore, the feasibility of use and clinical applications of this method *in vivo* were explored at 3T.

3.2.2 Methods

This study was approved by the Institutional Review Boards of Pusan National University Yangsan Hospital and Ulsan National University of Science and Technology. MRI experiments were conducted with healthy volunteers and Parkinson's disease patients in accordance with the guidelines established by the Declaration of Helsinki. All participants provided written informed consent prior to enrollment in the study.

3-dimensional histological reconstruction to delineate neuromelanin and iron distribution

The histology data were obtained from the SN of a brain from a normal subject (a 60-year-old male). This tissue sample was also used in our previous study [57]. There were high amounts of both neuromelanin and ferric iron deposits within the SN detected by Perls' Prussian blue staining. Binary masks were generated to assess the distribution of neuromelanin and ferric iron by thresholding three color (RGB) channels of images captured from 30 sparsely stained sections. These 30 binary images were sequentially co-registered to corresponding T_1 -weighted images of 15 slices [22]. The midbrain structures (thickness = 7.5 mm) were reconstructed in three dimensions using a 3D Slicer interface (MATLAB-bridge, www.slicer.org) to identify the distribution of neuromelanin and ferric iron deposition. The dark pigments of neuromelanin were represented by green dots, while the ferric iron molecules stained with Perls' Prussian blue staining were represented by red dots within the 3D

transparent structure. To detect dopaminergic neurons, tyrosine hydroxylase immunohistochemistry of tissue sections was also performed using a rabbit anti-tyrosine hydroxylase antibody (AB152, Millipore Corporation, Temecula, CA).

Postmortem midbrain tissue collection

Postmortem midbrain samples containing the SN were obtained from two subjects (75-year-old and 86-year-old females) with no diagnosis of neurodegenerative diseases who had joined the Pusan National University Anatomical Donation Program; the brain of one patient (51-year-old male) with genetically confirmed Perry syndrome (*DCTN1* T78C mutation) was obtained from the Pusan National University Hospital Brain Bank [58]. The two normal postmortem midbrain tissue samples had been fixed in formalin solution for two years, while the one diseased brain had been fixed for four years. In the midbrain tissue stored for two to four years in formalin, the redistribution of iron among different molecules may occur, which can affect the paramagnetic complexes formed by iron chelation, changing the absolute transverse relaxation times but maintaining contrast of MR transverse relaxometries within brain tissues [59, 60].

Postmortem MRI

Sample preparation for postmortem assessment with a preclinical 7T MR scanner (BioSpec, Paravision 6.0, Bruker, Ettlingen, Germany) was conducted according to a previous protocol [57]. For the acquisition of MRI scans, the midbrain tissues were positioned in a 50 mL syringe and the imaging slice was aligned perpendicular to the main B_0 field.

The T_2 map was acquired using a multi-spin multi-echo (MSME) pulse sequence with the following parameters: repetition time (TR) = 6,000 ms; echo time (TE) = 8 ~ 384 ms in steps of 8 ms; and single-slice excitation for five slices. In multi-slice acquisition, multiple off-resonance excitation pulses contribute to signal reduction in adjacent slices [61, 62]; hence, the multi-slice acquisition to generate the T_2 map based on a modified Rapid Acquisition with Relaxation Enhancement (RARE) sequence may cause unintended MT effects on each slice compared to single-slice acquisition techniques [61]. The T_2^* map was generated by a multiple gradient echo (MGE) pulse sequence with the following parameters: TR = 2,000 ms; TE = 3.3 ~ 81.2 ms in steps of 4.1 ms; and excitation of 20 slices by multi-slice acquisition. The T_2 and T_2^* maps were fitted mono-exponentially from the respective exponential curves based on the formula $S(t) = S_0 e^{-\frac{t}{T_2}} + C$ and $S(t) = S_0 e^{-\frac{t}{T_2^*}} + C$, using in-house-developed MATLAB (MathWorks, Natick, MA, USA) code. After co-registration between the T_2 and T_2^* maps using a 2D rigid transformation of rotation and translation in MATLAB, the T_2^*/T_2 and T_2^*/T_2^2 maps were calculated, voxel-wise, from the T_2 and T_2^* maps to separate the distribution of iron clusters based

on their size differences.

For QSM, phase data from the MGE pulse sequences of five tilted orientations were merged to generate one final magnetic susceptibility map. The imaging parameters for the MGE sequence of QSM algorithm were the same as those used to generate the T_2^* map. Temporal phase unwrapping was performed using the phase information of the first three echoes. The spatial phase unwrapping was performed by the Laplacian-based method [26]. Background field removal was implemented using the Laplacian boundary value (LBV) method [27]. The inverse problem of converting five measured field maps to one merged susceptibility map was solved by the calculation of susceptibility through multiple orientation sampling (COSMOS) technique [63]. For the brain from the 75-year-old female subject, the susceptibility map was also generated by morphology enabled dipole inversion (MEDI) from one field map [28].

Neuromelanin-sensitive MRI was performed with a RARE pulse sequence with the following parameters: TR = 800 ms; TE = 8 ms; and multi-slice acquisition. The additional MT pulse for neuromelanin-sensitive MRI was applied at a flip angle of 600° and a frequency offset of 600 Hz. The common parameters used for postmortem MRI were as follows: isotropic in-plane resolution of $136 \times 136 \mu\text{m}$ (field of view = $35 \times 35 \mu\text{m}$ and matrix size = 256×256); slice thickness = 0.5 mm. The same slice geometry was maintained across each of the pulse sequences for direct mutual comparisons.

Histology

Histological staining was performed as the gold-standard reference to compare the results from postmortem MR relaxometry. To prepare cryosections, tissues were sequentially immersed in 10%, 20%, and 30% sucrose solutions in phosphate buffered saline (PBS) until tissues sank in each solution to minimize the formation of intracellular ice crystals. After the tissues sank in the 30% sucrose solution, the cryoprotected tissues were rapidly frozen in the dry ice box. Adjustment of the angle and position of each tissue sample was performed using the corresponding MR images for reference. Cryosections were cut using Cryostat (CM1950, Leica Biosystems, Nussloch, Germany) at $50 \mu\text{m}$ (approximately 1/10th the thickness of the corresponding MR image). The tissues were photographed during cryosectioning to determine the region where dark pigmentation was visible.

Staining of the ten sectioned slides corresponding to each MR image was performed; Perls' Prussian blue staining was used to assess the distribution of ferric iron molecules, Luxol fast blue staining was performed for myelin identification, and Cresyl violet counterstaining was performed to identify neurons. For Perls' Prussian blue staining, a 1:1 mixture of 20% HCl solution and 20% potassium ferrocyanide solution was applied to tissue for 30 min. Luxol fast blue staining was performed as follows: filtered 0.1% Luxol fast blue solution was applied and slides were placed in a 65°C oven for

seven hours, followed by differentiation in 0.05% lithium carbonate solution, then counterstained with filtered 1% Cresyl violet solution. The stained slides were scanned using an Olympus Slide virtual microscopy (Olympus Optical Co. Ltd., Tokyo, Japan) at 10× magnification.

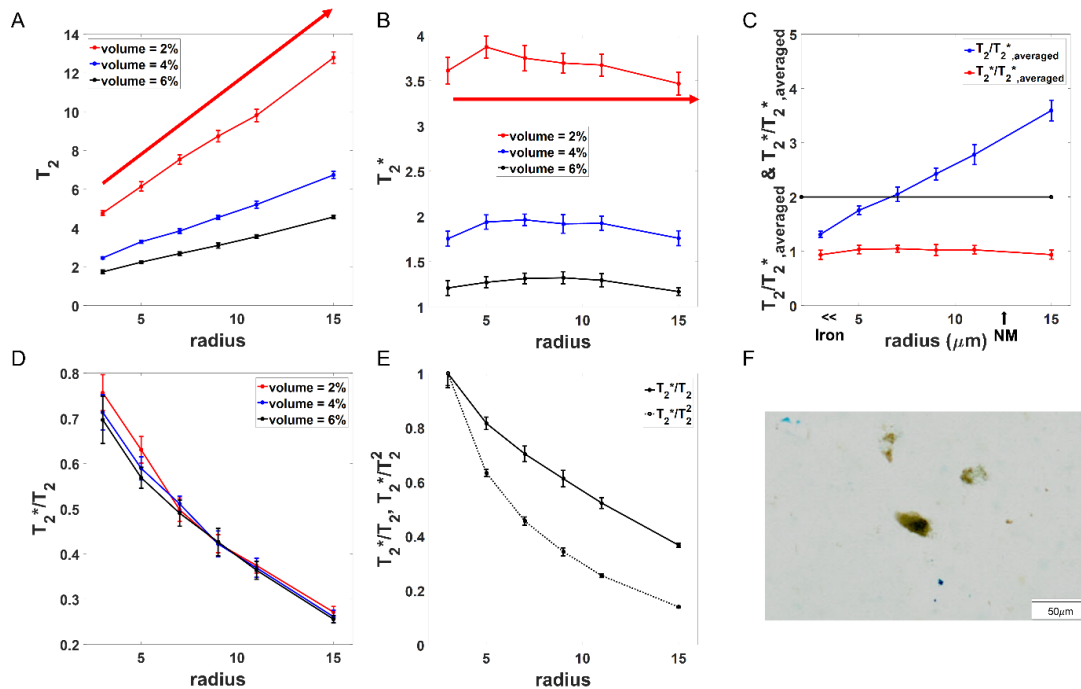


Figure 3.2.1 Monte Carlo simulation for transverse MR relaxation times based on the size of randomly distributed paramagnetic spherical particles. (A): T_2 values (ms) based on particle size and fractional volume; (B): T_2^* values (ms) based on particle size and fractional volume; (C): T_2/T_2^* ,_{averaged} and T_2^*/T_2^* ,_{averaged} to validate the two-fold thresholding of T_2 ; (D): T_2^*/T_2 values based on particle size and fractional volume; (E): The trends of the T_2^*/T_2 and T_2^*/T_2^2 ratios based on particle size, with the same 6% fractional volume; (F): Micrographs of Perls' Prussian blue staining showing the size of neuromelanin pigments (dark brown) and iron molecules (blue). MR = magnetic resonance.

Monte Carlo simulation for the validation of T_2 and T_2^* threshold values

To validate the numerical basis of the threshold T_2 and T_2^* values, Monte Carlo simulations were performed, which assess the contribution of randomly distributed paramagnetic clusters in transverse MR relaxometries. The spherical clusters had radii of 3, 5, 7, 9, 11, 13, or 15- μm , with fractional volumes of 2, 4, and 6% of the entire three-dimensional space. The whole dimensions of the simulation space were determined by the radii of spherical clusters and fractional volumes with 50 particles of the set radius. The susceptibility of paramagnetic perturbbers was set at 2.857×10^{-7} cgs [64]. It should be noted that precise recommendations for susceptibility value settings for various forms of iron molecules in the SN have not been reported. The present study used a representative value previously reported for

ultrasmall iron oxide nanoparticles; thus, the absolute value of transverse relaxation times based on simulations may not be representative of experimental values from *ex vivo* and *in vivo* measurements. Simulations were performed, but were only used to determine the threshold ratio of T_2 and T_2^* values to delineate iron clusters. Specifically, simulation procedures consisted of 60,000 protons randomly diffusing, with a diffusion constant of $1 \mu\text{m}^2/\text{ms}$. They continuously diffused within the three dimensional space, passing through the perturbed magnetic field caused by all the clusters in the simulation space at step times of 0.1 ms until the echo times of the simulations were reached. The echo times for spin-echo simulation were 8 ~ 56 ms in steps of 8 ms; echo times for gradient simulation were 3 ~ 27 ms in steps of 4 ms. The accumulated phase from the random proton diffusion was calculated across the entire simulation space. Corresponding T_2 and T_2^* values were mono-exponentially fitted following signal reduction for both spin-echo and gradient-echo. T_2 and T_2^* were then plotted against the size of the paramagnetic perturbers for each fractional volume. The practical size of neuromelanin pigments and deposited iron molecules were identified by microscopy following Perls' Prussian blue staining (Figure 3.2.1F).

The overall results of the Monte Carlo simulation are shown in Figure 3.2.1. The results of Monte Carlo simulations of paramagnetic perturbers with magnetic susceptibility of iron oxide revealed that increases of T_2 correlated with increases in the radius of the iron clusters with the same fractional volumes (Figure 3.2.1A). For T_2^* , the value was constant as the radius changed (Figure 3.2.1B). In Figure 3.2.1C, to validate the twofold threshold for the T_2 versus the T_2^* map, thresholding of T_2^* and T_2 values was performed by setting the threshold value of $T_{2,\text{threshold}}$ at $2T_{2^*,\text{threshold}}$, respectively. The threshold value for T_2^* could be empirically determined to include clusters of any size in the SN, however, iron clusters of larger sizes were excluded from the corresponding T_2 thresholding. In this way, voxels that simultaneously satisfied the conditions of $T_2^* < T_{2^*,\text{threshold}}$, and $T_2 > T_{2,\text{threshold}}$ ($T_{2,\text{threshold}} = 2T_{2^*,\text{threshold}}$) were selected to delineate the area of significant T_2 and T_2^* mismatch. Therefore, conceptually speaking, neuromelanin-iron complex formed an enlarged iron cluster in the SN that would satisfy the condition ($T_2 - T_2^* > T_{2^*,\text{threshold}}$), and could be separated by subtracting the corresponding thresholded T_2 mask from the T_2^* mask for *ex vivo* and *in vivo* results.

T_2 and T_2^* mismatches assessed by postmortem MRI

To verify the feasibility of visualizing the neuromelanin distribution at a clinically available resolution, postmortem MRI was also performed with a correspondingly lower in-plane spatial resolution ($1.09 \times 1.09 \times 0.5 \text{ mm}$; matrix size = 32×32). The T_2^*/T_2^2 map was generated by combining the acquired low-resolution T_2^* map (32×32) with the down-sampled T_2 map (32×32). The T_2^* map was thresholded at a specific value for each sample to include all iron molecules of ferric iron and

neuromelanin, as levels of formalin fixation differed between each sample. Correspondingly, the T_2 map was generated using a two-fold higher threshold value than the T_2^* map, consistent with simulations. The manual-ROI mask of the whole SN taken from the T_2^* map was overlapped with such binary masks to exclude other iron-rich areas outside the SN, such as the red nucleus, then the thresholded T_2 mask was subtracted from the T_2^* mask for both the high- and low-resolution images. In this way, the voxels that simultaneously satisfied the conditions of $T_2^* < T_{2^*,\text{threshold}}$, and $T_2 > T_{2,\text{threshold}}$ ($T_{2,\text{threshold}} = 2T_{2^*,\text{threshold}}$) were selected. Based solely on the determined $T_{2^*,\text{threshold}}$, the corresponding regions of significant T_2 and T_2^* mismatch were identified. The distribution of dark neuromelanin pigments was binarized by thresholding the RGB channels from the captured image of co-registered cryosectioned block-faces. The overlap between the T_2 and T_2^* mismatch area (T_2^*/T_2^2 map and $T_2^*-T_2$ mask) identified by high- and low-resolution MRI and the binarized neuromelanin distribution segmented from the co-registered cryosectioned block-faces was quantitatively assessed using Dice's similarity coefficient. Furthermore, the segmented regions of apparent T_2 and T_2^* mismatches were directly compared with the susceptibility map generated by QSM, and the Luxol fast blue myelin staining.

LA-ICP-MS for spatial iron mapping

Quantification of iron distribution in a 2-dimensional plane was assessed in postmortem brain tissues using femto-second laser ablation inductively coupled plasma mass spectrometry (LA-ICP-MS). The quadrupole ICP-MS device, iCAP TQ (ThermoFisher Scientific, Bremen, Germany), equipped with a femtosecond laser (1,030 nm) ablation system (J200, Applied Spectra Inc, Fremont, CA, USA) was used to assess the concentration and distribution of ^{56}Fe and ^{13}C in sectioned tissue (50 μm thick) of 75-year-old normal female brain and the depigmented brain. The tissue sections were ablated under the constant flow of helium gas (0.9 L/min). Argon gas, with a flow rate of 0.7 L/min, was used as a carrier gas, which was mixed with the helium after ablation. The spot size of the laser beam was chosen as 50 μm , directed onto a 28 \times 17 mm area of tissue. Line scanning was performed at a velocity of 0.2 mm/s. The time-resolved intensity data for each of the two ions were collected by Qtegra software (v. 2.10.3324.83) provided by the company of the ICP-MS device. The output data from the mass spectrometer were exported as single columns into comma-separated-value (.CSV) files for each trace element. The in-house-developed MATLAB code was used to convert individual intensity values to 2D images showing the concentration and distribution of each element in the tissue sample. To compare the concentration of ^{56}Fe between the two samples, the intensity of ^{56}Fe was normalized voxel-wise by the ratio of intensities of ^{13}C to $^{56}\text{Fe}/^{13}\text{C}$, where ^{13}C was the internal standard, homogeneously distributed throughout the brain tissue.

In vivo MRI and [¹⁸F] FP-CIT PET acquisition

Eight normal subjects and eight idiopathic Parkinson's disease patients who met the diagnostic criteria were included in this study; the normal subject group was comprised of 26- to 63-year-old adults (mean = 48.5, SE = 5.1 years). Parkinson's disease patients ranged in age from 51 to 67 (mean = 61.5, SE = 1.8 years). All Parkinson's disease patients were at Hoehn and Yahr (H-Y) stages I or II, and the duration of disease progression was 1~5 years (mean = 2.4, SE = 0.6 years).

All participants underwent 3T brain MRI (MAGNETOM Skyra, Siemens Medical Solutions, Malvern, PA, USA) at Pusan National University Yangsan Hospital. For all *in vivo* MR images, the same slice geometry and orientation were maintained, and imaging parameters were consistent; the isotropic in-plane resolution was 1 × 1 mm (field of view = 192 × 192 mm, matrix size = 192 × 192), and twelve slices were imaged at 2 mm thickness, with a 0.1 mm slice gap. Axial images were obtained parallel to the anterior commissure and posterior commissure (AC-PC) line, covering the entire midbrain. Among the 12 slices, two slices in which the caudal level of the red nucleus was visible and the neighboring section in the caudal direction without the red nucleus being visible were selected to better elucidate the differences between normal subjects and Parkinson's disease patients [65].

The T_2 map was acquired using a multi spin-echo pulse sequence with the following parameters: TR = 2,000 ms; TE = 10 ~ 150 ms in steps of 10 ms; no average; and acquisition time = 6 min 26 s. The T_2^* map was generated using a multiple-gradient-echo pulse sequence with the following parameters: TR = 406 ms; TE = 3.14 ~ 29.94 ms in steps of 5.49 ms; flip angle = 20°; an average calculated based on two replicate measurements; and acquisition time = 2 min 36 s. The T_2 and T_2^* maps were fitted voxel-wise with the mono-exponential T_2 and T_2^* relaxation curve directly from the Siemens scanner to maintain reproducibility. For *in vivo* experiments, single-slice acquisition of T_2 maps was impossible for several slices due to the limited time of the experiment for those respective patients.

Neuromelanin-sensitive MRI was performed using a 2D spin-echo sequence with an additional MT pulse, with the following parameters: TR = 600 ms; TE = 6.8 ms; an average calculated based on two replicate measurements, and acquisition time = 3 min 53 s. For SWI, the magnitude and phase data were obtained from the same dataset from the T_2^* map with TR = 406 ms and TE = 24.45 ms. The high-pass filtered phase image was produced by subtracting the 2D Hanning low-pass filtered phase image from the original phase image [66]. As the Siemens MR scanner used in this study employs a "left-handed" MR imaging system, the fourth power of the positive phase mask generated from the high-pass filtered phase image was multiplied by the magnitude of the corresponding image to generate the SWI.

All eight Parkinson's disease patients had received ¹⁸F-N-(3-fluoropropyl)-2β-carboxymethoxy-3β-(4-iodophenyl) nortropane (FP-CIT) positron emission tomography (PET) scans within 6 months of their MR scan (mean = 3.5, SE = 0.7 months). PET/CT scans were acquired 180 min after intravenous

injection of 5 mCi (185 MBq) of [^{18}F] FP-CIT using a Biograph 40 TruePoint PET/CT scanner (Siemens Medical Solutions, Malvern, PA, USA) in the 3D scanning mode. PET images were reconstructed using an iterative ordered-subset expectation-maximization algorithm, with a 4 mm Gaussian filter, with a reconstructed matrix size of 256×256 .

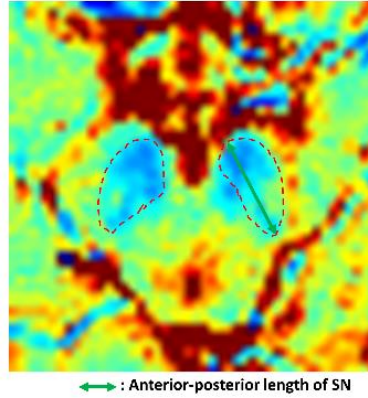


Figure 3.2.2 The manually drawn boundary (red dotted line) around the short T_2^* region with anterior-posterior length of the SN; SN = substantia nigra.

Image processing and statistical analysis of in vivo MRI

Consistent with the procedure for postmortem MRI to delineate neuromelanin distribution patterns, after performing 2D rigid transformation of rotation and translation for the co-registration using MATLAB, the T_2^* map was divided by the T_2 map, then the voxels of the T_2^* map were empirically thresholded using a cutoff level of 30 ms, while those of the T_2 map were correspondingly thresholded at 60 ms (2×30 ms), respectively, to generate binary images for all *in vivo* subjects. The binary images were overlapped with a manually segmented ROI around the entire SN (Figure 3.2.2). The binary mask from the T_2 map was subtracted from that of the T_2^* map. In this way, the voxels which satisfied the condition of $T_2 - T_2^* > T_{2^*,\text{threshold}}$ were selected as the areas of significant T_2 and T_2^* mismatch, empirically determined by only the $T_{2^*,\text{threshold}}$ values (30 ms) for all sixteen *in vivo* subjects. Additionally, for the Parkinson's disease patients, the anterior and posterior portions were divided by transecting each side from the anterior median fissure identified by neuromelanin-sensitive MRI [67] to exclude the ventromedial regions of iron deposition. Finally, the quantitative analyses were performed, and the results were compared between both normal controls and Parkinson's disease patients. The whole length of the mismatch line, which measures the diagonal line-length of whole T_2 and T_2^* binary mismatch mask, was analyzed for all subjects. Also, the dorsal border length of the mismatch line, which measures the corresponding line-length only within the posterior portion, was analyzed for Parkinson's disease patients.

The intensity of the hyperintense area of neuromelanin-sensitive MRI was normalized by the mean value of the background signals. Mean and standard error were estimated for the number of voxels within the hyperintense area and the normalized intensity sum within the hyperintense area of neuromelanin-sensitive MRI.

Considering apparent bilateral asymmetry in [^{18}F] FP-CIT PET uptake, a visual assessment of the [^{18}F] FP-CIT PET images was performed by an experienced neurologist (J.H. Lee). According to the degree of signal reduction in the putamen and caudate nucleus, each side of the brain was categorized as G1 (mild reduction, limited to the posterior putamen) or G2 (marked reduction, extending to the anterior putamen) for all eight Parkinson's disease patients, generating 16 datasets.

Statistical comparisons were made between groups by one-tailed, unpaired Mann-Whitney U-tests. p values < 0.05 were deemed statistically significant. Normal controls (sixteen bilateral SNs from eight subjects) and Parkinson's disease patients (sixteen bilateral SNs from eight patients, including seven SNs classified as G1 and nine SNs classified as G2) were compared based on the following parameters: (1) the whole length of the mismatch line from determined by the $T_2^*-T_2$ mask; (2) the dorsal border length of the mismatch line within the posterior portion based on the $T_2^*-T_2$ mask; (3) the number of voxels within the hyperintense area of the SN assessed by neuromelanin-sensitive MRI; and (4) the normalized intensity sums of the hyperintense areas within the SN determined from neuromelanin-sensitive MRI.

Two analyses were performed to compare the size of the SN, which was segmented based on the T_2^* map, between normal controls and Parkinson's disease patients. The anterior-posterior length of the SN (as shown by green line in Figure 3.2.2), which measures the line-length of the major axis of the oval SN mask, and the volume of the SN mask in two selected levels were quantitatively analyzed in both groups. These measurements to assess the size of the SN were also compared by one-tailed, unpaired Mann-Whitney U-tests, with p values < 0.05 deemed statistically significant.

3.2.3 Results

Neuromelanin-pigmented neurons were abundantly localized in the dorsal area of the SN

In the 3D reconstructed midbrain structure (Figure 3.2.3A and Figure 3.2.3B), which covers most of the SN from rostral to caudal levels (7.5mm thick), a wide distribution of stained ferric iron molecules was observed, represented as red dots. Most red dots were concentrated in the SNr based on Perls' Prussian blue staining (Figure 3.2.3C and Figure 3.2.3E). Neuromelanin pigments existed along the SNc, indicated by green dots, and the distribution of neuromelanin showed high colocalization with the positively-stained region in tyrosine hydroxylase immunohistochemistry, a marker of dopaminergic

neurons (Figure 3.2.3D and Figure 3.2.3F). The neuromelanin-pigmented neurons were distributed linearly in the caudal and intermediate levels of the SN [9]; their localization was abundant in the dorsal area of the SN, especially in the intermediate level.

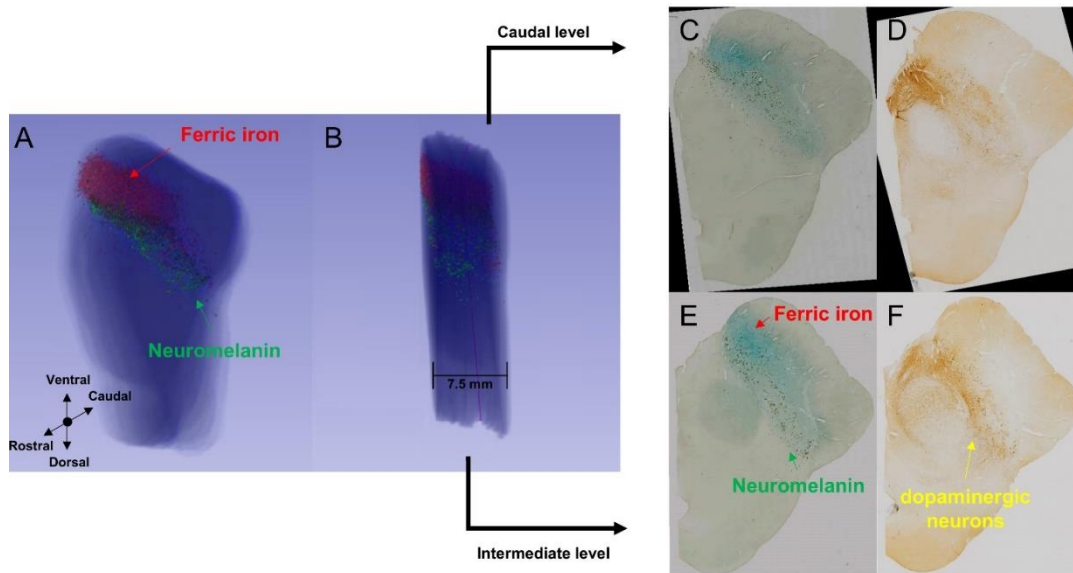


Figure 3.2.3 3D reconstructed midbrain tissue showing deposited ferric iron and neuromelanin pigments. (A): 3D reconstructed midbrain tissue captured from the first angle; (B): 3D reconstructed midbrain tissue captured from the second angle; (C): Perls' Prussian blue staining at the caudal level; (D): Tyrosine hydroxylase immunohistochemistry at the caudal level; (E): Perls' Prussian blue staining at the intermediate level; (F): Tyrosine hydroxylase immunohistochemistry at the intermediate level. Stained tissue sections were 50 μm thick.

MRI signal properties of neuromelanin, ferric iron, and myelinated fibers

The postmortem multimodal MR images (Figure 3.2.4I-A, Figure 3.2.4II-A, and Figure 3.2.4III-A) demonstrated that a separation of the gray matter and white matter was attained in the T_1 -weighted image with an MT preparation pulse, which has been previously validated through direct comparison with Luxol fast blue staining [57]. Shortened T_2^* (Figure 3.2.4I-B, Figure 3.2.4II-B, and Figure 3.2.4III-B) and T_2 values (Figure 3.2.4I-C, Figure 3.2.4II-C, and Figure 3.2.4III-C) in the SN of the three tissue specimens were observed, resulting from the presence of deposited iron, neuromelanin, and myelinated fibers. In the brain from the two normal subjects, the QSM, indicating paramagnetic components (positive susceptibilities) within the SN, was determined (Figure 3.2.4I-D and Figure 3.2.4II-D). Although both samples were obtained from normal subjects, fewer paramagnetic regions were observed in the susceptibility map of the sample from the 75-year-old female compared to the 86-year-old female, likely due to the age-related accumulation of paramagnetic iron compounds within the SN, which has

been shown to occur in normal subjects [1, 68]. In the case of depigmented SN sample obtained from the diseased brain, paramagnetic lines were observed across the medial SN and at the boundary between the SN and crus cerebri based on the QSM (Figure 3.2.4III-D). In this sample, there was co-localization between the paramagnetic lines and hypointense myelinated fibers in the T_1 -weighted image with MT effects, reflecting the iron deposition known to cause loss of neurons and myelinated fibers within the brain (Figure 3.2.4III-A).

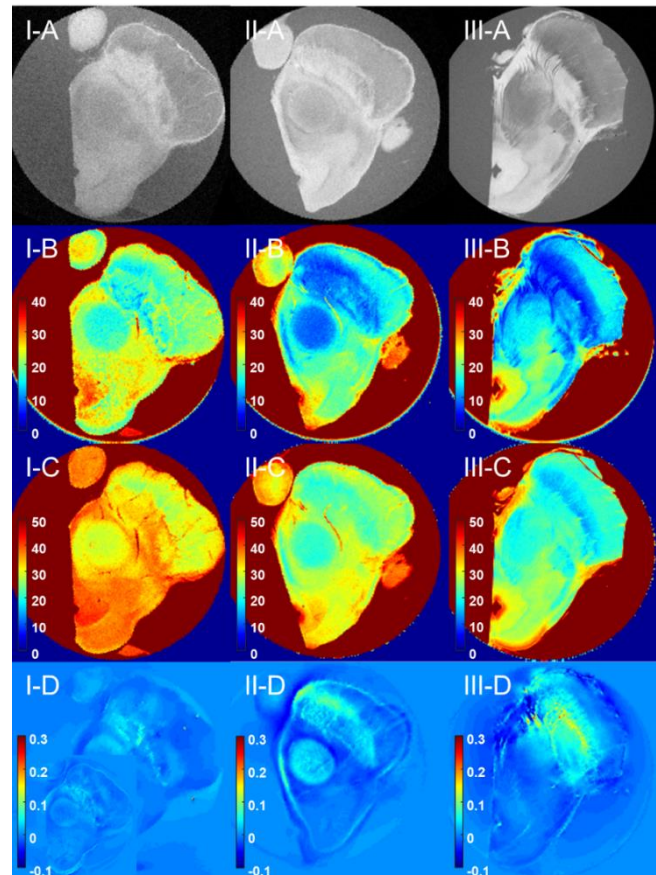


Figure 3.2.4 Postmortem multimodal MRI of the three subjects. (I: 75-year-old normal female; II: 86-year-old normal female; III: 51-year-old male patient with SN depigmentation). (A): T_1 -weighted image with MT effects; (B): T_2^* map (ms); (C): T_2 map (ms); (D): The susceptibility map from QSM (I-D: QSM-MEDI with inset showing QSM-COSMOS) (ppm). SN = substantia nigra; QSM = quantitative susceptibility mapping; MT = magnetization transfer; MEDI = morphology enabled dipole inversion; COSMOS = calculation of susceptibility through multiple orientation sampling.

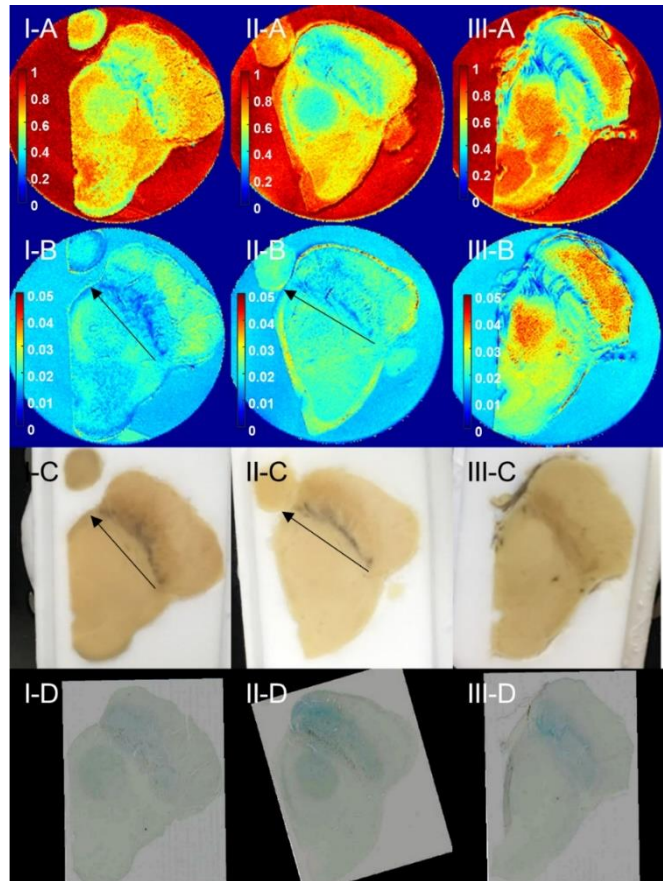


Figure 3.2.5 Postmortem multimodal MRI with direct histological validation. (I: 75-year-old normal female; II: 86-year-old normal female; III: 51-year-old male patient with SN depigmentation) (A): T_2^*/T_2 map; (B): T_2^*/T_2^2 map; (C): Image directly captured during cryosectioning; (D): Corresponding Perls' Prussian blue staining image. (Black arrows in B and C of subjects I and II indicate the neuromelanin distribution of the analogous dorsal linear pattern within the SN.) MRI = magnetic resonance imaging; SN = substantia nigra.

Delineation of neuromelanin-rich regions using combined T_2 and T_2^* maps

For the tissue isolated from the three brains (Figure 3.2.5), the overlap of the T_2 and T_2^* ratios and neuromelanin-rich regions was validated using co-registered images of dark neuromelanin pigments from the captured image of cryosectioned block-faces (Figure 3.2.5I-C, Figure 3.2.5II-C, and Figure 3.2.5III-C), and the results from the imaging of sections following Perls' Prussian blue staining (Figure 3.2.5I-D, Figure 3.2.5II-D, and Figure 3.2.5III-D). When the T_2^* map was combined voxel-wise with the T_2 map, the impact of deposited iron molecules on T_2^* was significantly reduced in the T_2^*/T_2 maps (Figure 3.2.5I-A, Figure 3.2.5II-A, and Figure 3.2.5III-A) and T_2^*/T_2^2 maps (Figure 3.2.5I-B, Figure 3.2.5II-B, and Figure 3.2.5III-B). In the direct comparison of the T_2^*/T_2^2 maps and the images from the histological experiments (Figure 3.2.5I-C, Figure 3.2.5II-C, and Figure 3.2.5III-C), the distribution of

dark neuromelanin pigments (Figure 3.2.5I-C, Figure 3.2.5II-C; black arrows) were highly colocalized with the regions of low value in the T_2^*/T_2^2 maps along the dorsal area of the SN (Figure 3.2.5I-B and Figure 3.2.5II-B) in the normal brains. However, the dark neuromelanin pigments within the SNc were not observed in the image captured from the depigmented SN from the diseased brain (Figure 3.2.5III-C). Negligible alterations were found in the corresponding region in the T_2^*/T_2^2 map. Instead, paramagnetic myelinated fibers were seen across the medial SN. The iron-positive signature was detected along the myelinated fibers in Perls' Prussian blue staining (Figure 3.2.5III-D).

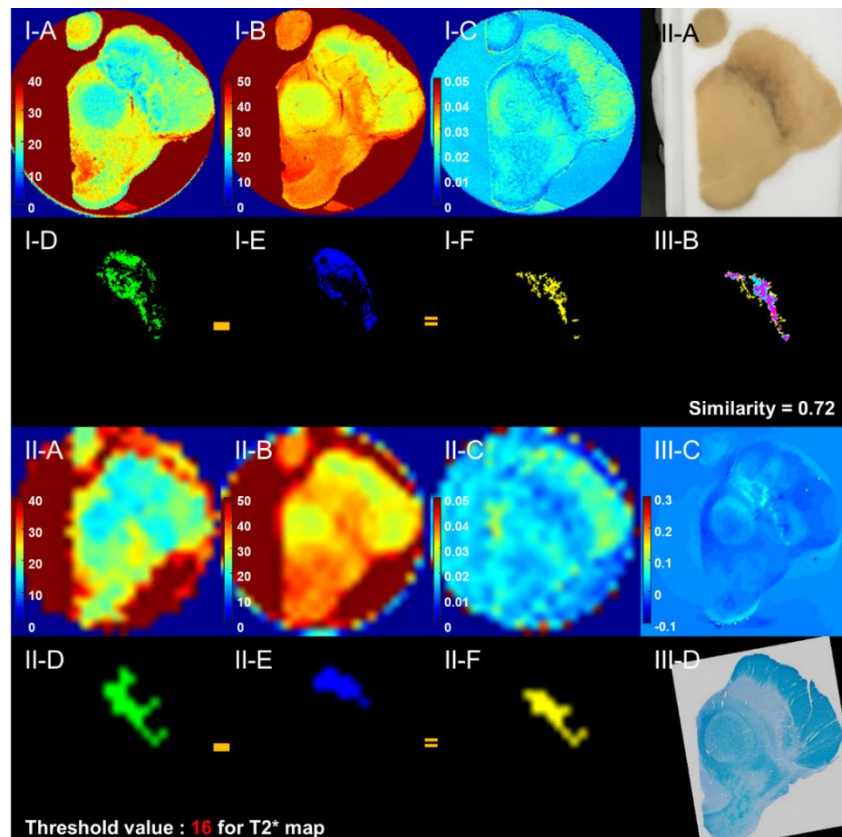


Figure 3.2.6 Neuromelanin segmentation by T_2^* and T_2 thresholding from the tissue sample obtained from a 75-year-old normal female. (I: high-resolution images (matrix size = 256 x 256); II: low-resolution images (matrix size = 32 x 32)) (A): T_2^* map (ms); (B): T_2 map (ms); (C): T_2^*/T_2^2 map; (D): T_2^* -thresholded mask; (E): T_2 -thresholded mask; (F): Subtraction of the T_2 -thresholded mask from the T_2^* -thresholded mask; (III-A): Image directly captured during cryosectioning; (III-B): The overlap of neuromelanin-expected area from the high-resolution T_2^*/T_2^2 map and binarized neuromelanin distribution segmented from the co-registered cryosectioned block-face; (III-C): The susceptibility map (ppm); (III-D): Corresponding Luxol fast blue staining image.

In the two brains from the normal subjects, comparison of the T_2^*/T_2^2 maps (Figure 3.2.6I-C and Figure

3.2.7I-C) generated from high-resolution images (matrix size = 256×256) revealed a trend consistent with what was observed based on the corresponding low-resolution (matrix size = 32×32) T_2^*/T_2^2 maps (Figure 3.2.6II-C, Figure 3.2.7II-C), though the neuromelanin-rich area was less precisely delineated in the low-resolution T_2^*/T_2^2 map compared to the higher resolution maps. Based on the simulations, the threshold values of 16 ms for the 75-year-old female, and 13 ms for the 86-year-old female on each T_2^* map (Figure 3.2.6I-A and Figure 3.2.7I-A) properly included the region of low T_2^* values around the SN, and the corresponding threshold values for the T_2 maps (Figure 3.2.6I-B and Figure 3.2.7I-B) were twice the threshold values of the T_2^* maps (32 ms and 26 ms for the two brains).

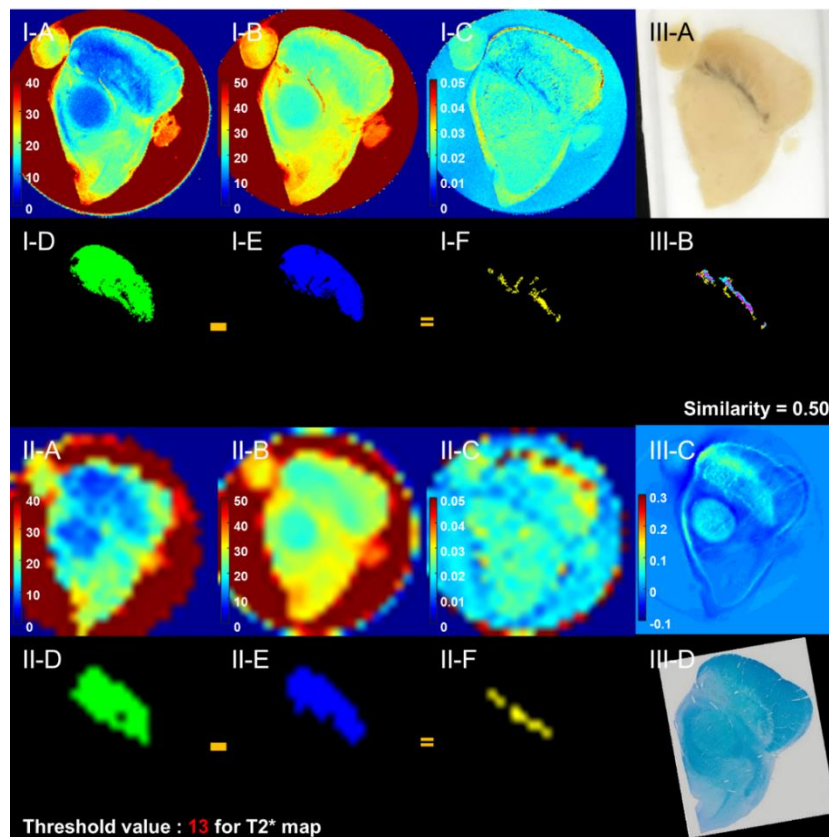


Figure 3.2.7 Neuromelanin segmentation by T_2^* and T_2 thresholding from the tissue sample obtained from an 86-year-old normal female. (I: high-resolution images (matrix size = 256×256); II: low-resolution images (matrix size = 32×32)) (A): T_2^* map (ms); (B): T_2 map (ms); (C): T_2^*/T_2^2 map; (D): T_2^* -thresholded mask; (E): T_2 -thresholded mask; (F): Subtraction of the T_2 -thresholded mask from the T_2^* -thresholded mask; (III-A): Image directly captured during cryosectioning; (III-B): The overlap of neuromelanin-expected area from the high-resolution T_2^*/T_2^2 map and binarized neuromelanin distribution segmented from the co-registered cryosectioned block-face; (III-C): The susceptibility map (ppm); (III-D): Corresponding Luxol fast blue staining image.

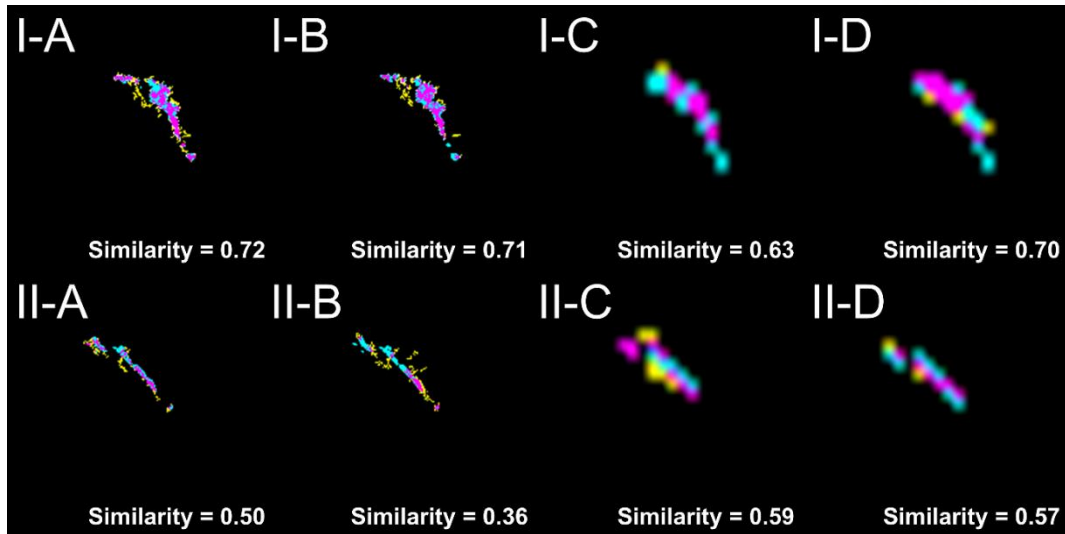


Figure 3.2.8 The overlap of the T_2^* and T_2 mismatch area of MRI and binarized neuromelanin distribution segmented from co-registered cryosectioned block-faces from normal controls. (I: 75-year-old normal female; II: 86-year-old normal female) (A): Overlap of the neuromelanin-expected area from the high-resolution T_2^*/T_2^2 map and histological staining; (B): Overlap of the neuromelanin-expected area from the high-resolution $T_2^*-T_2$ mask and histological staining; (C): Overlap of the neuromelanin-expected area from the low-resolution T_2^*/T_2^2 map and histological staining; (D): Overlap of the neuromelanin-expected area from the low-resolution $T_2^*-T_2$ mask and histological staining.

The binary region of T_2 and T_2^* mismatch (Figure 3.2.6I-F and Figure 3.2.7I-F) obtained by subtracting the T_2 -segmented mask (Figure 3.2.6I-E and Figure 3.2.7I-E) from the T_2^* -segmented mask (Figure 3.2.6I-D and Figure 3.2.7I-D) acquired from high-resolution MR relaxometry visualized considerable co-localization with the neuromelanin distribution observed from captured image of the cryosectioned block-faces (Figure 3.2.6III-A and Figure 3.2.7III-A). Subtraction of the low-resolution T_2 -segmented mask from the T_2^* -segmented mask generated blurry binary images (Figure 3.2.6II-F and Figure 3.2.7II-F), but colocalization was still observed with the neuromelanin distribution patterns. The overlap (magenta) of separated neuromelanin from the high-resolution T_2^*/T_2^2 map (yellow) and the binarized neuromelanin distribution (cyan) were used to determine Dice's similarity correlations for the 75-year-old female and the 86-year-old female; these values were 0.72 and 0.5, respectively (Figure 3.2.6III-B and Figure 3.2.7III-B). The similarities between the high- and low-resolution T_2 and T_2^* mismatches and the binarized neuromelanin distributions (cyan) were consistent for both subjects (Figure 3.2.8).

In the depigmented SN of the diseased brain, the linear paramagnetic signals across the SN clearly visible in the high-resolution T_2^*/T_2^2 map (Figure 3.2.9I-C) appeared as blurred spots in the low-resolution T_2^*/T_2^2 map (Figure 3.2.9II-C). The mismatch between the T_2^* -segmented mask (Figure 3.2.9I-D and Figure 3.2.9II-D) using the threshold value of 9 ms on the T_2^* map (Figure 3.2.9I-A and

Figure 3.2.9II-A) and the T_2 -segmented mask (Figure 3.2.9I-E and Figure 3.2.9II-E) using the threshold value of 18 ms on the T_2 map (Figure 3.2.9I-B and Figure 3.2.9II-B) revealed a gross delineation of myelinated fibers across the SN (Figure 3.2.9I-F and Figure 3.2.9II-F). However, due to the absence of dorsal neuromelanin pigments in the depigmented SN, Dice's similarity correlation resulted in a value of zero for this tissue sample (Figure 3.2.9III-B). It is also noted that the lateral T_2 and T_2^* mismatch area in both high-resolution and low-resolution $T_2^*-T_2$ masks co-localized with the myelin distribution (Figure 3.2.9III-D). Such area was not conspicuous in corresponding T_2^*/T_2^2 map. Thus, observed T_2 and T_2^* mismatch area in subtraction mask of the lateral area was also from myelinated fibers within the SN, and much shorter than the length of dorsal neuromelanin distribution in normal SN.

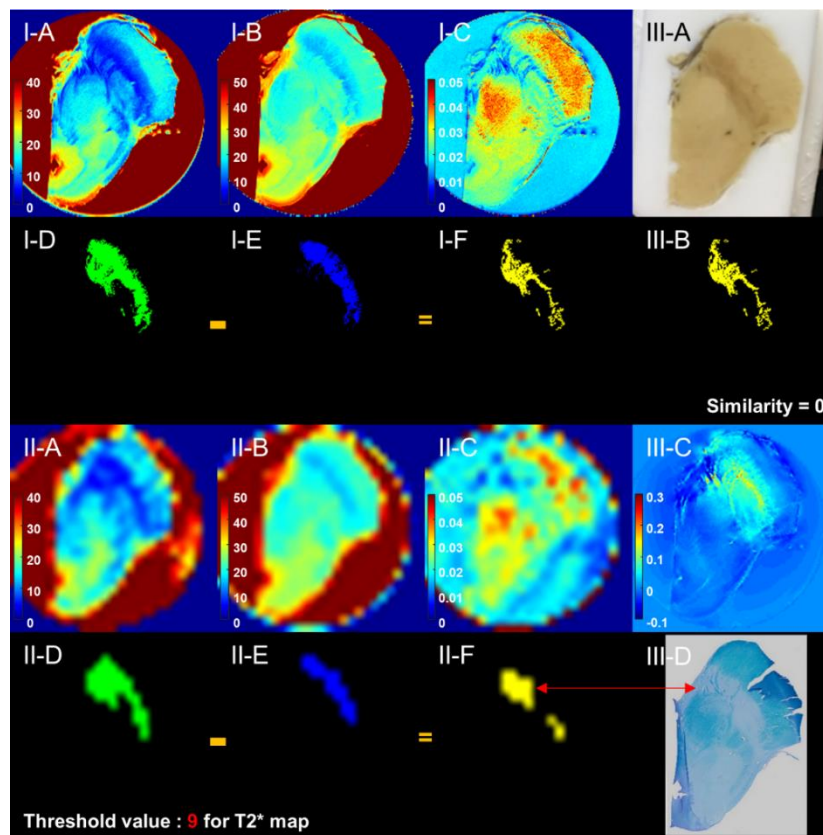


Figure 3.2.9 Neuromelanin segmentation by T_2^* and T_2 thresholding from the tissue sample obtained from a 51-year-old male patient with SN depigmentation (I: high-resolution images (matrix size = 256 x 256); II: low-resolution images (matrix size = 32 x 32)). (A): T_2^* map (ms); (B): T_2 map (ms); (C): T_2^*/T_2^2 map; (D): T_2^* -thresholded mask; (E): T_2 -thresholded mask; (F): Subtraction of the T_2 -thresholded mask from T_2^* -thresholded mask; (III-A): Image directly captured during cryosectioning; (III-B): The overlap of the neuromelanin-expected area from the high-resolution T_2^*/T_2^2 map and the binarized neuromelanin distribution segmented from the co-registered cryosectioned block-faces; (III-C): The susceptibility map (ppm); (III-D): Corresponding Luxol fast blue staining image.

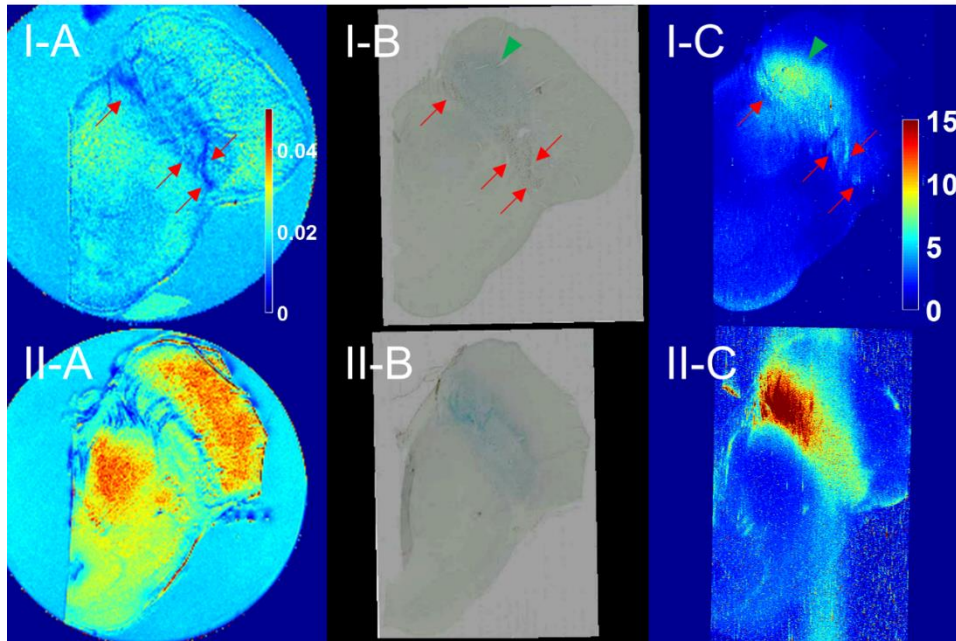


Figure 3.2.10 Iron chelation with neuromelanin pigments. I: 75-year-old normal female; II: 51-year-old male patient with SN depigmentation. (A): T_2^*/T_2^2 map; (B): Perls' Prussian blue staining; (C): LA-ICP-MS imaging of the intensity of $^{56}\text{Fe}/^{13}\text{C}$. Red arrows indicate the visible neuromelanin distribution in each image. Green arrowheads indicate the ferric iron distribution in each image. SN = substantia nigra; LA-ICP-MS = laser ablation inductively coupled plasma mass spectrometry.

Iron deposition mapping by LA-ICP-MS in the SN

For a normal brain and the diseased brain with a depigmented SN, the origin of the observed T_2 and T_2^* mismatch areas (Figure 3.2.10I-A and Figure 3.2.10II-A) was further validated by co-localizing the spatial distributions of iron clusters determined by Perls' Prussian blue staining to detect the iron bound only to iron metabolism molecules, such as hemosiderin (Figure 3.2.10I-B and Figure 3.2.10II-B) (Meguro et al., 2005; Ugarte et al., 2018; De Barros et al., 2019) and LA-ICP-MS imaging to observe all molecular forms of iron (Figure 3.2.10I-C and Figure 3.2.10II-C). The location of the T_2 and T_2^* mismatch areas within the SN of the normal brain (Figure 3.2.10I-A, indicated by the red arrows), was consistent with respect to both the distribution patterns of neuromelanin pigments determined from Perls' Prussian blue staining (Figure 3.2.10I-B) and elevated $^{56}\text{Fe}/^{13}\text{C}$ intensity from LA-ICP-MS imaging (Figure 3.2.10I-C). The ventromedial area of the elevated $^{56}\text{Fe}/^{13}\text{C}$ signals from LA-ICP-MS, indicated by a green arrow, was observed to co-localize with the area of stained ferric iron deposition determined from Perls' Prussian blue staining.

On the other hand, the diseased brain showed an overall elevation of iron deposition within the SN based on LA-ICP-MS (Figure 3.2.10II-C), which was corroborated with Perls' Prussian blue staining

(Figure 3.2.10II-B). The ventromedial T_2 and T_2^* mismatch areas of the diseased brain (Figure 3.2.10II-A), especially, were co-localized with both ferric iron deposition along the myelinated fibers observed by Perls' Prussian blue staining and the elevation of $^{56}\text{Fe}/^{13}\text{C}$ intensity along the myelinated fibers seen in LA-ICP-MS imaging (Figure 3.2.10II-C).

Feasibility of employing T_2 and T_2^* mismatch clinically

All *in vivo* MR images for two selected levels of eight normal controls and eight Parkinson's disease patients are shown in Figure 3.2.11 and Figure 3.2.12, respectively. Representative MR images of *in vivo* experiments on both a normal subject (Figure 3.2.13I-a,b,c,d) and a Parkinson's disease patient (Figure 3.2.13II -a, b, c, d, e, f) are shown, along with the corresponding normal (Figure 3.2.13I-A,B,C,D) and diseased (Figure 3.2.13II - A, B, C, D, E, F) postmortem examples. The areas of short T_2^* values were observed to be disproportionately wider compared to areas of short T_2 values for both postmortem and *in vivo* SNs. In the T_2^* maps of normal SNs (Figure 3.2.13I-B and Figure 3.2.13I-b), the dorsal linear line was included in the manually segmented whole SN region. However, the area of low T_2 values was mainly localized in the ventromedial area of the normal SNs (Figure 3.2.13I-C and Figure 3.2.13I-c). Correspondingly, the mismatch regions (Figure 3.2.13I-D and Figure 3.2.13I-d) determined by subtracting the T_2 -segmented mask from the T_2^* -segmented mask were consistently seen as a linear pattern in the dorsal area of the normal SNs. Then, the whole dorsal mismatch lines which appeared along the dorsal area of the SN were marked by blue arrows for normal (Figure 3.2.13I-D and Figure 3.2.13I-d) and diseased brains (Figure 3.2.13II-D and Figure 3.2.13II-d). In the cases of diseased brains, the linear T_2 and T_2^* mismatch regions obtained by subtracting the T_2 - and T_2^* -thresholded masks were mostly obscured. Furthermore, the region of T_2 and T_2^* mismatch expanded to a greater degree, ventrally. Then, the dorsal border length of the mismatch line within the posterior portion could be obtained by excluding the ventral T_2 and T_2^* mismatch in diseased SN, as representatively shown by green arrows in Figure 3.2.13II-E and Figure 3.2.13II-e for diseased SNs. Particularly, in this *in vivo* case of Parkinson's disease patient, both whole length of the mismatch line and dorsal border length of the mismatch line appeared to be asymmetric; their losses were more pronounced on the side ipsilateral to the hemisphere exhibiting lower [^{18}F] FP-CIT uptake (Figure 3.2.13II-f).

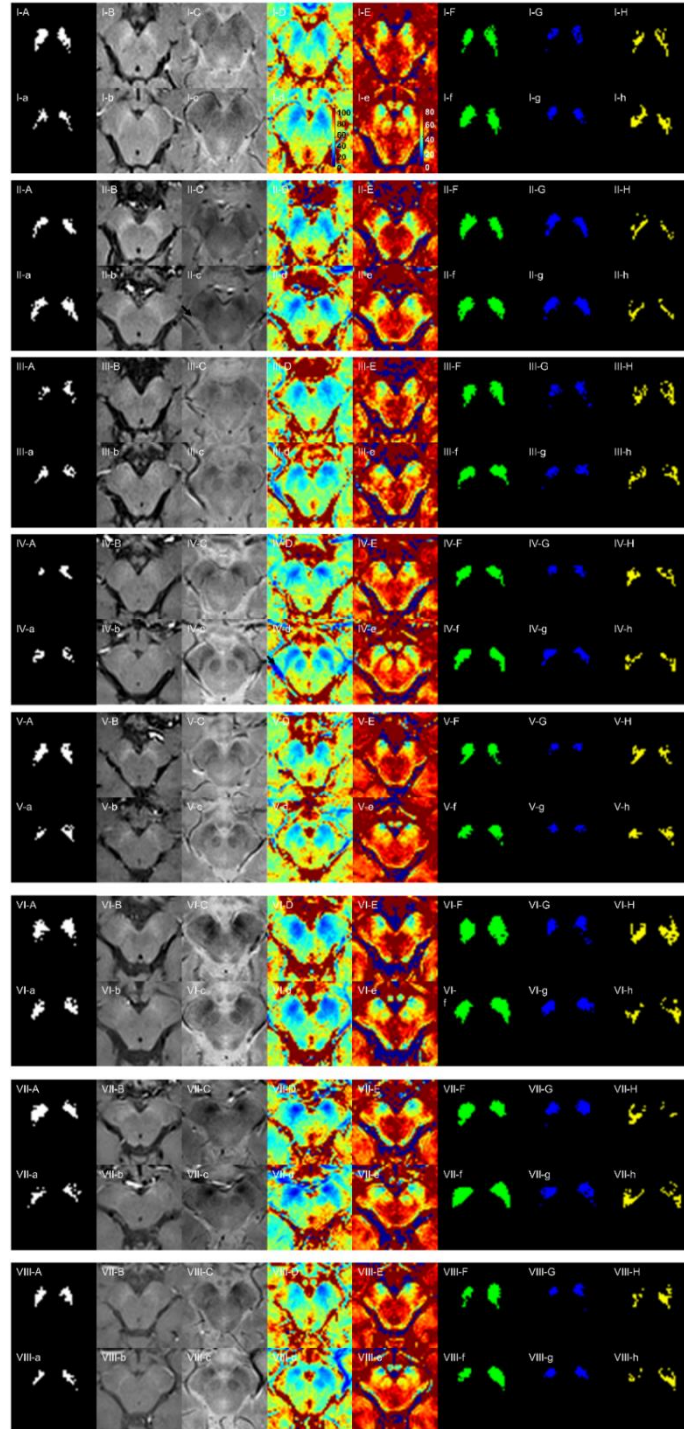


Figure 3.2.11 *In vivo* multimodal MRI for two intermediate levels in normal subjects. Upper- and lower-case letters show MRI for two levels of each subject. (A, a): Segmented hyperintense area from neuromelanin-sensitive MRI; (B, b): Neuromelanin-sensitive MRI; (C, c): SWI; (D, d): T_2^* map (ms); (E, e): T_2 map (ms); (F, f): T_2^* -thresholded mask; (G, g): T_2 -thresholded mask; (H, h): Subtraction of the T_2^* -thresholded mask from the T_2 -thresholded mask. MRI = magnetic resonance imaging, SWI = susceptibility-weighted imaging, SN = substantia nigra.

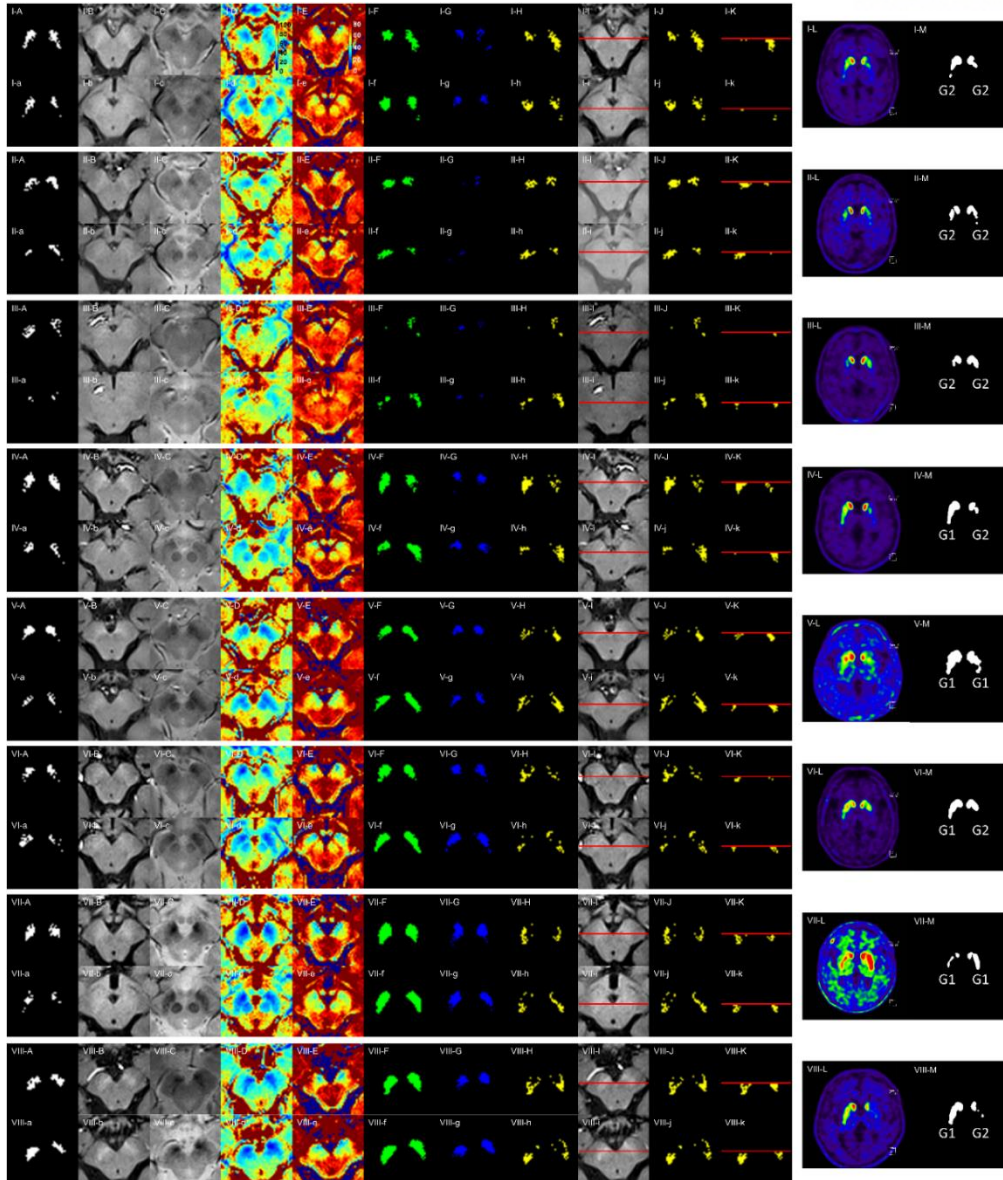


Figure 3.2.12 *In vivo* multimodal MRI for two intermediate levels in Parkinson's disease patients. Upper- and lower-case letters show MRI for two levels of each subject. (A, a): Segmented hyperintense area from neuromelanin-sensitive MRI; (B, b): Neuromelanin-sensitive MRI; (C, c): SWI; (D, d): T_2^* map (ms); (E, e): T_2 map (ms); (F, f): T_2^* -thresholded mask; (G, g): T_2 -thresholded mask; (H, h): Subtraction of the T_2^* -thresholded mask from the T_2 -thresholded mask; (I, i): Subsection (red line) of the anterior and posterior portions from neuromelanin-sensitive MRI; (J, j): Subsection (red line) of the mismatch line from the T_2^* - T_2 mask; (K, k): Remaining mismatch line in the posterior portion of the SN; (L): Corresponding $[^{18}\text{F}]$ FP-CIT PET image; (M): The segmented area based on the $[^{18}\text{F}]$ FP-CIT PET image. MRI = magnetic resonance imaging, SWI = susceptibility-weighted imaging, SN = substantia nigra; $[^{18}\text{F}]$ FP-CIT PET = ^{18}F -N-(3-fluoropropyl)-2 β -carbomethoxy-3 β -(4-iodophenyl) nortropane positron emission tomography.

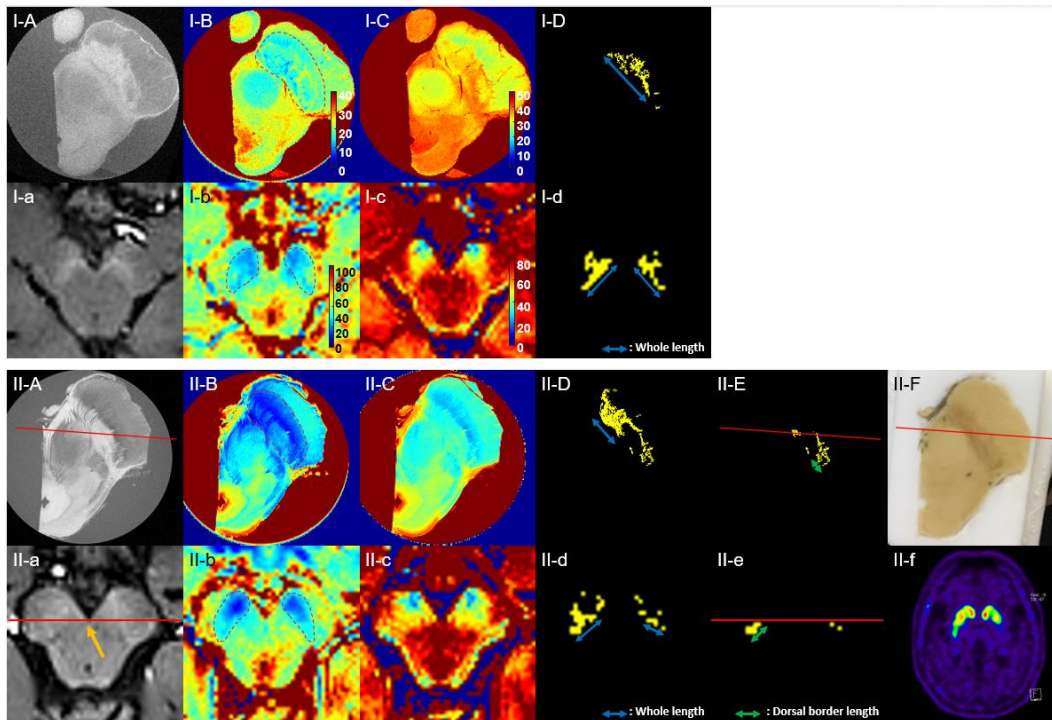


Figure 3.2.13 Schematic flow diagram for postmortem and *in vivo* MRI analysis. I-A to I-D: Normal postmortem SN; I-a to I-d: Normal *in vivo* SN; II-A to II-F: Diseased postmortem SN; II-a to II-f: Diseased *in vivo* SN. (A, a): Neuromelanin-sensitive MRI and transections (red line) of the anterior and posterior portions from the anterior median fissure (orange arrow) for diseased brains; (B, b): T_2^* map (ms) and manually drawn boundary (red dotted line) around the short T_2^* region; (C, c): T_2 map (ms); (D, d): The whole length of the mismatch line from the T_2^* - T_2 mask; (II-E, II-e): The dorsal border length of the mismatch line from the T_2^* - T_2 mask; (II-F): Image directly captured during cryosectoining; (II-f): Corresponding [^{18}F] FP-CIT PET image for a Parkinson's disease patient. MRI = magnetic resonance imaging; SWI = susceptibility-weighted imaging; [^{18}F] FP-CIT PET = ^{18}F -N-(3-fluoropropyl)-2 β -carbomethoxy-3 β -(4-iodophenyl) nortropane positron emission tomography.

The observed dorsal linear mismatches (Figure 3.2.13I-D and Figure 3.2.13I-d) were generally maintained except a few sides (one ~ two among four sides in subjects of V, VII, and VIII) as shown in Figure 3.2.11H and Figure 3.2.11h for normal subjects. However, such mismatches were shortened for most of Parkinson's disease patients (Figure 3.2.12H and Figure 3.2.12h). The dorsolateral nigral hyperintensity based on SWI was visually detectable in all normal controls (Figure 3.2.11C and Figure 3.2.11c). The dorsal hypointense boundary observed in the SWI of normal controls was considerably colocalized with the linearly short T_2^* region. While SWI of Parkinson's disease patients mostly showed an apparent loss of dorsolateral nigral hyperintensity, but weak hyperintensity still remained in subjects of II and VIII (Figure 3.2.12II-C and Figure 3.2.12VIII-C). In *in vivo* neuromelanin-sensitive MRI

(Figure 3.2.13I-a and Figure 3.2.13II-a), the signal contrast between the hyperintense SNc and surrounding areas appeared more apparent in the representative case of normal control compared to the representative case of Parkinson's disease patient. The observed dorsal linear pattern was not clearly resolved in other methods of calculating the ratios (T_2^*/T_2 , T_2^*/T_2^2) in normal subjects and Parkinson's disease patients likely due to the comparably lower resolution of clinical 3T MR imaging (Figure 3.2.14); this is consistent with postmortem low-resolution imaging.

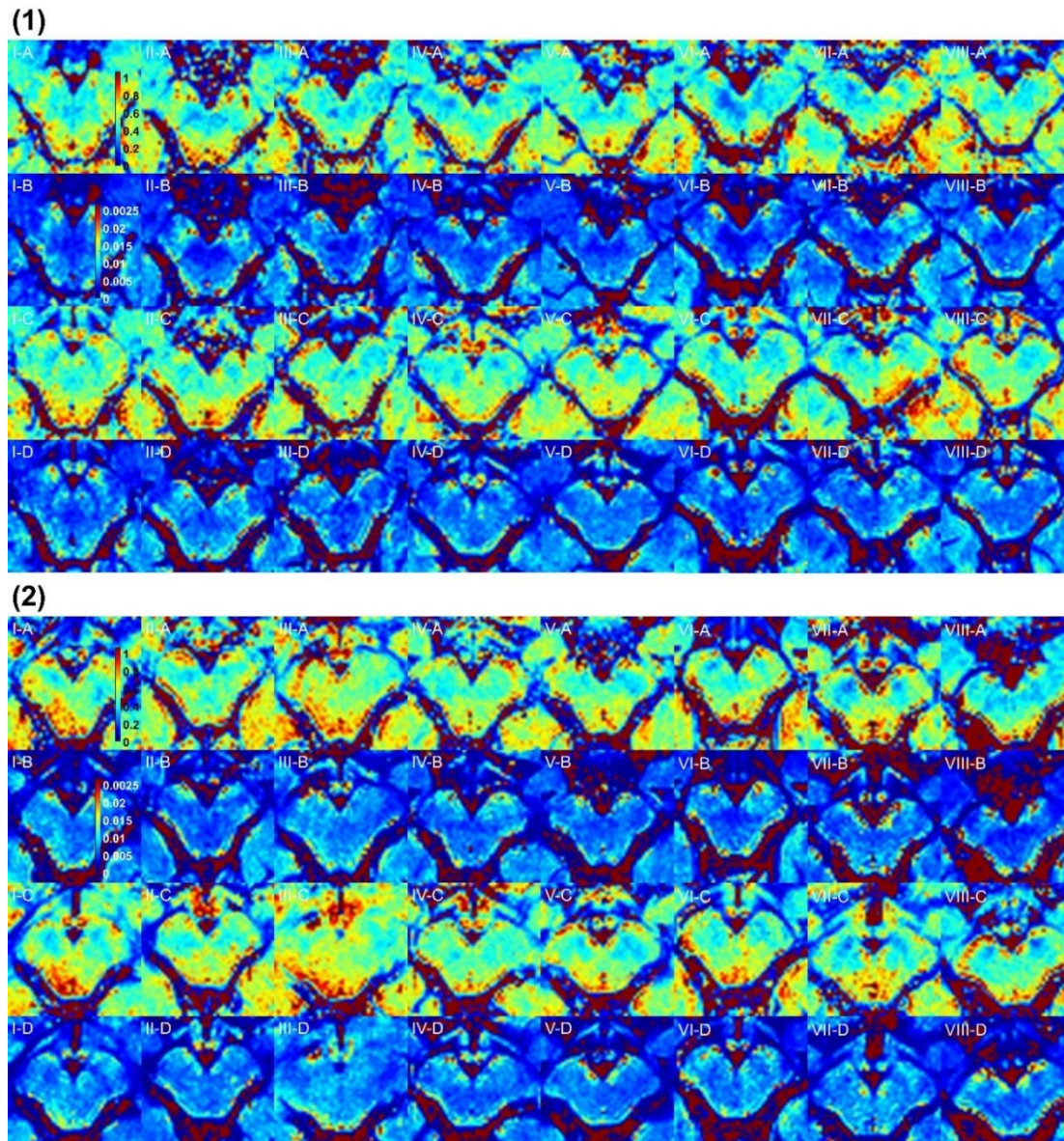


Figure 3.2.14 *In vivo* T_2 and T_2^* ratios for two levels of normal subjects and Parkinson's disease patients. (1): normal subjects; (2): Parkinson's disease patients. (I-VIII: subjects 1-8, displayed in the same order as in Figure 3.2.11 and Figure 3.2.12). (A): T_2^*/T_2 map of one level; (B): T_2^*/T_2^2 map of one level; (C): T_2^*/T_2 map of another level; (D): T_2^*/T_2^2 map of another level.

Table 3.2.1 Quantitative values from T_2 and T_2^* mismatch and neuromelanin-sensitive MRI technique.

Group	Whole length of mismatch line (mm)	Dorsal border length of mismatch line (mm)	Hyperintense area in neuromelanin-sensitive MRI (voxels)	Intensity sum of hyperintense area from neuromelanin-sensitive MRI (a.u.)	Anterior-posterior length of the SN (mm)	Volume of the SN mask (mm ³)
Normal	9.0±0.5	.	30.2±2.0	34.5±2.4	11.9±0.2	132.0±4.9
Parkinson's disease	5.5±0.4	.	27.2±1.9	29.8±2.1	12.0±0.3	124.8±4.0
G1 grading from PET	6.4±0.7	4.2±0.6	30.6±2.3	33.6±2.5	.	.
G2 grading from PET	4.8±0.5	2.6±0.5	24.5±2.7	26.9±3.0	.	.

The values (Mean ± SE) are the whole length of the mismatch line, the dorsal border length of the mismatch line, the hyperintense area from neuromelanin-sensitive MRI, intensity sum of the hyperintense area from neuromelanin-sensitive MRI, the anterior-posterior length of the SN, and the volume of the SN mask in normal controls, Parkinson's disease patients, and those categorized as G1 or G2 based on PET scans. MRI = magnetic resonance imaging, SN = substantia nigra, PET = positron emission tomography.

For the statistical analysis, the quantitatively measured values (means ± SE) for each group are summarized in Table 3.2.1. The whole length of the T_2 and T_2^* mismatch line was significantly shorter in Parkinson's disease patients (5.5 ± 0.4 mm) compared to the normal controls (9.0 ± 0.5 mm) with p value < 0.005 (Figure 3.2.15A). However, two measurements obtained from neuromelanin-sensitive MRI were not significantly different between normal controls and Parkinson's disease patients (Figure 3.2.15B and Figure 3.2.15C). Specifically, the number of voxels within the hyperintense area of the SN was 30.2 ± 2.0 in normal controls and 27.2 ± 1.9 in Parkinson's disease patients with non-significant p value of 0.2219. The normalized intensity sum of the hyperintense area within the SN was 34.5 ± 2.4 a.u. in normal controls and 29.8 ± 2.1 a.u. in Parkinson's disease patients with non-significant p value of 0.1241.

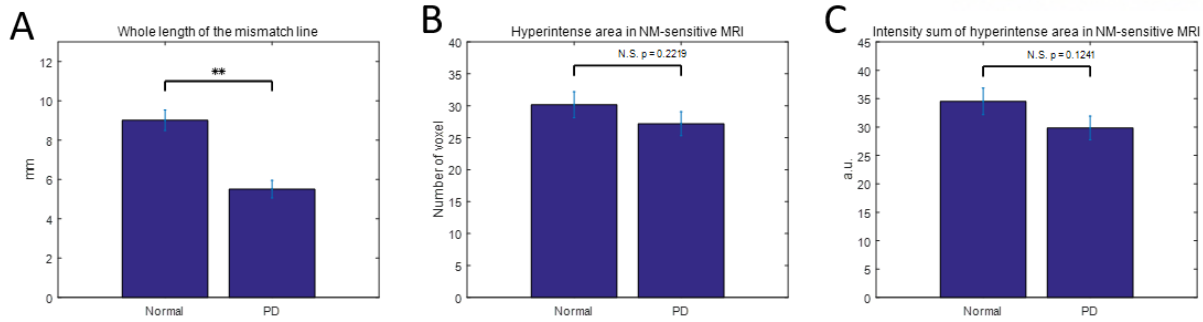


Figure 3.2.15 *In vivo* MRI of normal controls and Parkinson's disease patients. (A): Bar graph of the whole length mismatch line determined from the T_2^* - T_2 mask in normal controls and Parkinson's disease patients; (B): Bar graph of the hyperintense region derived from neuromelanin-sensitive MRI in normal controls and Parkinson's disease patients; (C): Bar graph of the intensity sums of the hyperintense region from neuromelanin-sensitive MRI in normal controls and Parkinson's disease patients. Normal controls and Parkinson's disease patients was compared by one-tailed unpaired Mann-Whitney U-test; **: p value < 0.005 , N.S.: non-significant p value > 0.05 .

Data from the *in vivo* MRI measurements are compared for the three groups (normal, G1, and G2) based on [^{18}F] FP-CIT PET scan results in Figure 3.2.16. The measurements on the whole length of the linear T_2 and T_2^* mismatch was both significantly different between normal and G1 and between normal and G2 (Figure 3.2.16A). But such difference was insignificant between G1 and G2, where both are groups from Parkinson's disease. Whereas, the dorsal border length of the mismatch line within the posterior portion was 4.2 ± 0.6 mm in G1 and 2.6 ± 0.5 mm in G2, with a considerable difference between the two groups with p value < 0.05 (Figure 3.2.16B). On the other hands, differences in the measurements based on neuromelanin-sensitive MRI were not consistent among the three groups (Figure 3.2.16C and Figure 3.2.16D).

3.2.4 Discussions and Conclusions

Through direct correlational analyses of postmortem histology, we have previously shown that the neuromelanin-iron complex has a significant effect in reducing T_2^* , but not T_2 values [22, 57]. In this study, we further expanded the utility of such ideas by (1) validating the hypothesis that the T_2 and T_2^* mismatches are useful for detecting differences in dorsal neuromelanin populations between normal and depigmented SNs. Direct comparison of the T_2 and T_2^* mismatch area obtained from MRI and assessment of neuromelanin distribution observed from captured image of the cryo-section block-faces in postmortem tissues showed consistent similarities (higher than those from conventional neuromelanin-sensitive MRI) for the two normal SN samples, but not for the depigmented SN sample.

(2) Also, the elevated iron signals identified by LA-ICP-MS were co-localized with neuromelanin distribution detected from histology, further confirming iron chelation on neuromelanin in normal SN. (3) Finally, *in vivo* assessments using 3T MRI demonstrated the clinical feasibility of utilizing the length of the T_2 and T_2^* mismatch to distinguish between the dorsal region of normal and diseased SNs. The dorsal linear mismatch that we observed in the brains of normal subjects was consistent with the findings from postmortem MR relaxometry, despite the potential angular and the resolution discrepancy in imaging acquisition between postmortem and *in vivo* MRI as shown in Figure 3.2.13. The degradation of this dorsal linear T_2 and T_2^* mismatch was observed in both postmortem and *in vivo* studies of diseased SNs.

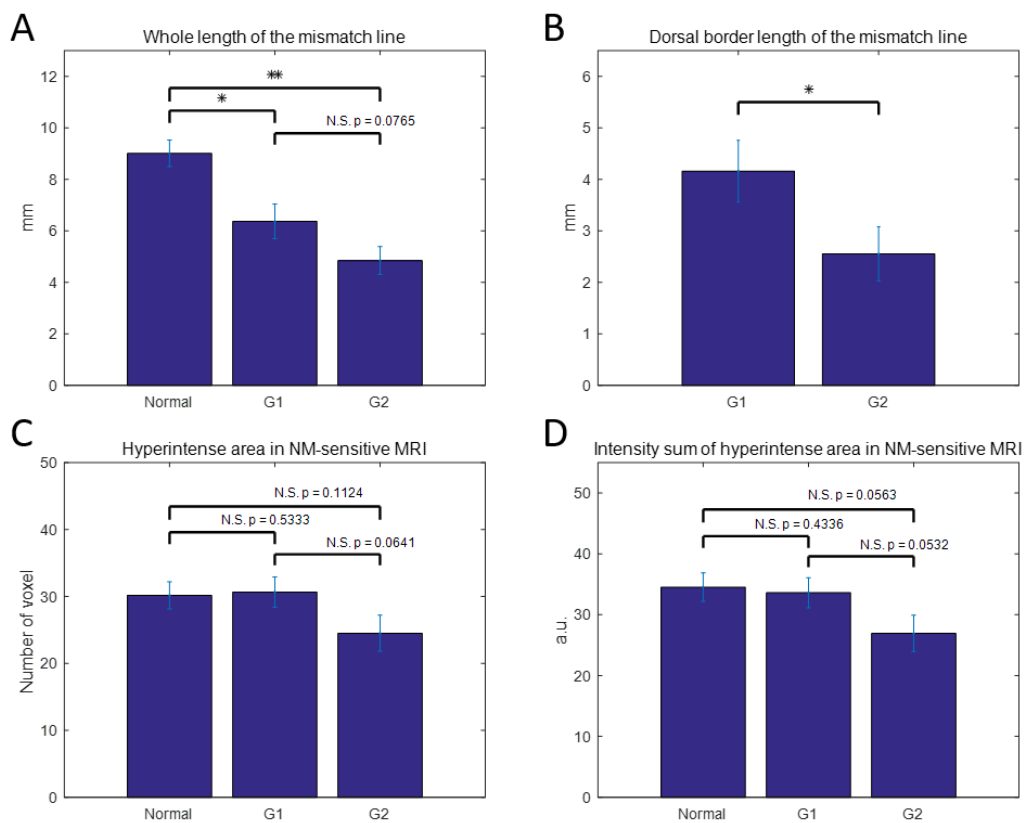


Figure 3.2.16 *In vivo* MRI of three groups categorized from [^{18}F] FP-CIT PET. (A): Bar graph of the whole length of the mismatch line based on the T_2^* - T_2 mask in normal, G1, and G2 categories; (B): Bar graph of the dorsal border length of the mismatch line based on the T_2^* - T_2 mask in G1, and G2 categories; (C): Bar graph of the hyperintense region assessed by neuromelanin-sensitive MRI in normal, G1, and G2 categories; (D): Bar graph of the intensity sums of the hyperintense region from neuromelanin-sensitive MRI in normal, G1, and G2 categories. Normal controls and Parkinson's disease patients were compared by one-tailed unpaired Mann-Whitney U-test; *: p value < 0.05, **: p value < 0.005, N.S.: non-significant p value > 0.05.

Our unique methodology allowed us to develop and optimize a novel preliminary *in vivo* MRI biomarker through *ex vivo* experimentation. To detect the neuromelanin-rich SNc at clinically available resolution, we verified the region of T_2 and T_2^* mismatch using low-resolution postmortem relaxometry. Furthermore, Monte Carlo simulations were performed to validate the rationale of thresholding T_2 and T_2^* values. Despite the challenges involved in interpreting the low-resolution images obtained from *in vivo* MR relaxometry, the mismatch between the T_2 - and T_2^* -thresholded masks highlighted the differences in the dorsal area of the SN between the normal subjects and the Parkinson's disease patients. Through objective analysis, we observed that although the anterior-posterior length of the SN and the area of the SN mask were comparable between normal controls and diseased brains (Table 3.2.1 and Figure 3.2.17), the whole length of the mismatch line from the T_2^* - T_2 mask was significantly shortened in the diseased brain compared to the normal controls.

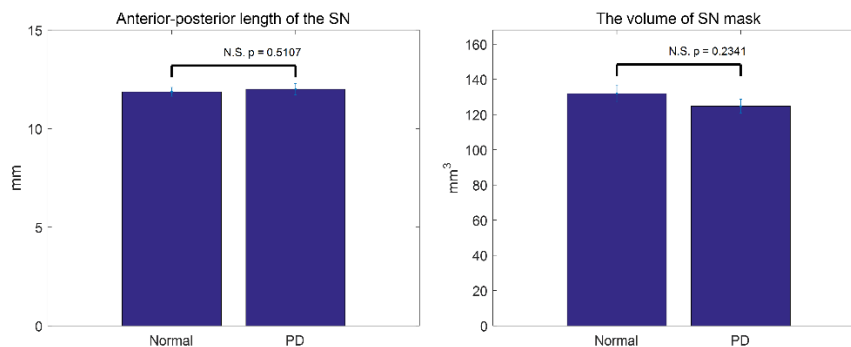


Figure 3.2.17 The quantitative measurement of SN size in normal controls and Parkinson's disease patients. Anterior-posterior lengths of the SN in normal controls and Parkinson's disease patients and the volume of the SN mask in normal controls and Parkinson's disease patients. Normal controls and Parkinson's disease patients was compared by one-tailed unpaired Mann-Whitney U-test; N.S.: not significant $p > 0.05$. MRI = magnetic resonance imaging; SN = substantia nigra.

The linear T_2 and T_2^* mismatch region along the dorsal area of the SN exhibited short T_2^* values and appeared as a prominent hypointense signal in SWI. Neuromelanin-enriched subdivisions are comprised of the pars medialis, pars lateralis, and dorsal tier, aligned along the dorsal area of the SN [9, 69]. In our study, using 3D histological reconstruction, abundant neuromelanin-pigmented neurons were observed to be linearly distributed in the dorsal area of the SN. Some authors have suggested that the medial lemniscus or intrinsic microvessels contribute to the linear hypointensity in the dorsal area [50, 70]. Further studies using QSM will confirm the identification of paramagnetic neuromelanin in the hypointense dorsal area of the SN against the medial lemniscus, which is the component of white matter with the diamagnetic property. Our postmortem QSM results from the brains of the two normal subjects

showed dorsal linear neuromelanin distribution as paramagnetic molecules. The microvessels running along the caudolateral circumference of the red nucleus cannot account for the hypointensity observed throughout the whole dorsal area of the SN. Therefore, neuromelanin-related contrast could contribute to the hypointense boundary surrounding the dorsolateral nigral hyperintensity or the swallow tail sign, which seemed to correspond to nigrosome 1 in SWI.

Parkinson's disease patients typically had shorter mismatch lines than the normal subjects. The linearity along the dorsal area tended to be obscured, which was corroborated with a decreased uptake of [¹⁸F] FP-CIT in PET scans, which identifies dopamine transporters. The shorter length of the mismatch line exhibited more dramatic reductions in [¹⁸F] FP-CIT signals. However, the shortened dorsal linear mismatch region may not be fully explained by loss of neuromelanin alone. The distribution of reactive iron molecules sequestered in the form of ferritin or hemosiderin within the SN, which accumulate in neurons, glia, and particularly in oligodendrocytes, extends into the dorsal area of the SNc [60]. These iron clusters could also cause the shortening of T_2 values in the corresponding region and they may contribute to shortening dorsal T_2 and T_2^* mismatch lines as well. However, it should be carefully considered that although neuromelanin-iron complexes are primarily localized in dopaminergic neurons, extra-neuronal neuromelanin-iron complexes released by degenerating neurons are associated with the progression of Parkinson's disease [71].

In some *in vivo* cases, the T_2 and T_2^* mismatch region has also been identified in the ventral part of the SN. Excessive accumulation of certain types of iron molecules can form iron clusters of a larger size to alter T_2 and T_2^* values disproportionately, further generating T_2 and T_2^* mismatch; this was validated by the Monte Carlo simulation to investigate the impact of cluster size of spherical paramagnetic perturbers on MR T_2 and T_2^* values. Within the *ex vivo* depigmented SN, the myelinated fibers colocalized with ferric iron and appeared to exhibit paramagnetic properties through QSM, although myelin has conventionally been considered a diamagnetic molecule [72]. The myelinated, large-diameter fibers running through the SN may additionally contribute to the identification of T_2 and T_2^* mismatch. Impaired iron transport may cause accumulation of iron deposits along the myelinated fibers as Parkinson's disease progresses [73]. Elevated iron signals along the ventral myelinated fibers were observed by both Perls' Prussian blue staining and LA-ICP-MS imaging, confirming such iron deposits near myelinated fibers. Taken together, the cytoarchitectural components of the SN, including neuromelanin, ferric iron, and myelinated fibers may altogether affect MRI signal properties, complicating interpretation of the results of *in vivo* studies. Reflecting the importance of topological interpretation of observed T_2 and T_2^* mismatch region, the comparisons of dorsal border length of the mismatch lines within posterior portion (excluding T_2 and T_2^* mismatch in ventral part of SN) showed a significant difference between G1 (mild reduction) and G2 (marked reduction) groups among the

patients, although the difference of the whole length of the mismatch line was insignificant between two groups. Thus, the topographical and morphological alterations in the T_2 and T_2^* mismatch region observed in Parkinson's disease patients should be determined through the extensive study of the related histopathology.

For *in vivo* experiments assessed at 3T, low-resolution and low sensitivity of T_2 and T_2^* maps compared to 7T postmortem MRI may account for the blurred T_2^*/T_2 and T_2^*/T_2^2 maps. This made it difficult to clearly delineate neuromelanin-rich regions; therefore, we instead leveraged the mismatch between the T_2 and T_2^* maps by subtracting the thresholded T_2 mask from the T_2^* mask to allow for more robust analysis of 3T *in vivo* datasets. High-resolution images acquired with 7T *in vivo* MRI may further improve the quality of the T_2^*/T_2 and T_2^*/T_2^2 maps to allow for better visualization of neuromelanin distribution and should be assessed in future investigations.

Neuromelanin-sensitive MRI methods have been utilized for evaluating the pathological changes induced by Parkinson's disease within the SNc. The first group to apply this methodology used a 2D T_1 -weighted fast spin-echo sequence to visualize the SN and locus coeruleus of subjects [14]. Others have also utilized similar fast spin-echo sequences with additional MT preparation pulses and various gradient echo sequences to overcome the limitations of the 2D fast spin-echo technique [17, 47, 50, 74, 75]. A recent study validated the clinical utility of neuromelanin-sensitive MRI by comparing postmortem brain tissue morphology and dopamine release measured with PET, and changes in cerebral blood flow [48]. The SNc volume measurements from neuromelanin-sensitive MRI have showed the significant reductions in Parkinson's disease patients [76, 77]. However, conventional methods are not fully quantitative and are limited by low-resolution images [78]. Besides neuromelanin, increased iron deposition in the SN can also enhance neuromelanin-related T_1 contrast [79]. In this study, the differences observed in neuromelanin-sensitive MRI were not consistent between normal control and Parkinson's disease brains. Such insignificant differences between normal controls and Parkinson's disease patients in neuromelanin-sensitive MRI may be attributed to facts that the duration of disease progression was relatively short (mean = 2.4 years, SE = 0.6 years) and the Hoehn and Yahr (H-Y) stages were rather early (I or II) for Parkinson's disease patients recruited in the current study.

Combined T_2 and T_2^* relaxometry-based neuromelanin MRI may have the potential to monitor pathophysiological changes associated with Parkinson's disease progression, which involves the loss of neuromelanin, coupled with iron accumulation. This complementary approach employing conventional neuromelanin-sensitive MRI and a novel technique based on transverse MR relaxometry will improve the evaluation of neuromelanin contents in the SN. In conclusion, the quantitative measurement of T_2 and T_2^* mismatch regions is a potential MRI biomarker to assess SN pathology in Parkinson's disease. Studies with a larger number of age-matched, elderly, normal subjects and

Parkinson's disease patients with diverse disease severity scores, higher magnetic field imaging, and accompanying histopathological examinations are required to further validate the clinical utility of this approach.

The original source of Chapter 3.2 is the article, Lee, H., Baek, S. Y., Kim, E. J., Huh, G. Y., Lee, J. H., & Cho, H. (2020). MRI T2 and T2* relaxometry to visualize neuromelanin in the dorsal substantia nigra pars compacta. *NeuroImage*, 211, 116625..

Chapter 4. Iron deposition on the myelinated fibers

4.1 Pathological validation of paramagnetic lesions in the white matter of Adult-onset leukoencephalopathy with axonal spheroids and pigmented glia

4.1.1 Introduction

Adult-onset leukoencephalopathy with neuroaxonal spheroids and pigmented glia (ALSP) is an autosomal dominant disease resulting from mutations in the colony-stimulating factor 1 receptor (*CSF1R*) gene [80]. The clinical presentation of ALSP includes personality and behavioral changes, dementia, parkinsonism, and seizures [80, 81]. The presence of myelin loss, which spares the subcortical U-fibers, reactive astrocytosis, axonal spheroids, and pigmented microglia in the white matter (WM) are pathological hallmarks [81].

Magnetic resonance imaging (MRI) typically shows T_2 hyperintense lesions in the periventricular, callosal, and deep WM, with frontal or frontoparietal predominance, and cerebral cortical atrophy corresponding to the WM lesions, as well as enlarged ventricles [80]. Thinning of the corpus callosum, abnormal signal intensity in the pyramidal tracts, diffusion-restricted lesions, and calcifications in the WM are characteristic MRI findings of ALSP [81]. Although these MRI features are supportive of a diagnosis of ALSP, they are not specific to ALSP, and may be suggestive of several alternate diagnoses, including multiple sclerosis (MS) and other demyelinating disorders [82].

It has been proposed that susceptibility-weighted imaging (SWI) is a sensitive technique for identifying iron depositions in WM pathological lesions in patients with MS [83]. The presence of pigmented microglia/macrophages in the WM lesions is particularly relevant in terms of MS pathology [84]. Similarly, iron-positive macrophages were found in ALSP brains and involved oxidative stress [80, 85]. In addition, calcifications in the WM can be detected in some patients with ALSP [81]. Therefore, SWI can be a useful complementary tool for identifying pathological mineral deposits in the WM lesions in ALSP.

Herein, we identified four adult-onset leukoencephalopathy with neuroaxonal spheroids and pigmented glia (ALSP) cases with *CSF1R* mutations who underwent SWI at 3T MRI and found the characteristic susceptibility-related phase contrast in the frontal white matter. To investigate the origin of the SWI contrast, postmortem brain from ALSP patient was examined using both 7T MRI and histopathology.

Table 4.1.1 Clinical and genetic findings of four patients with ALSP.

Patient	Sex	Age of onset (yr.)	Age at MRI (yr.)	Clinical Symptoms	CSF1R Mutation
1*	M	51	55	dementia, apathy, irritability, parkinsonism, gait disturbance, seizure	c.2381T>C, p.I794T
2	M	52	56	dementia, apathy, violence, gait disturbance, seizure	c.2675_2683del, p.C892_A895del
3	F	60	61	dementia, apathy, seizure	c.2381T>C, p.I794T
4	F	56	58	dementia, apathy, parkinsonism	c.2442+5G>A

* died at the age of 58

4.1.2 Methods

All enrolled patients carrying *CSF1R* mutations (NM 005211.3, NP 005202.2) underwent 3T MRI *in vivo* (Verio, Siemens, Erlangen, Germany). T_2 -weighted images (T2WI) were acquired using a 2D turbo spin echo sequence with TR = 3400–5000 ms, TE = 84–110 ms, and flip angle = 120–150°. SWI was performed with TR = 28 ms, TE = 20 ms, and flip angle = 15° in a 3D gradient echo sequence. The phase shift value in this study was for a left-handed coordinate system, which was positively correlated with iron levels. Routine brain CT scan was performed in three patients. This study was approved by Institutional Review Board. MRI and genetic analysis were performed after obtaining informed consent from all patients.

To validate SWI contrast, postmortem 7T MRI (Bruker, Karlsruhe, Germany) and a histopathological correlation study was performed in one case (case 1) after obtaining informed consent for the use of brain tissue prior to death. Formalin-fixed cortical tissue block from one of the frontal lobes was used for *ex vivo* experiments. A 2D multi-gradient echo sequence was used to obtain SWI with TR = 2000 ms, TE = 3.1–40 ms (10 echoes, increment = 4.1 ms), flip angle = 30°, field of view = 35 × 35 mm, matrix size = 256 × 256, in-plane resolution = 0.136 × 0.136 μm, slice thickness = 0.5 mm, and the number of slices = 20. For SWI, the four times of positive mask produced from phase image ($-\pi$ to π) were multiplied to the magnitude image. For quantitative susceptibility mapping (QSM), a susceptibility map was calculated from the complex phase information of the first three echoes of the gradient echo sequence [86]. For comparison, postmortem SWI was also obtained from a control brain of an individual without a history of neurological disease who had joined the Pusan National University Anatomical Donation Program and signed the informed consent.

After MRI scanning, the tissue block was sectioned at 8- μm thickness in accordance with 500- μm -thick *ex vivo* MR images. The sectioned slices were serially stained with hematoxylin and eosin (H&E) staining, Luxol fast blue staining (LFB), Perl's Prussian blue staining, ferritin IHC (polyclonal anti-ferritin light chain antibody, rabbit, 1:400; Abcam), CD68 IHC (monoclonal CD68 antibody, mouse, 1:300; Dako). Olympus virtual slide microscopy (Olympus, Tokyo, Japan) was used to scan all stained slides with a pixel size of 0.6836 μm^2 .

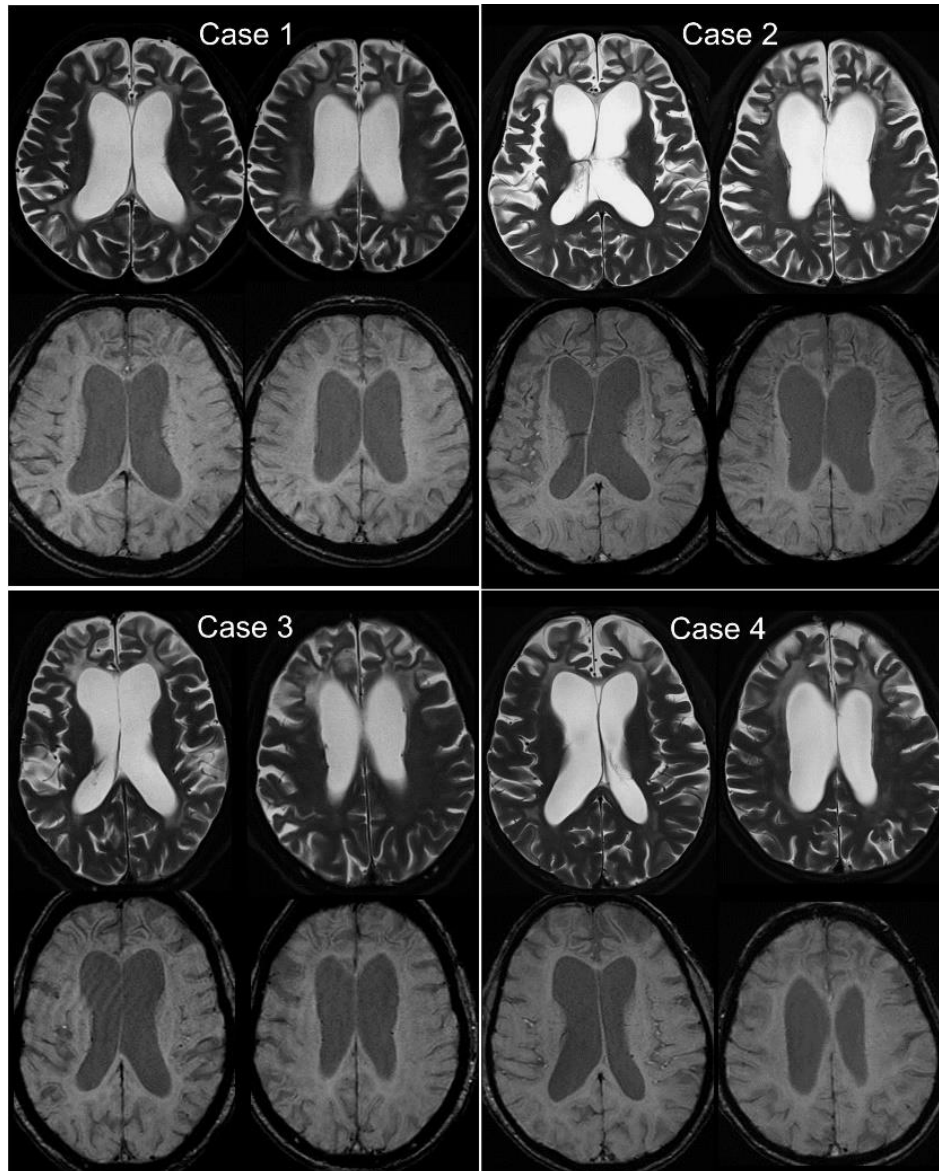


Figure 4.1.1 T_2 -weighted images and Susceptibility-weighted images on ALSP cases. In all ALSP cases, T_2 -weighted images shows symmetric bifrontal white matter hyperintensities with sparing of the subcortical U fibers and frontal-predominant atrophy. Susceptibility-weighted images demonstrate the characteristic ‘tree silhouette-like’ hypointense configuration of the frontal subcortical white matters.

4.1.3 Results

The demographic and clinical features from four patients are summarized in Table 4.1.1. The mean age at onset was 54.7 ± 4.1 years (range 51–60 years). Initial symptoms included personality and behavior changes (cases 1, 2, and 3), and parkinsonism (case 4). At the time of evaluation, all patients had neuropsychiatric symptoms including apathy or irritability, and they were diagnosed with dementia. Two patients showed parkinsonian features (cases 1 and 4). Three patients had recurrent seizures (cases 1, 2, and 3). Mutations in *CSF1R* were all located in the intracellular tyrosine-kinase domain of *CSF1R* encoded by exons 12–22 [87], and included a known missense mutation (c.2381T>C, p.I794T in cases 1 and 3), a novel splice donor site mutation (c.2442+5G>A in case 4), and a novel in-frame deletion of a single-codon (c.2675_2683del, p.C892_A894del in case 2).

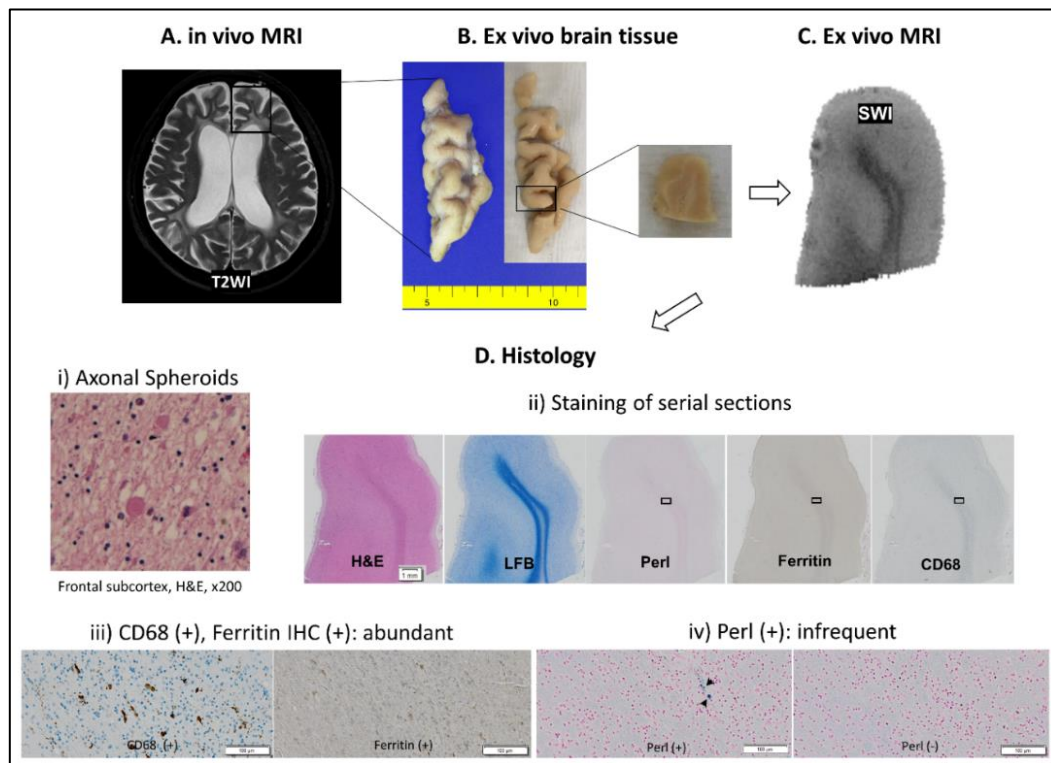


Figure 4.1.2 Schematic flow diagram for postmortem and *in vivo* MRI analysis. The region of the *in vivo* 3T MRI scan for case 1 (A) corresponds to the region shown in the *ex vivo* brain tissue (B) and 7T MRI scan (C). (D-i) Axonal spheroids in the frontal subcortex. (D-ii) Staining of serial sections with hematoxylin and eosin (H&E) staining, Luxol fast blue staining (LFB), Perl's Prussian blue staining (counterstained with nuclear fast red), ferritin immunohistochemistry (IHC), and CD68 IHC. (D-iii) Abundant CD68-positive, ferritin-positive cells. (D-iv) Infrequent positive staining for iron by Perl's Prussian blue staining.

In all patients, brain MRI showed frontal predominant atrophy and bifrontal periventricular, callosal, and deep WM lesions with sparing of the subcortical U fibers (Figure 4.1.1). In case 1, WM changes, cortical atrophy, and dilation of the lateral ventricles were more widespread. In case 4, periventricular WM changes were asymmetric, with more severe involvement on the contralateral side of the more severely affected limb. Diffusion-restricted or gadolinium-enhanced lesions were not detected in any case. No signal abnormalities were noted in the brainstem, cerebellum, or basal ganglia. SWI revealed the characteristic “tree silhouette-like” hypointense configuration of the frontal gyri alongside T_2 hyperintense WM lesions (Figure 4.1.1). On the phase images, the areas corresponding to linear hypointensity on SWI were seen as hyperintense (positive phase) which suggested a paramagnetic nature (Figure 4.1.2). Calcification was not identified in the corresponding areas.

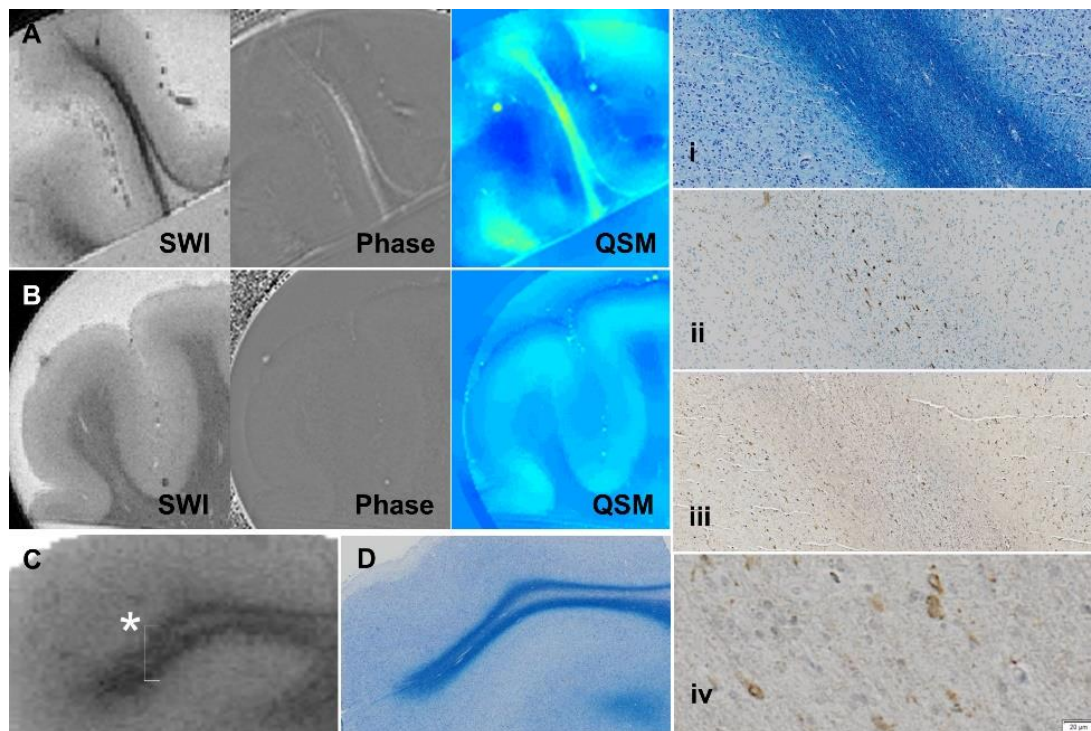


Figure 4.1.3 Postmortem MRI for ALSP brain with histological validation. Postmortem MRI for ALSP brain (A) manifests marked hypointensity on susceptibility-weighted images (SWI) with a positive phase shift on phase image and positive susceptibility values on quantitative susceptibility mapping (QSM) in contrast to the control brain (B). The signal hypointensity on postmortem SWI (C) is correlated with the density of white matter stained with Luxol fast blue (LFB, D). White box (*) on SWI defines where histologic images are taken at higher magnification (i~iv). (i) LFB staining shows symmetrical central myelin pallor with relatively preserved U fibers. (ii) CD68-positivity is most abundantly located in central demyelinating white matters. (iii, iv) Ferritin immunoreactivity is mainly observed in the CD68-positive zones and the white matter–cortical grey matter junction.

Postmortem MRI of ALSP brains revealed paramagnetic properties of the WM layers, in contrast to the control brain (Figure 4.1.3a and Figure 4.1.3b). These appeared as marked hypointense regions on SWI, with a positive phase shift on phase images and positive susceptibility values on QSM. Such paramagnetic signals were most prominent in the subcortical U-fibers. LFB staining showed symmetrical central myelin pallor with relatively preserved U fibers (Figure 4.1.3d and Figure 4.1.3e). In these areas, few axonal spheroids were present. CD68-positive microglial cells were most abundantly located in central demyelinating lesions (Figure 4.1.3f). Ferritin IHC staining was mainly observed in the CD68-positive zones and the WM–cortical grey matter junction (Figure 4.1.3g and Figure 4.1.3h). Co-registration between postmortem MRI and histology demonstrated that the signal hypointensity on postmortem SWI was correlated with the density of WM stained with LFB (Figure 4.1.3c and Figure 4.1.3d). However, positive staining for iron by Perl’s Prussian blue staining was infrequently found in the corresponding paramagnetic WM lesions. There were no dystrophic calcifications.

4.1.4 Discussions and Conclusions

To date, the SWI findings of ALSP have not been described. SWI demonstrated the prominent susceptibility-related phase contrast with a tree silhouette-like configuration in the frontal subcortical WM, accompanied by striking frontal atrophy. This unique tissue contrast on SWI may help to characterize ALSP further.

The characteristic SWI abnormalities observed may be associated with the location of WM lesions. The prominent SWI contrast regions colocalized with iron-rich WM regions in the normal brain. Iron concentrations are higher in the frontal than in occipital regions, and are prominent in the subcortical U-fibers [83, 88]. In our postmortem study, the higher spatial resolution obtained with 7T MRI further clarified the topographical details of the hypointense signals. The phase and susceptibility maps of the postmortem brain tissue disclosed paramagnetic properties in remnant U-fibers. In the normal brain, on the contrary, the WM showed diamagnetic susceptibility.⁵ Similar MRI abnormalities in the WM lesions have recently been described in patients with MS and progressive multifocal leukoencephalopathy (PML) [84, 89]. In MS, higher amounts of iron were found at the WM–cortical grey matter junction, reflected by transverse relaxivity, R_2^* , and phase images. Iron deposits were found surrounding the core of the focal WM lesions, and colocalized with ferritin- and iron-enriched activated microglia/macrophages [84]. PML often occurs at the subcortical–juxtacortical WM involving the U-fibers [89]. SWI hypointensities potentially explained by iron deposition were observed within the cortex and/or U-fibers adjacent to the multifocal WM lesions of PML patients [89]. Compared with MS and PML, a contiguous linear pattern confined to subcortical WM is a unique feature of ALSP.

The paramagnetic properties of WM in our patients might also be caused by ferritin-positive microglia. In the postmortem WM tissue, ferritin immunoreactivity colocalized with CD68-positive microglia showing a dystrophic and degenerating phenotype [89]. In general, ferritin IHC demonstrates iron in microglia [90, 91]. Accumulation of ferritin-bearing microglia can cause an increase in susceptibility. However, the distribution of ferritin did not precisely match the MRI contrast. Ferritin immunoreactivity was found mainly in the periphery of the remnant U-fibers, particularly in severely demyelinated WM fibers. The distribution of ferritin was not accompanied by sufficient quantities of iron in Perl's Prussian blue staining to induce significant MRI signal changes. In fact, it has previously been reported that the WM lesions in ALSP brains stained variably for iron [80, 85, 92]. In some cases, only rare cells were positive for iron stains [92]. It is unclear whether increased expression of ferritin in ALSP is associated with increased iron uptake [90]. Further studies using chemical assessment of iron concentration or X-ray fluorescence, a more powerful assay for mapping the true iron distribution, is needed to confirm the origin of the magnetic susceptibility [83].

Non-iron factors, such as changes in subcortical WM architecture, may also alter SWI phase contrast behavior. Myelin is the dominant source of anisotropic volume susceptibility in the WM [93]. The phase of the gradient echo sequence depends on the orientation of the myelin sheet with respect to the main magnetic field [82, 84, 93]. Demyelination of central WM-sparing iron-rich U-fibers seems to underlie the complicated susceptibility layers, which may lead to local phase changes in the MR phase images.

This study is limited by the small sample size. SWI was not always performed in all patients with ALSP, which may have created a bias. Since we did not use DAB intensification, our histopathological studies may have underestimated the actual iron levels [94]. Indeed, deoxyhemoglobin, an *in vivo* iron source of SWI contrast, was absent in postmortem specimens [84].

Although questions remain on how ferritin-positive microglia affect MRI signals, the WM architecture changes due to demyelination of the central WM-sparing U-fibers may mainly contribute to the paramagnetic susceptibility contrast.

The original source of Chapter 4.1 is the article, Kim, M., Lee, H., Cho, H. J., Young Chun, S., Shin, J. H., Kim, E. J., ... & Lee, J. H. (2017). Pathologic correlation of paramagnetic white matter lesions in adult-onset leukoencephalopathy with axonal spheroids and pigmented glia. *Journal of Neuropathology & Experimental Neurology*, 76(11), 924-928..

4.2 Accumulated iron on the myelinated fibers of the oculomotor nerve in the brain of progressive supranuclear palsy

4.2.1 Introduction

The common pathological characteristics of Parkinsonism are elevated iron deposition with neuronal degeneration in the substantia nigra (SN) [5, 95]. Several studies have investigated the neurochemistry of iron-containing molecules involved in the pathology of Parkinsonism [96, 97]. Labile iron in the brain is associated with the generation of hydroxyl radicals and reactive oxygen species, leading to oxidative stress and cellular damage [1, 98]. Specifically, high iron accumulation in the SN associated with disease progression results in detrimental damage to neuromelanin-containing dopaminergic neurons [99, 100]. Iron accumulation in the SN can be visualized and monitored using *in vivo* magnetic resonance imaging (MRI) using iron-sensitive sequences. R_2^* ($1/T_2^*$) map and quantitative susceptibility mapping (QSM) have been applied to quantify the iron concentration within the SN of patients of Parkinson's disease (PD) and other Parkinsonian syndromes, including progressive supranuclear palsy (PSP), and compared to those in healthy controls [101].

PSP is a degenerative parkinsonism characterized by hyperphosphorylated tau protein pathology and neuronal cell loss in cortical and subcortical structures, including the SN and midbrain structures, globus pallidus, and subthalamic nucleus [102, 103]. Supranuclear vertical gaze palsy with significant midbrain atrophy has been recognized as a cardinal feature of PSP [104, 105]. Iron accumulation within the PSP brain also serves as a potential biomarker in *in vivo* MRI studies, and it has the ability to help distinguish patients with PSP from normal controls [101, 106, 107]. Significant increases in iron-related signals have been found in the SN, red nucleus (RN), and globus pallidus of patients with PSP [101]. In postmortem MRI studies with pathological validation, the microstructural destruction of the borders and internal architecture of the SN is far greater in PSP than that in PD [108, 109]. In FLASH MR images, the hypointense pixels near the boundary of the RN that adjoin the hypointense pixels of the SN resulted in less delineation between the structures of the PSP midbrain [108]. However, the exact underlying pathology of these alterations is unknown.

This work focuses on verifying the histological origin of increased MR susceptibility contrast between the SN and RN in the PSP midbrain and on ascertaining its utility as an *in vivo* diagnostic marker for PSP brains, which can differentiate these patients from healthy controls and patients with PD. 7T high-resolution postmortem MRI of PSP and normal brains along with mutually independent iron characterization techniques including histopathology and mass spectrometry were collectively

investigated. 3T *in vivo* iron-related MRIs of the brains of healthy controls, PD, and PSP were compared.

4.2.2 Methods

This study was approved by the Pusan National University Yangsan Hospital and Ulsan National University of Science and Technology institutional review board. All procedures, including the *in vivo* MRI, postmortem MRI, mass spectrometry, and histopathological analysis were conducted according to the guidelines of the Helsinki Declaration. The images were processed using in-house developed MATLAB codes (version R2016a, MathWorks, Natick, MA, USA).

Postmortem MRI and histopathological analysis

Midbrain specimens of an 86-year-old female without any neurodegenerative disease were acquired from the Pusan National University Anatomical Donation Program. A diseased midbrain tissue, which was characterized by severe midbrain atrophy, frontotemporal lobar degeneration, tau pathology, and depigmentation in the SN, from a 67-year-old male diagnosed with PSP was obtained from the Pusan National University Hospital Brain Bank. The formalin-fixed midbrain samples were stored in a 4 °C refrigerator for more than 2 years for sufficient stabilization of MR properties [110, 111]. Formalin fixation redistributes iron within the tissues [59]. Although it may alter the staining intensity and the absolute transverse relaxometry values (R_2^*) in postmortem MR images, the contrast of postmortem SWI, R_2^* , and QSM within brain tissues were maintained from *in vivo* MRI [59, 112].

Two tissues were placed in 50 mL syringes separately after removing air bubbles because bubbles around the tissue surface cause susceptibility artifacts on MR images. High-resolution MR acquisitions were performed on tissues using 7T preclinical MRI (Bruker, Karlsruhe, Germany) at Ulsan National University of Science and Technology to validate the origin of the *in vivo* MRI contrast. SWI, R_2^* map, and QSM were used to evaluate iron and myelin contents in 2D multiple gradient echo sequence acquired using the following parameters: repetition time (TR) = 2,000 ms, echo time (TE) = 3.3-81.2 ms (20 echoes with $\Delta TE = 4.1$ ms), flip angle = 30°, field of view = 35 × 35 mm, matrix size = 256 × 256, slice thickness = 500 μm , and number of slices = 20. The slice geometry was perpendicular to the main magnetic field. SWI was acquired using magnitude and phase images of TE = 15.6 ms. The R_2^* map was obtained from the magnitude image by mono-exponential fitting of the T_2^* transverse relaxation curve on each voxel. QSM was reconstructed from phase images of five tilted orientations using the Laplacian boundary value (LBV) algorithm for background field removal and calculation of susceptibility through multiple orientation sampling (COSMOS) [27, 63]. T_1 -weighted images were also acquired with 2D RARE sequence for co-registration with histological analysis using the following

parameters: TR = 800 ms, TE = 8 ms, flip angle = 30°, field of view = 35 × 35 mm, matrix size = 256 × 256, slice thickness = 500 μm, and number of slices = 20.

After the MR scan, tissue samples were subjected to histopathological analysis, which is a gold standard to demonstrate the effect of underlying elements on the corresponding MR images. For the tissue cryoprotection, to minimize osmotic stress and ice formation during cooling, tissues were sequentially embedded in 10%, 20%, and 30% sucrose in Phosphate-buffered saline solution until they sank. Thin slides of 50 μm thickness were generated using a cryostat (CM1950, Leica Biosystems, Nussloch, Germany). Ten sectioned slides (thickness 50 μm) were prepared from one corresponding MR image (thickness 500 μm). Of ten sections, three adjacent slides were used serially for Perls' Prussian blue staining, Luxol fast blue staining, and LA-ICP-MS, respectively.

Perls' Prussian blue staining was performed for detecting ferric iron distribution. For Perls' Prussian blue staining, the slides were incubated in a 1:1 mixed solution of 20% HCl and 20% potassium ferrocyanide for 30 min. Luxol fast blue staining was performed to identify the distribution of myelinated fibers by soaking the tissues in 0.1% filtered Luxol fast blue solution at 65 °C in an oven overnight and counterstained with 0.1% cresyl violet acetate solution. The histological slides were imaged using Virtual Microscope (Olympus Optical Co. Ltd, Tokyo, Japan).

LA-ICP-MS was conducted to detect all molecular forms of iron within brain tissues on the slide that was neither stained with Perls' Prussian blue nor Luxol fast blue. Two-dimensional images of ⁵⁶Fe and ¹³C intensity were obtained by line scan using a quadrupole ICP-MS device, iCAP TQ (ThermoFisher Scientific, Bremen, Germany) with a femtosecond laser (1,030 nm) ablation system (J200, Applied Spectra, Inc, Fremont, CA, USA). For the comparison of iron concentration between tissues, ⁵⁶Fe intensity was normalized by ¹³C intensity to compensate sample-to-sample variations in laser ablation measurements, as ¹³C is a suitable internal standard for quantitative elemental bio-imaging [113].

Table 4.2.1 Demographic and clinical characteristics of PD, PSP, and healthy control groups.

	PD	PSP	Control
Subjects (M/F)	3/2	4/1	2/3
Age (years)	61.2 ± 3.7	64.2 ± 2.2	61.0 ± 2.7
Disease duration (years)	4.8 ± 3.1	3.4 ± 0.5	-
H-Y stage	2.0 ± 0.5	3.4 ± 0.5	-

Data are shown as mean ± standard deviation. Control = healthy control; H-Y = Hoehn & Yahr; PD = Parkinson's disease; PSP = Progressive supranuclear palsy.

For direct comparisons, postmortem MRI was co-registered with corresponding histological results and LA-ICP-MS images. Due to the different spatial resolutions among images, MR images and images of ^{56}Fe and ^{13}C intensity from LA-ICP-MS were up-sampled by bicubic interpolation before co-registration. The two-dimensional rigid transformation of rotation and translation was performed on up-sampled MR images and up-sampled images of ^{56}Fe and ^{13}C intensity from LA-ICP-MS to match the images of Luxol fast blue staining. The same transformation method was also used for the co-registration of the image of Perls' Prussian blue staining to the image of Luxol fast blue staining.

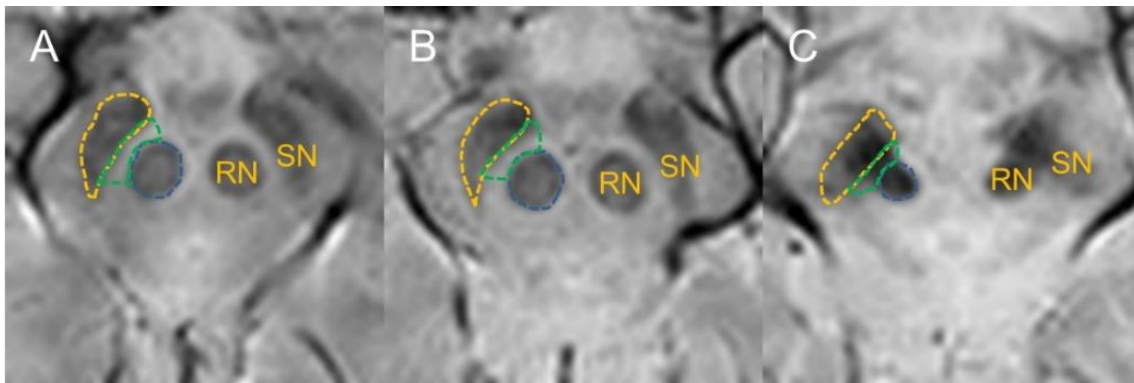


Figure 4.2.1 The delineation of ROI surrounding the region between SN and RN in SWI. A: Representative case (61F) of the healthy control group. B: Representative case (60M) of the PD group. C: Representative case (66M) of the PSP group. The orange dotted line showed the boundary of SN. The blue dotted line showed the boundary of RN. The green dotted line showed the ROI surrounding the region between SN and RN. PD = Parkinson's disease; PSP = progressive supranuclear palsy; RN = red nucleus; ROI = region of interest; SN = substantia nigra; SWI = susceptibility-weighted imaging.

In vivo MRI

Five patients with PSP, along with five age-matched patients with PD and five age-matched healthy controls, were included in this study. The demographic features of all participants are summarized in Table 4.2.1. Patients were clinically diagnosed by a movement disorder neurologist in accordance with the established criteria for each disorder [114, 115]. Although there was no significant difference in age and disease duration between patients with PD and those with PSP, the H-Y stage was significantly higher in patients with PSP ($p = 0.008$). All subjects provided informed consent and underwent 3T *in vivo* MRI (Magnetom Skyra, Siemens, Erlangen, Germany) at Pusan National University Yangsan Hospital. SWI, R_2^* map, and QSM were taken with a 2D gradient echo sequence using the following parameters: TR = 2,030 ms, TE = 3.1-29.9 ms (6 echoes with $\Delta\text{TE} = 4.8, 5.5, \dots, 5.5$ ms), flip angle = 60° , field of view = 192×192 mm, matrix size = 192×192 , slice thickness = 2 mm, and number

of slices = 60. SWI was acquired using the magnitude and phase images of TE = 24.6 ms. The R_2^* map was obtained using the same technique of postmortem MRI. QSM was reconstructed using MATLAB-based software, STI-Suite (version 3.0, University of California, Berkeley, CA, USA, <https://people.eecs.berkeley.edu/~chunlei.liu/software.html>). Among the 60 slices, the slice of the second level in the rostral direction showing the SN with a clear shape of the RN was consistently selected for each subject for the analysis.

The line profile of normalized SWI intensity, R_2^* , and QSM across the SN and RN were plotted along the two different lines for each group (right and left sides of five subjects in each group). SWI intensity was normalized by the maximum intensity value of each line profile. The white matter region between the SN and RN was manually delineated in SWI by H.L. as shown in Figure 4.2.1. The quantitative values of R_2^* and QSM within the region between the SN and RN using the same ROI from SWI were compared among the three groups using a Kruskal-Wallis H test. Bonferroni correction was performed for multiple comparisons with significance levels of $0.05/3=0.0166$.

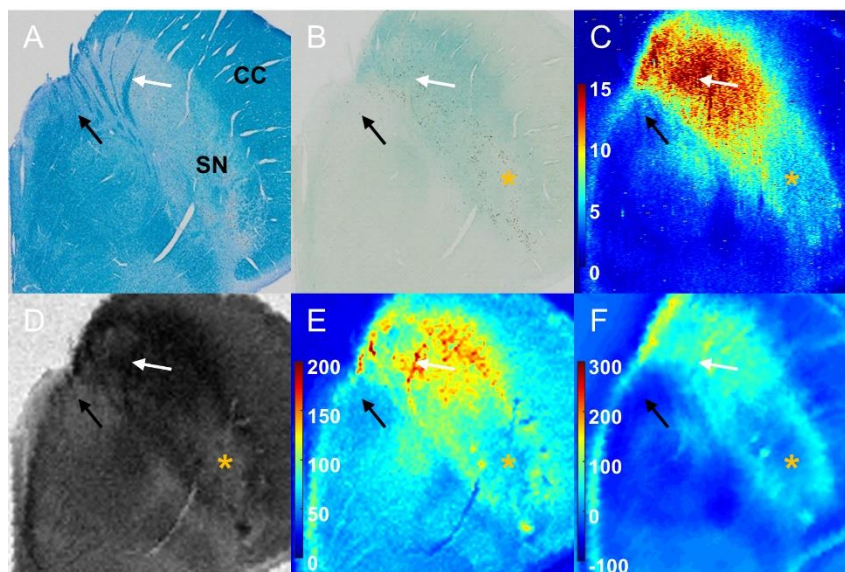


Figure 4.2.2 Histopathology and LA-ICP-MS with multimodal MRI on the postmortem SN of an 86-year-old normal female. (A): Luxol fast blue staining; (B): Perls' Prussian blue staining; (C): $^{56}\text{Fe}/^{13}\text{C}$ intensity from LA-ICP-MS imaging (a.u.); (D): SWI; (E): R_2^* map (1/s); (F): QSM (ppb); White and black arrows indicate myelinated fibers at anterior SN and oculomotor nerve. Orange asterisk shows the structure of nigrosome-1. CC = crus cerebri; LA-ICP-MS = laser ablation - inductively coupled plasma - mass spectrometry; QSM = quantitative susceptibility mapping; SN = substantia nigra; SWI = susceptibility-weighted imaging.

4.2.3 Results

Postmortem study

The co-registered results of multimodal high-resolution MRI, histopathology, and the two-dimensional image of iron distribution from laser ablation-inductively coupled plasma-mass spectrometry (LA-ICP-MS) of the postmortem normal and PSP brains are presented in Figure 4.2.2 and Figure 4.2.3, respectively.

Overall, the myelinated fibers at the anterior SN and third cranial nerve (oculomotor nerve) fascicles were observed in Luxol fast blue staining (white arrow for myelinated fibers at the anterior SN and black arrow for the oculomotor nerve fascicles in Figure 4.2.2A and Figure 4.2.3A). Ferric iron deposition was detected using Perls' Prussian blue staining (Figure 4.2.2B and Figure 4.2.3B). The stained ferric iron was broadly distributed within the SN. The region of elevated intensity for $^{56}\text{Fe}/^{13}\text{C}$ in LA-ICP-MS imaging (Figure 4.2.2C and Figure 4.2.3C) corresponded with the areas of the stained ferric iron deposits (blue blush in Perls' Prussian blue staining) [116].

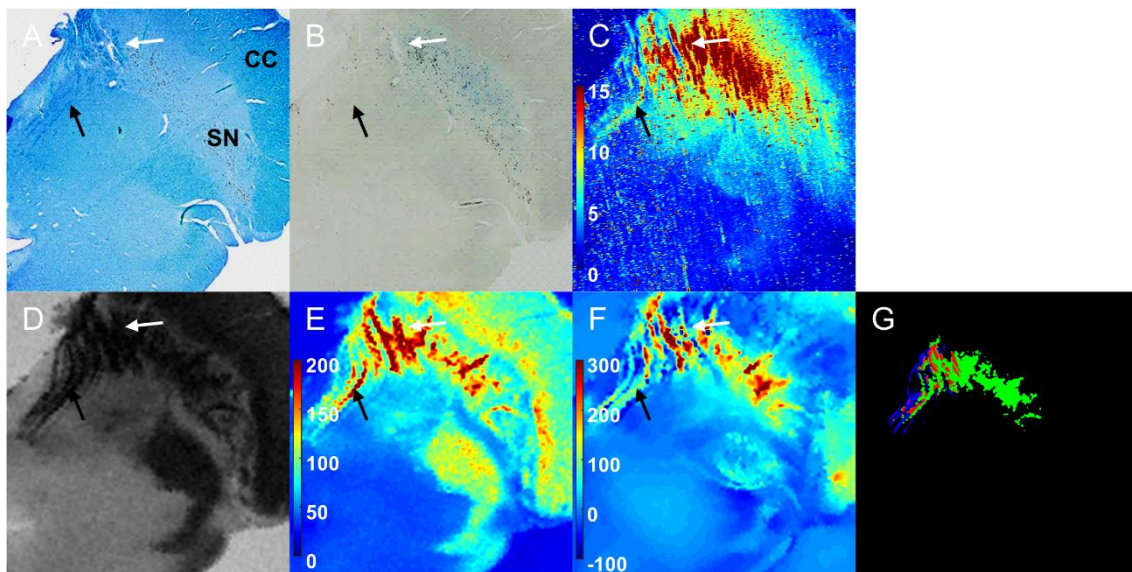


Figure 4.2.3 Histopathology and LA-ICP-MS with multimodal MRI on the postmortem SN of a 67-year-old male with PSP. (A): Luxol fast blue staining; (B): Perls' Prussian blue staining; (C): $^{56}\text{Fe}/^{13}\text{C}$ intensity from LA-ICP-MS imaging (a.u.); (D): SWI; (E): R_2^* map (1/s); (F): QSM (ppb). (G) The overlap (red) between myelinated fiber (blue) and hypointense SWI area (green). White and black arrows indicate myelinated fibers at anterior SN and oculomotor nerve. CC = crus cerebri; LA-ICP-MS = laser ablation - inductively coupled plasma - mass spectrometry; PSP = Progressive supranuclear palsy; QSM = quantitative susceptibility mapping; SN = substantia nigra; SWI = susceptibility-weighted imaging.

In the case of the normal brain, the area of deposited iron corresponded to the hypointense pixels in susceptibility-weighted imaging (SWI) (Figure 4.2.2D), and large R_2^* values were correspondingly observed in the same area (Figure 4.2.2E). In the QSM (Figure 4.2.2F), ferric iron deposition was shown as paramagnetic molecules. The structure of the so-called nigrosome-1 (the area of the orange asterisk) was detected as a hyperintense area in the SWI. This area was also described as an oval-shaped area with lower R_2^* values and susceptibility compared to those of surrounding tissues. Nigrosome-1 had lightly stained iron distribution in Perls' Prussian blue staining and a low intensity of iron ($^{56}\text{Fe}/^{13}\text{C}$). The R_2^* map and QSM further showed linear myelinated fibers with moderately high values distributed in the anterior SN (white arrow in each image). No iron accumulation along the oculomotor nerve fascicles (black arrow) was observed on iron-related MRI or $^{56}\text{Fe}/^{13}\text{C}$ from LA-ICP-MS.

In the case of PSP, the volume atrophy of the midbrain was apparent compared to that in normal SN. Similar to a normal SN, iron deposition was identified as large R_2^* values in Figure 4.2.3E. In particular, the region with both large values in the R_2^* map and positive susceptibility values in the QSM (Figure 4.2.3F) included the oculomotor nerve (black arrow) fascicles and myelinated fibers in the anterior SN (white arrow) identified from Luxol fast blue staining. The $^{56}\text{Fe}/^{13}\text{C}$ intensity from LA-ICP-MS also showed a significant iron signal in the area of myelinated fiber at the anterior SN and oculomotor nerve fascicles, directly indicating iron accumulation along the oculomotor nerve. The spatially overlapped region (red) between segmented myelinated fibers from Luxol fast blue staining (blue) and hypointense regions from SWI (green) is shown in Figure 4.2.3G. On the other hand, such iron distribution along the myelinated fibers in the PSP brain was not sensitively stained in the Perls' Prussian blue staining (Figure 4.2.3B).

The myelinated fibers of the oculomotor nerve detected in Luxol fast blue staining were not distinctively shown in the R_2^* map and QSM as indicated by red arrows. The mild iron concentration along myelinated fibers in the two control cases was not enough to overwhelm the effect of diamagnetic myelinated fibers in QSM, which was clearly observed in 67-year-old male PSP brains.

In vivo MRI

For *in vivo* MRI, representative MR images of the SWI, R_2^* map, and QSM showing rostral SN in healthy control, PD, and PSP groups are presented in Figure 4.2.4. The values of R_2^* map and QSM in SN were highest in patients with PSP, followed by patients with PD and then healthy controls. Marked atrophy of the midbrain was observed in all patients with PSP compared to those of healthy controls and patients with PD in the same field of view. In the SWI, a clear hyperintense boundary was identified in the region between the hypointense SN and the hypointense RN in healthy controls and patients with PD (Figure 4.2.4A-I and Figure 4.2.4B-I). However, in the case of PSP, the hypointense area was shown

at the areas bridging the SN and RN as an atypical connection between two tissues with blurred boundaries (Figure 4.2.4C-I). This connection was also identified in the R_2^* map and QSM of patients with PSP (Figure 4.2.4C-II and Figure 4.2.4C-III).

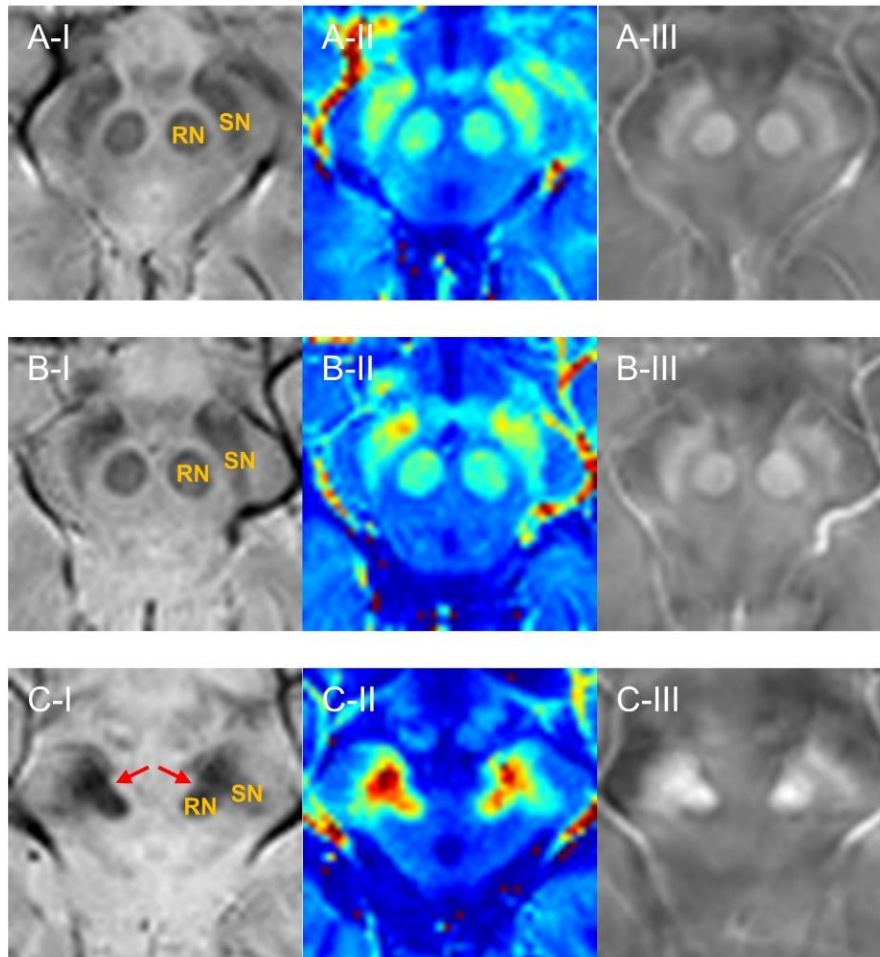


Figure 4.2.4 The representative MRI showing the SN and RN. A: Representative case (61F) of the healthy control group. B: Representative case (60M) of the PD group. C: Representative case (66M) of the PSP group. The red arrows in Figure C-I show the hypointensity in the region between SN and RN. (I): SWI; (II): R_2^* map; (III): QSM. PD = Parkinson's disease; PSP = progressive supranuclear palsy; QSM = quantitative susceptibility mapping; SN = substantia nigra; SWI = susceptibility-weighted imaging; RN = red nucleus.

In Figure 4.2.5, the respective line profiles of normalized SWI intensities are presented across the SN and RN along the two separate lines of the three groups, as shown in Figure 4.2.5A. To visualize the selectivity of such lines to myelinated white matter, the myelin of the oculomotor nerve fascicles passing by the RN and the myelin in the anterior SN were connected by red lines in Luxol fast blue staining, as

shown in Figure 4.2.5B. Ten line profiles of healthy controls along both red and blue lines in the SWI (Figure 4.2.5C-I and Figure 4.2.5C-IV) showed hyperintensity in the white matter region (WM in the x-axis) bridging the SN and RN. Hyperintense areas were also maintained in the white matter region between the SN and RN in patients with PD (Figure 4.2.5C-II and Figure 4.2.5C-V). Conversely, for patients with PSP, the SN, RN, and white matter region between the two tissues were hypointense, which resulted in blurred structural boundaries (Figure 4.2.5C-III and Figure 4.2.5C-VI). The line profiles for R_2^* and QSM values along the blue line in SWI are presented in Figure 4.2.6. The line profiles of R_2^* and QSM showed a concave pattern in the region between the SN and RN in both healthy controls and patients with PD, but such trend was significantly decreased in patients with PSP.

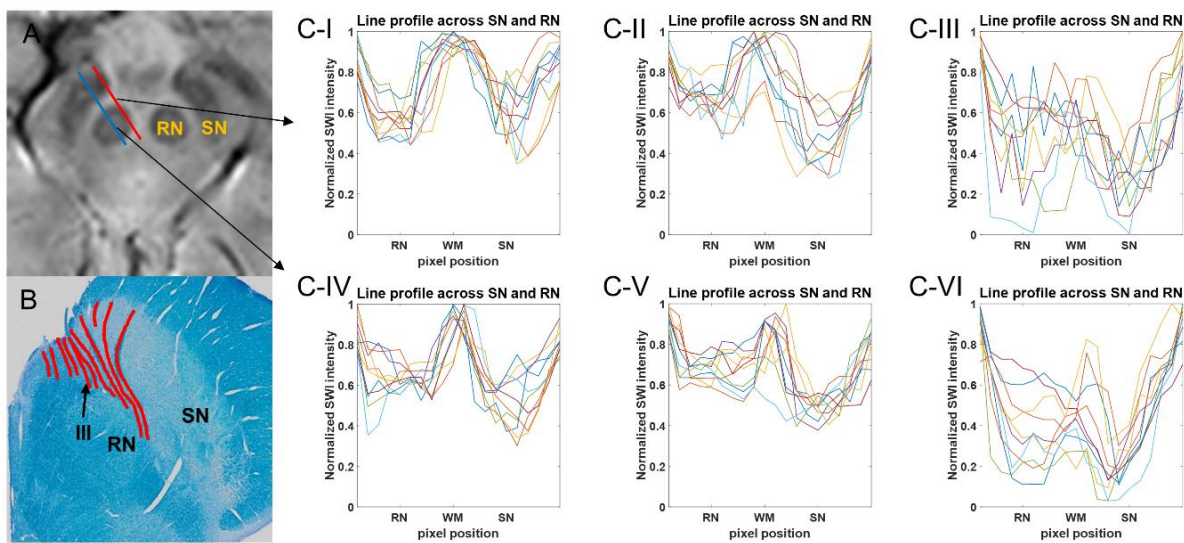


Figure 4.2.5 The line profile of normalized SWI intensity across the SN and RN. (A): SWI (B): Luxol fast blue staining with red lines for myelin distribution; (C-I), (C-IV): The line profile of normalized SWI intensity of healthy controls; (C-II), (C-V): The line profile of normalized SWI intensity of patients with PD; (C-III), (C-VI): The line profile of normalized SWI intensity of patients with PSP. The line profiles of (C-I~C-III) were delineated along the red line in SWI. The line profiles of (C-IV~C-VI) were delineated along the blue line in SWI. PD = Parkinson's disease; PSP = progressive supranuclear palsy; SN = substantia nigra; RN = red nucleus; WM = white matter between SN and RN.

The mean and standard deviation of R_2^* and QSM values in the region bridging the SN and RN were compared among the three groups (Table 4.2.2). R_2^* and QSM values of PSP were significantly higher than those of the other two groups (R_2^* : $p = 0.008$ with controls, $p = 0.008$ with PD; QSM: $p = 0.008$ with controls, $p = 0.008$ with PD). However, the differences in R_2^* and QSM values between controls and PD groups were negligible ($p = 0.421$ and $p = 1$, respectively) in the region bridging the SN and

RN. For the datasets with separated left and right sides of the brain, R_2^* and QSM values of PSP were more significantly distinguishable from those of other two groups, as demonstrated by the p -values in parentheses.

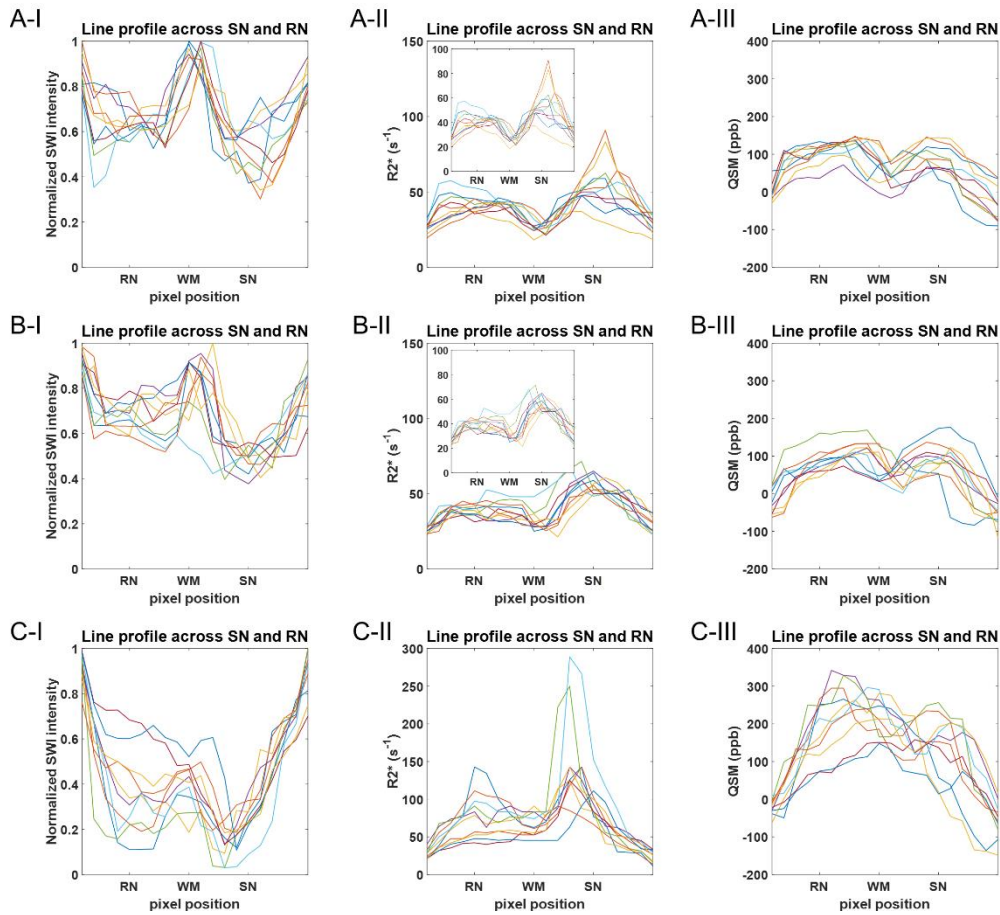


Figure 4.2.6 The line profiles across SN and RN. A is for the representative case of a group of healthy controls. B is for the representative case of the PD group. C is for the representative case of the PSP group. The line profiles were delineated along the same blue line used in SWI (Figure 4.2.5A) of each subject. (I): The line profile of normalized SWI intensity; (II): The line profile of R_2^* (The same plot of A-II and B-II with magnified y -axis was exhibited as inset figure); (III): The line profile of QSM. PD = Parkinson’s disease; PSP = Progressive supranuclear palsy; QSM = quantitative susceptibility mapping; RN = red nucleus; SN = substantia nigra; SWI = susceptibility-weighted imaging; WM = white matter region between SN and RN.

4.2.4 Discussions and Conclusions

The main finding in this study is that iron deposition along the myelinated fibers at the anterior SN

and oculomotor nerve fascicles in the brain of patients with PSP can be visualized using multiple independent approaches, such as 7T postmortem MRI, histological analysis, mass spectrometry, and *in vivo* 3T MRI. Our postmortem examinations showed that the increased MR susceptibility contrast between the SN and RN identified in patients with PSP is likely to originate from excessive iron deposition along the myelinated nerves between these two structures. To our knowledge, this is the first report demonstrating a higher level of iron deposition along the myelinated fibers at the anterior SN and oculomotor nerve fascicles in the vicinity of the SN and RN of patients with PSP compared to those of patients with PD and normal controls by using R_2^* , QSM, and LA-ICP-MS.

Table 4.2.2 Comparison of R_2^* and QSM in the region between SN and RN among PD, PSP, and control.

	Control	PD	PSP	Kruskal-Wallis		post-hoc (p)		
				χ^2	p	Control vs. PD	Control vs. PSP	PD vs. PSP
R_2^* values (s^{-1})	33.7 \pm 1.6	37.3 \pm 5.6	54.9 \pm 8.0	9.8	0.008*	0.421 (0.473)	0.008* (< 0.001**)	0.008* (0.002**)
QSM (ppb)	31.2 \pm 15.4	34.1 \pm 11.9	116.2 \pm 23.7	9.4	0.009*	1 (0.910)	0.008* (< 0.001*)	0.008* (< 0.001**)

Data are shown as mean \pm standard deviation.

Post-hoc (p) = p -values from post-hoc analysis of Mann-Whitney U test.

*: $p < 0.05$ (For post-hoc analysis, *: $p < 0.05/3$ and **: $p < 0.005/3$ after Bonferroni correction).

Control = healthy control; PD = Parkinson's disease; PSP = Progressive supranuclear palsy; SN = substantia nigra; RN = red nucleus.

Atrophy of the midbrain, which is a recognized characteristic in patients with PSP, may shorten the gap between the SN and RN. The shortened gap between the SN and RN probably causes an atypical connection between the two structures with blurred boundaries in low-resolution on *in vivo* MRI. Regardless of the volume loss in PSP brain, the fibers of oculomotor nerve would still present between the SN and RN. In our postmortem examinations of the PSP midbrain, Luxol fast blue staining showed the distribution of myelinated fibers at the anterior SN and the oculomotor nerve fascicles, which had a considerably high iron ($^{56}\text{Fe}/^{13}\text{C}$) signal intensity in the LA-ICP-MS image. The corresponding area had large R_2^* values and positive susceptibility values in the QSM. The spatial overlap between myelinated

fibers from Luxol fast blue staining and the hypointense region in SWI demonstrated that the myelinated fibers with high iron concentration were non-invasively observed in the iron-related MRI. However, Perls' Prussian blue staining, which is the conventional method used to determine the distribution of ferric iron within brain tissues, was less sensitive for staining myelin-associated iron.

It is still unclear why there is a high concentration of iron deposits along the myelinated fibers of the oculomotor nerve in association with PSP progression. There are several possible explanations for this abnormal iron deposition. 1) In human studies, high levels of iron have been reported to co-localize with hyperphosphorylated tau aggregates [117]. Tau-containing globose neurofibrillary tangles are prevalent in the PSP midbrain, including in the oculomotor nerve complex [118]. 2) Anatomically, the fibers of the oculomotor nerve fascicles from the nucleus pass by the RN and SN, and these two structures contain a high level of iron concentration [109]. Excessive iron accumulation within both the SN and RN can also cause abnormal iron deposition along the nearby myelinated fiber. 3) The vulnerability of myelinated fibers and oligodendrocytes to oxidative stress may be further accelerated by their high iron environment as myelination and axon maturation require iron consumption [60, 119]. The dysfunction of the iron homeostasis mechanism in myelinated fibers, such as impaired iron transportation of the iron transport tract and imperfect iron excretion from the neurons, can cause high iron deposition along the associated myelinated fibers [73, 120]. The increased iron level along the myelinated fiber of the oculomotor nerve is likely to result in neuronal damage with disease progression [99].

Although white matter, including myelinated fibers, is originally considered the main diamagnetic source in the brain due to its heavy phospholipid component, a high level of iron-containing molecules is also stored in myelin and oligodendrocytes as they have high iron requirements [121]. As demonstrated in the present study, iron deposition along the myelinated fiber around the SN can be a specific endogenous iron cluster, because the overloads of iron deposition along myelinated fibers overwhelm diamagnetism and induce paramagnetism as a myelin-iron complex [121, 122]. Moreover, various forms of endogenous iron clusters are distributed within the SN, including the neuromelanin-iron complex, reactive ferric irons in neurons and glial cells, pathological hallmarks of disorders apart from iron such as α -synuclein or tau, and the heme iron in microvessels crossing the SN [16, 70, 75, 123]. All these endogenous iron clusters within the SN need to be interpreted with care in *in vivo* iron-related MR contrast.

This study had several limitations. First, the postmortem sample size was small. However, a previous postmortem study on the SN of control and PSP brains showed consistent hypointensity between the SN and RN only in the PSP brain [108]. Second, we have not presented the corresponding images from postmortem PD midbrains for direct comparison between PD and PSP midbrain tissues. In PD, the most

severely affected regions are reported to be nigrosomes, containing most dopaminergic neurons, at the posterior SN [124]. The evaluation of the presence of nigrosome-1 in the posterior SN (rather than the anterior SN in the analysis of PD brain) in MRI has been utilized as a promising biomarker for PD diagnosis. Third, the disease severity (H-Y stage) was different between patients with PD and PSP, which may influence MR contrast. PSP is known to progress more rapidly than PD, and it is difficult to match disease duration and H-Y stage together between the two groups [125]. Further investigation should be pursued on a larger number of subjects with no significant differences in age, sex, and disease severity in each group. Histopathological validation is also recommended for postmortem PD and PSP brains with a large sample in future studies.

In conclusion, the current study has demonstrated excessive iron deposition along the myelinated fiber at the anterior SN and the third cranial nerve (oculomotor nerve) in the PSP brain, applied this knowledge to understand the *in vivo* iron-related MR contrast seen in patients with PSP, and compared it to those of healthy controls and patients with PD. Consequently, it was found that the connection between the SN and RN in *in vivo* SWI, R_2^* map, and QSM in patients with PSP can be a useful MR biomarker in the differential *in vivo* diagnosis of patients with PSP from healthy controls, patients with PD, and other patients with atypical Parkinsonian syndrome.

The original source of Chapter 4.2 is the article, Lee, H., Lee, M. J., Kim, E. J., Huh, G. Y., Lee, J. H., & Cho, H. (2021). Iron accumulation in the oculomotor nerve of the progressive supranuclear palsy brain. *Scientific reports*, 11(1), 1-9..

Chapter 5. Conclusions

5.1 Summary

In this thesis, multi-color iron magnetic resonance (MR) imaging techniques for non-invasive classification of the iron states and the separation of the various iron forms in the brain tissues were developed for the differential diagnosis of iron-related neurodegenerative diseases, such as Parkinson's disease (PD), progressive supranuclear palsy (PSP), Perry syndrome (PS), and Adult-onset leukoencephalopathy with axonal spheroids and pigmented glia (ALSP). The potential of multi-color iron MR imaging technique utilized for clinical imaging biomarkers was quantitatively investigated through the demonstration of its *in vivo* feasibility and implication on the diagnosis of patient groups from healthy subjects.

5.2 Limitations and Future works

This study has limited sample sizes of postmortem brain tissues and enrolled subjects. Especially, PD postmortem brain was not included in the study. Because formalin fixation on biological tissue can change the chemical environment through modifying the structure of the molecules, its effect should be considered for the comparison between the results of *in vivo* and *ex vivo* examinations. In *in vivo* research, the disease severities, such as Unified Parkinson's Disease Rating Scale part III (UPDRS III) or Hoehn and Yahr (H-Y) stage, were significantly different between the patients of PD and PSP, which can affect magnetic resonance imaging (MRI) contrast. Because the progression of PSP is more rapid compared to PD, matching disease duration and H-Y stage for both groups is not easily achieved in the subject enrollment.

For the future work of *in vivo* application to detect neuromelanin-iron complex in the substantia nigra, a higher-resolution image comparable to postmortem experiments will be obtained using 7T *in vivo* MRI. Further analysis will be conducted on the subjects with a larger number, including sex- and age-matched control and patient groups with various disease severities. Histopathological validation will be performed for the postmortem brains of PD, PSP, and other Parkinsonian syndromes with large amounts of samples. The advanced research will be implemented to validate the alteration of MR signal with the presence of beta-amyloid or tau according to the Alzheimer's disease progression.

References

1. Zucca, F. A., Segura-Aguilar, J., Ferrari, E., Muñoz, P., Paris, I., Sulzer, D., ... & Zecca, L. (2017). Interactions of iron, dopamine and neuromelanin pathways in brain aging and Parkinson's disease. *Progress in neurobiology*, *155*, 96-119.
2. Enochs, W. S., Petherick, P., Bogdanova, A., Mohr, U., & Weissleder, R. (1997). Paramagnetic metal scavenging by melanin: MR imaging. *Radiology*, *204*(2), 417-423.
3. Zecca, L., & Swartz, H. M. (1993). Total and paramagnetic metals in human substantia nigra and its neuromelanin. *Journal of neural transmission-Parkinson's disease and dementia section*, *5*(3), 203-213.
4. Zecca, L., Gallorini, M., Schünemann, V., Trautwein, A. X., Gerlach, M., Riederer, P., ... & Tampellini, D. (2001). Iron, neuromelanin and ferritin content in the substantia nigra of normal subjects at different ages: consequences for iron storage and neurodegenerative processes. *Journal of neurochemistry*, *76*(6), 1766-1773.
5. Ward, R. J., Zucca, F. A., Duyn, J. H., Crichton, R. R., & Zecca, L. (2014). The role of iron in brain ageing and neurodegenerative disorders. *The Lancet Neurology*, *13*(10), 1045-1060.
6. Zecca, L., Pietra, R., Goj, C., Mecacci, C., Radice, D., & Sabbioni, E. (1994). Iron and other metals in neuromelanin, substantia nigra, and putamen of human brain. *Journal of neurochemistry*, *62*(3), 1097-1101.
7. Zecca, L., Casella, L., Albertini, A., Bellei, C., Zucca, F. A., Engelen, M., ... & Sarna, T. (2008). Neuromelanin can protect against iron-mediated oxidative damage in system modeling iron overload of brain aging and Parkinson's disease. *Journal of neurochemistry*, *106*(4), 1866-1875.
8. Bolzoni, F., Giraud, S., Lopiano, L., Bergamasco, B., Fasano, M., & Crippa, P. R. (2002). Magnetic investigations of human mesencephalic neuromelanin. *Biochimica et Biophysica Acta (BBA)-Molecular Basis of Disease*, *1586*(2), 210-218.
9. Damier, P., Hirsch, E. C., Agid, Y., & Graybiel, A. M. (1999). The substantia nigra of the human brain: I. Nigrosomes and the nigral matrix, a compartmental organization based on calbindin D28K immunohistochemistry. *Brain*, *122*(8), 1421-1436.
10. Zaręba, M., Bober, A., Korytowski, W., Zecca, L., & Sarna, T. (1995). The effect of a synthetic neuromelanin on yield of free hydroxyl radicals generated in model systems. *Biochimica et Biophysica Acta (BBA)-Molecular Basis of Disease*, *1271*(2-3), 343-348.
11. Zecca, L., Mecacci, C., Seraglia, R., & Parati, E. (1992). The chemical characterization of melanin contained in substantia nigra of human brain. *Biochimica et Biophysica Acta (BBA)-Molecular Basis of Disease*, *1138*(1), 6-10.
12. Zecca, L., Shima, T., Stroppolo, A., Goj, C., Battiston, G. A., Gerbasi, R., ... & Swartz, H. M.

- (1996). Interaction of neuromelanin and iron in substantia nigra and other areas of human brain. *Neuroscience*, 73(2), 407-415.
13. Biesemeier, A., Eibl, O., Eswara, S., Audinot, J. N., Wirtz, T., Pezzoli, G., ... & Schraermeyer, U. (2016). Elemental mapping of Neuromelanin organelles of human Substantia Nigra: correlative ultrastructural and chemical analysis by analytical transmission electron microscopy and nano-secondary ion mass spectrometry. *Journal of neurochemistry*, 138(2), 339-353.
 14. Sasaki, M., Shibata, E., Kudo, K., & Tohyama, K. (2008). Neuromelanin-sensitive MRI. *Clinical Neuroradiology*, 18(3), 147-153.
 15. Nakane, T., Nihashi, T., Kawai, H., & Naganawa, S. (2008). Visualization of neuromelanin in the Substantia nigra and locus ceruleus at 1.5 T using a 3D-gradient echo sequence with magnetization transfer contrast. *Magnetic Resonance in Medical Sciences*, 7(4), 205-210.
 16. Trujillo, P., Summers, P. E., Ferrari, E., Zucca, F. A., Sturini, M., Mainardi, L. T., ... & Costa, A. (2017). Contrast mechanisms associated with neuromelanin-MRI. *Magnetic resonance in medicine*, 78(5), 1790-1800.
 17. Ogisu, K., Kudo, K., Sasaki, M., Sakushima, K., Yabe, I., Sasaki, H., ... & Shirato, H. (2013). 3D neuromelanin-sensitive magnetic resonance imaging with semi-automated volume measurement of the substantia nigra pars compacta for diagnosis of Parkinson's disease. *Neuroradiology*, 55(6), 719-724.
 18. Sasaki, M., Shibata, E., Tohyama, K., Takahashi, J., Otsuka, K., Tsuchiya, K., ... & Sakai, A. (2006). Neuromelanin magnetic resonance imaging of locus ceruleus and substantia nigra in Parkinson's disease. *Neuroreport*, 17(11), 1215-1218.
 19. Isaias, I. U., Trujillo, P., Summers, P., Marotta, G., Mainardi, L., Pezzoli, G., ... & Costa, A. (2016). Neuromelanin imaging and dopaminergic loss in Parkinson's disease. *Frontiers in aging neuroscience*, 8, 196.
 20. Schmierer, K., Scaravilli, F., Altmann, D. R., Barker, G. J., & Miller, D. H. (2004). Magnetization transfer ratio and myelin in postmortem multiple sclerosis brain. *Annals of neurology*, 56(3), 407-415.
 21. Hardy, P. A., & Henkelman, R. M. (1989). Transverse relaxation rate enhancement caused by magnetic particulates. *Magnetic resonance imaging*, 7(3), 265-275.
 22. Lee, J. H., Baek, S. Y., Song, Y., Lim, S., Lee, H., Nguyen, M. P., ... & Cho, H. (2016). The Neuromelanin-related T₂* Contrast in Postmortem Human Substantia Nigra with 7T MRI. *Scientific reports*, 6(1), 1-9.
 23. Eapen, M., Zald, D. H., Gatenby, J. C., Ding, Z., & Gore, J. C. (2011). Using high-resolution MR imaging at 7T to evaluate the anatomy of the midbrain dopaminergic system. *American Journal of Neuroradiology*, 32(4), 688-694.
 24. Zecca, L., Stroppolo, A., Gatti, A., Tampellini, D., Toscani, M., Gallorini, M., ... & Zucca, F. A.

- (2004). The role of iron and copper molecules in the neuronal vulnerability of locus coeruleus and substantia nigra during aging. *Proceedings of the National Academy of Sciences*, 101(26), 9843-9848.
25. Haacke, E. M., Xu, Y., Cheng, Y. C. N., & Reichenbach, J. R. (2004). Susceptibility weighted imaging (SWI). *Magnetic Resonance in Medicine: An Official Journal of the International Society for Magnetic Resonance in Medicine*, 52(3), 612-618.
 26. Schofield, M. A., & Zhu, Y. (2003). Fast phase unwrapping algorithm for interferometric applications. *Optics letters*, 28(14), 1194-1196.
 27. Zhou, D., Liu, T., Spincemaille, P., & Wang, Y. (2014). Background field removal by solving the Laplacian boundary value problem. *NMR in Biomedicine*, 27(3), 312-319.
 28. Liu, J., Liu, T., de Rochefort, L., Ledoux, J., Khalidov, I., Chen, W., ... & Wang, Y. (2012). Morphology enabled dipole inversion for quantitative susceptibility mapping using structural consistency between the magnitude image and the susceptibility map. *Neuroimage*, 59(3), 2560-2568.
 29. Zecca, L., Fariello, R., Riederer, P., Sulzer, D., Gatti, A., & Tampellini, D. (2002). The absolute concentration of nigral neuromelanin, assayed by a new sensitive method, increases throughout the life and is dramatically decreased in Parkinson's disease. *FEBS letters*, 510(3), 216-220.
 30. Fukunaga M, Li TQ, van Gelderen P, de Zwart JA, Shmueli K, Yao B, Lee J, Maric D, Aronova MA, Zhang G, Leapman RD, Schenck JF, Merkle H, and Duyn JH, "Layer-specific variation of iron content in cerebral cortex as a source of MRI contrast". *Proceedings of the National Academy of Sciences*, 107(8), 3834-3839. (2010).
 31. Baxan, N., Harsan, L. A., Dragonu, I., Merkle, A., Hennig, J., & von Elverfeldt, D. (2010). Myelin as a primary source of phase contrast demonstrated in vivo in the mouse brain. In *Proc., ISMRM, 19th Annual Meeting and Exhibition, Stockholm, Sweden* (p. 3016).
 32. Liu, C., Li, W., Johnson, G. A., & Wu, B. (2011). High-field (9.4 T) MRI of brain dysmyelination by quantitative mapping of magnetic susceptibility. *Neuroimage*, 56(3), 930-938.
 33. Wang, Z. J., Lian, L., Chen, Q., Zhao, H., Asakura, T., & Cohen, A. R. (2005). 1/T₂ and magnetic susceptibility measurements in a gerbil cardiac iron overload model. *Radiology*, 234(3), 749-755.
 34. Drayer, B., Burger, P., Darwin, R., Riederer, S., Herfkens, R., & Johnson, G. A. (1986). Magnetic resonance imaging of brain iron. *American journal of neuroradiology*, 7(3), 373-380.
 35. Shima, T., Sarna, T., Swartz, H. M., Stroppolo, A., Gerbasi, R., & Zecca, L. (1997). Binding of iron to neuromelanin of human substantia nigra and synthetic melanin: an electron paramagnetic resonance spectroscopy study. *Free Radical Biology and Medicine*, 23(1), 110-119.
 36. Jellinger, K., Kienzl, E., Rumpelmair, G., Riederer, P., Stachelberger, H., Ben-Shachar, D., & Youdim, M. B. H. (1992). Iron-melanin complex in substantia nigra of parkinsonian brains: an

- x-ray microanalysis. *Journal of neurochemistry*, 59(3), 1168-1171.
37. Faucheux, B. A., Martin, M. E., Beaumont, C., Hauw, J. J., Agid, Y., & Hirsch, E. C. (2003). Neuromelanin associated redox-active iron is increased in the substantia nigra of patients with Parkinson's disease. *Journal of neurochemistry*, 86(5), 1142-1148.
 38. Nagara, H., Inoue, T., Koga, T., Kitaguchi, T., Tateishi, J., & Goto, I. (1987). Formalin fixed brains are useful for magnetic resonance imaging (MRI) study. *Journal of the neurological sciences*, 81(1), 67-77.
 39. Schmierer, K., Wheeler-Kingshott, C. A., Tozer, D. J., Boulby, P. A., Parkes, H. G., Yousry, T. A., ... & Miller, D. H. (2008). Quantitative magnetic resonance of postmortem multiple sclerosis brain before and after fixation. *Magnetic Resonance in Medicine: An Official Journal of the International Society for Magnetic Resonance in Medicine*, 59(2), 268-277.
 40. Schmierer, K., Thavarajah, J. R., An, S. F., Brandner, S., Miller, D. H., & Tozer, D. J. (2010). Effects of formalin fixation on magnetic resonance indices in multiple sclerosis cortical gray matter. *Journal of magnetic resonance imaging*, 32(5), 1054-1060.
 41. Dietrich, O., Levin, J., Ahmadi, S. A., Plate, A., Reiser, M. F., Bötzel, K., ... & Ertl-Wagner, B. (2017). MR imaging differentiation of Fe 2+ and Fe 3+ based on relaxation and magnetic susceptibility properties. *Neuroradiology*, 59(4), 403-409.
 42. Hoehn, M. M., & Yahr, M. D. (1998). Parkinsonism: onset, progression, and mortality. *Neurology*, 50(2), 318-318.
 43. Dauer, W., & Przedborski, S. (2003). Parkinson's disease: mechanisms and models. *Neuron*, 39(6), 889-909.
 44. Enochs, W. S., Nilges, M. J., & Swartz, H. M. (1993). Purified human neuromelanin, synthetic dopamine melanin as a potential model pigment, and the normal human substantia nigra: characterization by electron paramagnetic resonance spectroscopy. *Journal of neurochemistry*, 61(1), 68-79.
 45. Enochs, W. S., Hyslop, W. B., Bennett, H. F., Brown 3rd, R. D., Koenig, S. H., & Swartz, H. M. (1989). Sources of the increased longitudinal relaxation rates observed in melanotic melanoma. An in vitro study of synthetic melanins. *Investigative radiology*, 24(10), 794-804.
 46. Lehericy, S., Sharman, M. A., Santos, C. L. D., Paquin, R., & Gallea, C. (2012). Magnetic resonance imaging of the substantia nigra in Parkinson's disease. *Movement disorders*, 27(7), 822-830.
 47. Chen, X., Huddleston, D. E., Langley, J., Ahn, S., Barnum, C. J., Factor, S. A., ... & Hu, X. (2014). Simultaneous imaging of locus coeruleus and substantia nigra with a quantitative neuromelanin MRI approach. *Magnetic resonance imaging*, 32(10), 1301-1306.
 48. Cassidy, C. M., Zucca, F. A., Girgis, R. R., Baker, S. C., Weinstein, J. J., Sharp, M. E., ... & Horga, G. (2019). Neuromelanin-sensitive MRI as a noninvasive proxy measure of dopamine

- function in the human brain. *Proceedings of the National Academy of Sciences*, 116(11), 5108-5117.
49. Lehericy, S., Bardinet, E., Poupon, C., Vidailhet, M., & François, C. (2014). 7 Tesla magnetic resonance imaging: a closer look at substantia nigra anatomy in Parkinson's disease. *Movement Disorders*, 29(13), 1574-1581.
 50. Schwarz, S. T., Afzal, M., Morgan, P. S., Bajaj, N., Gowland, P. A., & Auer, D. P. (2014). The 'swallow tail' appearance of the healthy nigrosome—a new accurate test of Parkinson's disease: a case-control and retrospective cross-sectional MRI study at 3T. *PloS one*, 9(4), e93814.
 51. Blazejewska, A. I., Schwarz, S. T., Pitiot, A., Stephenson, M. C., Lowe, J., Bajaj, N., ... & Gowland, P. A. (2013). Visualization of nigrosome 1 and its loss in PD: pathoanatomical correlation and in vivo 7 T MRI. *Neurology*, 81(6), 534-540.
 52. Baudrexel, S., Nürnberger, L., Rüb, U., Seifried, C., Klein, J. C., Deller, T., ... & Hilker, R. (2010). Quantitative mapping of T1 and T2* discloses nigral and brainstem pathology in early Parkinson's disease. *Neuroimage*, 51(2), 512-520.
 53. Barbosa, J. H. O., Santos, A. C., Tumas, V., Liu, M., Zheng, W., Haacke, E. M., & Salmon, C. E. G. (2015). Quantifying brain iron deposition in patients with Parkinson's disease using quantitative susceptibility mapping, R2 and R2. *Magnetic resonance imaging*, 33(5), 559-565.
 54. An, H., Zeng, X., Niu, T., Li, G., Yang, J., Zheng, L., ... & Li, J. (2018). Quantifying iron deposition within the substantia nigra of Parkinson's disease by quantitative susceptibility mapping. *Journal of the neurological sciences*, 386, 46-52.
 55. Zhang, Y., Larcher, K. M. H., Misic, B., & Dagher, A. (2017). Anatomical and functional organization of the human substantia nigra and its connections. *Elife*, 6, e26653.
 56. Rudow, G., O'Brien, R., Savonenko, A. V., Resnick, S. M., Zonderman, A. B., Pletnikova, O., ... & Troncoso, J. C. (2008). Morphometry of the human substantia nigra in ageing and Parkinson's disease. *Acta neuropathologica*, 115(4), 461.
 57. Lee, H., Baek, S. Y., Chun, S. Y., Lee, J. H., & Cho, H. (2018). Specific visualization of neuromelanin-iron complex and ferric iron in the human post-mortem substantia nigra using MR relaxometry at 7T. *Neuroimage*, 172, 874-885.
 58. Chung, E. J., Hwang, J. H., Lee, M. J., Hong, J. H., Ji, K. H., Yoo, W. K., ... & Kim, Y. J. (2014). Expansion of the clinicopathological and mutational spectrum of Perry syndrome. *Parkinsonism & related disorders*, 20(4), 388-393.
 59. Birkl, C., Langkammer, C., Golob-Schwarzl, N., Leoni, M., Haybaeck, J., Goessler, W., ... & Ropele, S. (2016). Effects of formalin fixation and temperature on MR relaxation times in the human brain. *NMR in Biomedicine*, 29(4), 458-465.
 60. Möller, H. E., Bossoni, L., Connor, J. R., Crichton, R. R., Does, M. D., Ward, R. J., ... & Ronen, I. (2019). Iron, myelin, and the brain: neuroimaging meets neurobiology. *Trends in*

- neurosciences*, 42(6), 384-401.
61. Melki, P. S., & Mulkern, R. V. (1992). Magnetization transfer effects in multislice RARE sequences. *Magnetic resonance in medicine*, 24(1), 189-195.
 62. Santyr, G. E. (1993). Magnetization transfer effects in multislice MR imaging. *Magnetic resonance imaging*, 11(4), 521-532.
 63. Liu, T., Spincemaille, P., De Rochefort, L., Kressler, B., & Wang, Y. (2009). Calculation of susceptibility through multiple orientation sampling (COSMOS): a method for conditioning the inverse problem from measured magnetic field map to susceptibility source image in MRI. *Magnetic Resonance in Medicine: An Official Journal of the International Society for Magnetic Resonance in Medicine*, 61(1), 196-204.
 64. Troprès, I., Pannetier, N., Grand, S., Lemasson, B., Moisan, A., Péoc'h, M., ... & Barbier, E. L. (2015). Imaging the microvessel caliber and density: principles and applications of microvascular MRI. *Magnetic resonance in medicine*, 73(1), 325-341.
 65. Cosottini, M., Frosini, D., Pesaresi, I., Costagli, M., Biagi, L., Ceravolo, R., ... & Tosetti, M. (2014). MR imaging of the substantia nigra at 7 T enables diagnosis of Parkinson disease. *Radiology*, 271(3), 831-838.
 66. Denk, C., & Rauscher, A. (2010). Susceptibility weighted imaging with multiple echoes. *Journal of Magnetic Resonance Imaging*, 31(1), 185-191.
 67. Bergsland, N., Zivadinov, R., Schweser, F., Hagemeyer, J., Lichter, D., & Guttuso Jr, T. (2019). Ventral posterior substantia nigra iron increases over 3 years in Parkinson's disease. *Movement Disorders*, 34(7), 1006-1013.
 68. Sulzer, D., Cassidy, C., Horga, G., Kang, U. J., Fahn, S., Casella, L., ... & Zecca, L. (2018). Neuromelanin detection by magnetic resonance imaging (MRI) and its promise as a biomarker for Parkinson's disease. *NPJ Parkinson's disease*, 4(1), 1-13.
 69. Mai, J. K., & Paxinos, G. (Eds.). (2011). *The human nervous system*. Academic press.
 70. Kau, T., Hametner, S., Endmayr, V., Deistung, A., Prihoda, M., Haimburger, E., ... & Grabner, G. (2019). Microvessels may Confound the "Swallow Tail Sign" in Normal Aged Midbrains: A Postmortem 7 T SW-MRI Study. *Journal of Neuroimaging*, 29(1), 65-69.
 71. McGeer, P. L., Itagaki, S., Boyes, B. E., & McGeer, E. G. (1988). Reactive microglia are positive for HLA-DR in the substantia nigra of Parkinson's and Alzheimer's disease brains. *Neurology*, 38(8), 1285-1285.
 72. Kim, M., Lee, H., Cho, H. J., Young Chun, S., Shin, J. H., Kim, E. J., ... & Lee, J. H. (2017). Pathologic correlation of paramagnetic white matter lesions in adult-onset leukoencephalopathy with axonal spheroids and pigmented glia. *Journal of Neuropathology & Experimental Neurology*, 76(11), 924-928.
 73. Peckham, M. E., Dashtipour, K., Holshouser, B. A., Kani, C., Boscanin, A., Kani, K., & Harder,

- S. L. (2016). Novel pattern of iron deposition in the fascicula nigrale in patients with Parkinson's disease: a pilot study. *Radiology research and practice*, 2016.
74. Mukai, M., Sugaya, K., Yabe, I., Goto, Y. I., Yokochi, F., Miyamoto, K., ... & Matsubara, S. (2013). Neuromelanin MRI in a family with mitochondrial parkinsonism harboring a Y955C mutation in POLG1. *Parkinsonism & related disorders*, 19(9), 821-824.
 75. Langley, J., Huddleston, D. E., Chen, X., Sedlacik, J., Zachariah, N., & Hu, X. (2015). A multicontrast approach for comprehensive imaging of substantia nigra. *Neuroimage*, 112, 7-13.
 76. Schwarz, S. T., Xing, Y., Tomar, P., Bajaj, N., & Auer, D. P. (2017). In vivo assessment of brainstem depigmentation in Parkinson disease: potential as a severity marker for multicenter studies. *Radiology*, 283(3), 789-798.
 77. Takahashi, H., Watanabe, Y., Tanaka, H., Mihara, M., Mochizuki, H., Liu, T., ... & Tomiyama, N. (2018). Quantifying changes in nigrosomes using quantitative susceptibility mapping and neuromelanin imaging for the diagnosis of early-stage Parkinson's disease. *The British journal of radiology*, 91(1086), 20180037.
 78. Hashido, T., & Saito, S. (2016). Quantitative T1, T2, and T2* mapping and semi-quantitative neuromelanin-sensitive magnetic resonance imaging of the human midbrain. *PloS one*, 11(10), e0165160.
 79. Wallis, L. I., Paley, M. N., Graham, J. M., Grünewald, R. A., Wignall, E. L., Joy, H. M., & Griffiths, P. D. (2008). MRI assessment of basal ganglia iron deposition in Parkinson's disease. *Journal of Magnetic Resonance Imaging: An Official Journal of the International Society for Magnetic Resonance in Medicine*, 28(5), 1061-1067.
 80. Nicholson, A. M., Baker, M. C., Finch, N. A., Rutherford, N. J., Wider, C., Graff-Radford, N. R., ... & Rademakers, R. (2013). CSF1R mutations link POLD and HDLS as a single disease entity. *Neurology*, 80(11), 1033-1040.
 81. Konno, T., Yoshida, K., Mizuno, T., Kawarai, T., Tada, M., Nozaki, H., ... & Ikeuchi, T. (2017). Clinical and genetic characterization of adult-onset leukoencephalopathy with axonal spheroids and pigmented glia associated with CSF 1R mutation. *European journal of neurology*, 24(1), 37-45.
 82. Liu, C., Li, W., Tong, K. A., Yeom, K. W., & Kuzminski, S. (2015). Susceptibility-weighted imaging and quantitative susceptibility mapping in the brain. *Journal of magnetic resonance imaging*, 42(1), 23-41.
 83. Langkammer, C., Krebs, N., Goessler, W., Scheurer, E., Yen, K., Fazekas, F., & Ropele, S. (2012). Susceptibility induced gray-white matter MRI contrast in the human brain. *Neuroimage*, 59(2), 1413-1419.
 84. Bagnato, F., Hametner, S., Yao, B., van Gelderen, P., Merkle, H., Cantor, F. K., ... & Duyn, J. H. (2011). Tracking iron in multiple sclerosis: a combined imaging and histopathological study at

- 7 Tesla. *Brain*, 134(12), 3602-3615.
85. Ali, Z. S., Van Der Voorn, J. P., & Powers, J. M. (2007). A comparative morphologic analysis of adult onset leukodystrophy with neuroaxonal spheroids and pigmented glia—a role for oxidative damage. *Journal of Neuropathology & Experimental Neurology*, 66(7), 660-672.
 86. Liu, T., Wisnieff, C., Lou, M., Chen, W., Spincemaille, P., & Wang, Y. (2013). Nonlinear formulation of the magnetic field to source relationship for robust quantitative susceptibility mapping. *Magnetic resonance in medicine*, 69(2), 467-476.
 87. Kim, E. J., Shin, J. H., Lee, J. H., Kim, J. H., Na, D. L., Suh, Y. L., ... & Huh, G. Y. (2015). Adult-onset leukoencephalopathy with axonal spheroids and pigmented glia linked CSF1R mutation: report of four Korean cases. *Journal of the neurological sciences*, 349(1-2), 232-238.
 88. Drayer, B. P. R. S. R. G., Burger, P., Darwin, R., Riederer, S., Herfkens, R., & Johnson, G. A. (1986). MRI of brain iron. *American Journal of Roentgenology*, 147(1), 103-110.
 89. Hodel, J., Outteryck, O., Verclytte, S., Deramecourt, V., Lacour, A., Pruvo, J. P., ... & Leclerc, X. (2015). Brain magnetic susceptibility changes in patients with natalizumab-associated progressive multifocal leukoencephalopathy. *American Journal of Neuroradiology*, 36(12), 2296-2302.
 90. Walker, D. G., & Lue, L. F. (2015). Immune phenotypes of microglia in human neurodegenerative disease: challenges to detecting microglial polarization in human brains. *Alzheimer's research & therapy*, 7(1), 1-9.
 91. van Duijn, S., Nabuurs, R. J., van Duinen, S. G., & Natté, R. (2013). Comparison of histological techniques to visualize iron in paraffin-embedded brain tissue of patients with Alzheimer's disease. *Journal of Histochemistry & Cytochemistry*, 61(11), 785-792.
 92. Freeman, S. H., Hyman, B. T., Sims, K. B., Hedley-Whyte, E. T., Vossough, A., Frosch, M. P., & Schmahmann, J. D. (2009). Adult onset leukodystrophy with neuroaxonal spheroids: clinical, neuroimaging and neuropathologic observations. *Brain Pathology*, 19(1), 39-47.
 93. Lee, J., Shmueli, K., Fukunaga, M., van Gelderen, P., Merkle, H., Silva, A. C., & Duyn, J. H. (2010). Sensitivity of MRI resonance frequency to the orientation of brain tissue microstructure. *Proceedings of the National Academy of Sciences*, 107(11), 5130-5135.
 94. Meguro, R., Asano, Y., Odagiri, S., Li, C., Iwatsuki, H., & Shoumura, K. (2007). Nonheme-iron histochemistry for light and electron microscopy: a historical, theoretical and technical review. *Archives of histology and cytology*, 70(1), 1-19.
 95. Dexter, D. T., Carayon, A., Javoy-Agid, F., Agid, Y., Wells, F. R., Daniel, S. E., ... & Marsden, C. D. (1991). Alterations in the levels of iron, ferritin and other trace metals in Parkinson's disease and other neurodegenerative diseases affecting the basal ganglia. *Brain*, 114(4), 1953-1975.
 96. Sian-Hülsmann, J., Mandel, S., Youdim, M. B., & Riederer, P. (2011). The relevance of iron in

- the pathogenesis of Parkinson's disease. *Journal of neurochemistry*, 118(6), 939-957.
97. Belaidi, A. A., & Bush, A. I. (2016). Iron neurochemistry in Alzheimer's disease and Parkinson's disease: targets for therapeutics. *Journal of neurochemistry*, 139, 179-197.
 98. Kruszewski, M. (2003). Labile iron pool: the main determinant of cellular response to oxidative stress. *Mutation Research/Fundamental and Molecular Mechanisms of Mutagenesis*, 531(1-2), 81-92.
 99. Lee, D. W., & Andersen, J. K. (2010). Iron elevations in the aging Parkinsonian brain: a consequence of impaired iron homeostasis?. *Journal of neurochemistry*, 112(2), 332-339.
 100. Sukhorukova, E. G., Alekseeva, O. S., & Korzhevsky, D. E. (2014). Catecholaminergic neurons of mammalian brain and neuromelanin. *Journal of Evolutionary Biochemistry and Physiology*, 50(5), 383-391.
 101. Lee, J. H., & Lee, M. S. (2019). Brain iron accumulation in atypical parkinsonian syndromes: in vivo MRI evidences for distinctive patterns. *Frontiers in neurology*, 10, 74.
 102. Brooks, D. J. (2002). Diagnosis and management of atypical parkinsonian syndromes. *Journal of Neurology, Neurosurgery & Psychiatry*, 72(suppl 1), i10-i16.
 103. Dickson, D. W. (2012). Parkinson's disease and parkinsonism: neuropathology. *Cold Spring Harbor perspectives in medicine*, 2(8), a009258.
 104. Grandas, F., & Esteban, A. (1994). Eyelid motor abnormalities in progressive supranuclear palsy. *Progressive Supranuclear Palsy: Diagnosis, Pathology, and Therapy*, 33-41.
 105. Lamberti, P., De Mari, M., Zenzola, A., Aniello, M. S., & Defazio, G. (2002). Frequency of apraxia of eyelid opening in the general population and in patients with extrapyramidal disorders. *Neurological Sciences*, 23(2), s81-s82.
 106. Gupta, D., Saini, J., Kesavadas, C., Sarma, P. S., & Kishore, A. (2010). Utility of susceptibility-weighted MRI in differentiating Parkinson's disease and atypical parkinsonism. *Neuroradiology*, 52(12), 1087-1094.
 107. Sjöström, H., Granberg, T., Westman, E., & Svenningsson, P. (2017). Quantitative susceptibility mapping differentiates between parkinsonian disorders. *Parkinsonism & related disorders*, 44, 51-57.
 108. Foroutan, P., Murray, M. E., Fujioka, S., Schweitzer, K. J., Dickson, D. W., Wszolek, Z. K., & Grant, S. C. (2013). Progressive supranuclear palsy: high-field-strength MR microscopy in the human substantia nigra and globus pallidus. *Radiology*, 266(1), 280-288.
 109. Massey, L. A., Miranda, M. A., Al-Helli, O., Parkes, H. G., Thornton, J. S., So, P. W., ... & Yousry, T. A. (2017). 9.4 T MR microscopy of the substantia nigra with pathological validation in controls and disease. *NeuroImage: Clinical*, 13, 154-163.
 110. Raman, M. R., Shu, Y., Lesnick, T. G., Jack, C. R., & Kantarci, K. (2017). Regional T1 relaxation time constants in ex vivo human brain: longitudinal effects of formalin exposure. *Magnetic*

resonance in medicine, 77(2), 774-778.

111. Dawe, R. J., Bennett, D. A., Schneider, J. A., Vasireddi, S. K., & Arfanakis, K. (2009). Postmortem MRI of human brain hemispheres: T2 relaxation times during formaldehyde fixation. *Magnetic Resonance in Medicine: An Official Journal of the International Society for Magnetic Resonance in Medicine*, 61(4), 810-818.
112. Langkammer, C., Schweser, F., Krebs, N., Deistung, A., Goessler, W., Scheurer, E., ... & Reichenbach, J. R. (2012). Quantitative susceptibility mapping (QSM) as a means to measure brain iron? A post mortem validation study. *Neuroimage*, 62(3), 1593-1599.
113. Austin, C., Fryer, F., Lear, J., Bishop, D., Hare, D., Rawling, T., ... & Doble, P. (2011). Factors affecting internal standard selection for quantitative elemental bio-imaging of soft tissues by LA-ICP-MS. *Journal of Analytical Atomic Spectrometry*, 26(7), 1494-1501.
114. Hughes, A. J., Daniel, S. E., Kilford, L., & Lees, A. J. (1992). Accuracy of clinical diagnosis of idiopathic Parkinson's disease: a clinico-pathological study of 100 cases. *Journal of neurology, neurosurgery & psychiatry*, 55(3), 181-184.
115. Höglinger, G. U., Respondek, G., Stamelou, M., Kurz, C., Josephs, K. A., Lang, A. E., ... & Bordelon, Y. (2017). Clinical diagnosis of progressive supranuclear palsy: the movement disorder society criteria. *Movement Disorders*, 32(6), 853-864.
116. Lee, H., Baek, S. Y., Kim, E. J., Huh, G. Y., Lee, J. H., & Cho, H. (2020). MRI T2 and T2* relaxometry to visualize neuromelanin in the dorsal substantia nigra pars compacta. *NeuroImage*, 211, 116625.
117. Rao, S. S., & Adlard, P. A. (2018). Untangling tau and iron: exploring the interaction between iron and tau in neurodegeneration. *Frontiers in molecular neuroscience*, 11, 276.
118. Shoeibi, A., Olfati, N., & Litvan, I. (2019). Frontrunner in translation: progressive supranuclear palsy. *Frontiers in neurology*, 10, 1125.
119. Bartzokis, G., Lu, P. H., & Mintz, J. (2007). Human brain myelination and amyloid beta deposition in Alzheimer's disease. *Alzheimer's & dementia*, 3(2), 122-125.
120. Heidari, M., Johnstone, D. M., Bassett, B., Graham, R. M., Chua, A. C. G., House, M. J., ... & Milward, E. A. (2016). Brain iron accumulation affects myelin-related molecular systems implicated in a rare neurogenetic disease family with neuropsychiatric features. *Molecular psychiatry*, 21(11), 1599-1607.
121. Duyn, J. H., & Schenck, J. (2017). Contributions to magnetic susceptibility of brain tissue. *NMR in Biomedicine*, 30(4), e3546.
122. Wisnieff, C., Ramanan, S., Olesik, J., Gauthier, S., Wang, Y., & Pitt, D. (2015). Quantitative susceptibility mapping (QSM) of white matter multiple sclerosis lesions: interpreting positive susceptibility and the presence of iron. *Magnetic resonance in medicine*, 74(2), 564-570.
123. Lewis, M. M., Du, G., Baccon, J., Snyder, A. M., Murie, B., Cooper, F., ... & Huang, X. (2018).

Susceptibility MRI captures nigral pathology in patients with parkinsonian syndromes. *Movement Disorders*, 33(9), 1432-1439.

Acknowledgements

This thesis is the comprehensive results of my research over the past six years at Ulsan national institute of Science and Technology.

I would like to start with big thanks to all the people who helped my work throughout my MS-PhD combined course.

I would like to express my sincere gratitude to my supervisor, professor HyungJoon Cho for committed guidance and careful encouragement. He has given me endless opportunities with trust so that I could be interested in my research. He has influenced my thought on the research and my attitude toward life like a parent.

I would like to sincerely thank professor Jae-Hyeok Lee for the great advice on clinical research as a co-supervisor. The collaborative study with him has enabled me to experience the unique and broad research area.

I really respect the aspiration of both professors for research. Without their efforts and contributions, this thesis couldn't have seen the light of the day.

I highly appreciate the help of BISE laboratory members. They have been nice, friendly, and positive every moment. The inspiring discussions with them have provided new insights and fresh ideas on my research. I have shared so many impressive moments with them.

I am infinitely thankful to my family for their unlimited financial and emotional support in my life. I would like to thank my parents for giving me birth, raising and taking care of me. I would like to say I have always been proud of you and your life to my younger brother. I love you guys so much. I'll always try my best to be a devoted son and proud brother.

Finally, I love my best friends who will walk with me for the rest of my life. Let's all succeed together!